REFERENCE : SD-TN-AI-1289
DATE : July 2010
ISSUE : draft **Page :** 1/69

ASSESSMENT OF A NEXT GENERATION GRAVITY MISSION FOR MONITORING THE VARIATIONS OF EARTH'S GRAVITY FIELD

TN3: INSTRUMENT CONCEPTS

Written by	***Responsibility*** + handwritten signature if no electronic workflow tool
S. Cesare	Author
S. Mottini	Author
B. Christophe (ONERA)	Author
Verified by	
A. Anselmi	Checker
Approved by	
A. Anselmi	Study Manager
Documentation Manager	
R. Cavaglià	

Approval evidence is kept within the documentation management system.

CHANGE RECORDS

ISSUE	DATE	§ CHANGE RECORDS	AUTHOR
draft	July 10		sc, sm, bc

TABLE OF CONTENTS

1. INTRODUCTION

1.1 Scope and Purpose

This document is submitted in fulfilment of WP 2120 of the Next Generation Gravity Mission (NGGM) study. Its purpose is:

- to establish the top-level requirements, measurement models and error trees for the reference observing techniques of the NGGM established in WP 2110 [RD-12]
- to review the state-of-art of the measurement technologies involved in the reference observing techniques of the NGGM and recommended the most appropriate technologies;
- to define instrument concepts potentially capable to meet the performance requirements;
- to compare the various instrument concepts and make recommendations on the reference instrument concept for the NGGM;
- to establish a first measurement error allocation and specifications for reference instrument concept and for the satellite functions involved in the observing technique;
- to outline the calibration approach of the recommended reference instrument concept.

2. DOCUMENTS

2.1 Applicable Documents

[AD-1] Assessment of a Next Generation Gravity Mission to monitor the variations of Earth's gravity field, Statement of Work, EOP-SF/2008-09-1334, Issue 2, 20 November 2008, Appendix 1 to AO/1-5914/09/NL/CT

[AD-2] Special Conditions of Tender, Appendix 3 to AO/1-5914/09/NL/CT

[AD-3] Draft Contract. Appendix 2 to AO/1-5914/09/NL/CT.

2.2 ESA Reference Documents

[RD-1] Rummel et al. (2003), Scientific objectives for Future Geopotential Missions, Technical Note, Version 6 from the ESA contract No: 16668/02/NL/MM "Enabling Observation Techniques for Future Solid Earth Missions"

[RD-2] Koop, R., Rummel, R. (2007), The Future of Satellite Gravimetry, Final Report of the Future Gravity Mission Workshop, 12-13 April 2007 ESA/ESTEC, Noordwiik, Netherlands

[RD-3] Laser Doppler Interferometry Mission for determination of the Earth's Gravity Field, ESTEC Contract 18456/04/NL/CP, Final Report, Issue 1, 19 December 2005

[RD-4] Laser Interferometry High Precision Tracking for LEO, ESA Contract No. 0512/06/NL/IA, Final Report, July 2008

[RD-5] System Support to Laser Interferometry Tracking Technology Development for Gravity Field Monitoring, ESA Contract No. 20846/07/NL/FF, Final report, September 2008

[RD-6] Bender P.L., Wiese D.N., and Nerem R.S., "A Possible Dual-GRACE Mission With 90 Degree And 63 Degree Inclination Orbits", Proceedings of the 3rd International Symposium on Formation Flying, Missions and Technologies, Noordwijk (NL), April 2008

[RD-7] T. van Dam et al., Monitoring and Modelling Individual Sources of Mass Distribution and Transport in the Earth System by Means of Satellites, Final Report, ESA Contract No. 20403, November 2008

[RD-8] Variable Earth Model Description and Product Specification Document, ESA Contract No. 20403, November 2008

[RD-9] Enabling Observation Techniques for Future Solid Earth Missions, ESA Contract No: 16668/02/ NL/MM, Final report, Issue 2, 15 July 2004.A

2.3 Further Reference Documents

[RD-10] Study Technical Note "Requirement Analysis", NGGM_SCI_1, Issue 1, Revision 1, 08-February, 2010

[RD-11] Study Technical Note "System Drivers", SD-TN-AI-1262, 4-DEC-09

[RD-12] Study Technical Note "Observing Techniques", NGGM_SCI_2, in preparation

[RD-13] Study Technical Note “Mission Analysis and AOCS concepts”, SD-TN-AI-1290.

[RD-14] Michael Watkins, NASA Time Variable Gravity Mapping Mission (Grace Follow-On/Grace II/EX-5) Study, Future Gravity Mission Workshop, 12-13 April 2007 ESA/ESTEC, Noordwiik, Netherlands.

[RD-15] M. Watkins, B. Tapley, W. Folkner, B. Chao, EX-5: Time Dependent Gravity Field Mapping, presented at Gravity, Geoid and Geodynamics workshop, Banff, Canada, 31-Jul-2000

[RD-16] R.S. Nerem, P. Bender, and B. Loomis, M. Stephens, R. Craig, J. Leitch, and R. Pierce, Interferometric Range Transceiver for Measuring Temporal Gravity Variations

[RD-17] W.M. Klipstein, M. Mohageg, J.A. White, and B.C. Young, Optical Frequency Standard Development in Support of Nasa’s Gravity Mapping Missons

[RD-18] Darwin–Payload Definition Document, SCI-A/2005/301/DARWIN/DMS/LdA, Issue 1, 31/08/2005

[RD-19] High Precision Optical Metrology, Final Presentation handouts, ESTEC, 22/05/2006

[RD-20] LISA Laser Interferometer Space Antenna: a Cornerstone Mission for the Observation of Gravitational Waves; Study report; ESA-SCI(2000)11, July 2000

[RD-21] LISA study of the Laser Interferometer Space Antenna; Final Technical report; ASTRIUM Report No. LI-RP-DS-009, April 2000, ESTEC Contract 13631/99/NL/MS

[RD-22] G. Heinzel, “LISA technology for gravity-field missions”, Graz Workshop, 30/9/2009

[RD-23] NGGM TN3 Part 3 “Instrument Concepts”, ONERA, 1/16598 DMPH, draft, July 201

[RD-24] Laser Interferometry High Precision Tracking for LEO, ESA Contract No. 0512/06/NL/IA, CCN01 Report, July 2009.

[RD-25] Davar Feili et al., Radio Frequency Mini Ion Engines for Fine Attitude Control and Formation Flying Applications, presented at the Second CEAS European Air & Space Conference, Manchester, UK20-26 October 2009.

[RD-26] S. Cesare, G. Catastini, R. Floberghagen, D. Lamarre, The in-flight calibration of the GOCE accelerometer, presented at ESA Living Planet Symposium, 28 June - 2 July 2010, Bergen, Norway.

3. TOP-LEVEL MEASUREMENT REQUIREMENTS AND ERROR BUDGETS FOR NGGM

3.1 Introduction: from scientific objectives to the measurement requirements

The primary scientific objectives of the NGGM have been identified in [RD-10] as the improvement of our understanding of ice sheet and glaciers melting trends, continental water cycles, ocean masses dynamics and solid-earth deformations through the mass transports (and then the temporal variations of the gravity field) that they produce within the Earth system.

In order to properly investigate these geophysical phenomena the NGGM shall cover all the latitudes for a 11 year lifetime (complete solar cycle), completing a full repeat cycle of the ground tracks in ~1 month (temporal resolution at the maximum spatial resolution) with a sub-cycle of a few days [RD-12]. The monthly gravity field solutions shall enable to resolve the geoid height with a cumulative error better or equal to [RD-12]:

- 0.1 mm at spherical harmonic degree 150 (spatial resolution = 133 km),
- 1 mm at spherical harmonic degree 200 (spatial resolution = 100 km),
- 10 mm at spherical harmonic degree 250 (spatial resolution = 80 km).

The low-low Satellite-to-Satellite Tracking (ll-SST) is in practice the only observing technique potentially capable to detect the time variable gravity signal with the required resolution from the lowest to the highest degrees, while the gradiometry could contribute to highest degrees and orders only and no significant contribution is added by the precise orbit determination which can be obtained from a GNSS receiver [RD-12]. As described in [RD-11], in the GRACE-like implementation of the ll-SST (Figure 3.1-1), the fundamental observable is the distance *variation* between two satellites centers of mass (COMs) produced by the gravity acceleration, Δd_G, formally obtained from Δd - Δd_D, where Δd is the total distance variation between the COMs, whatever the source, as measured by a distance metrology, and Δd_D is the distance variation produced by non-gravitational (i.e. drag) forces, as measured by accelerometers.

An alternative implementation of the ll-SST consists in referring the distance measurement not to the COMs of the satellites, but to two test masses places into “cavities” inside the satellites and kept in drag-free condition by the screening actions of the surface forces (aerodynamic drag, radiation pressure) exercised by the satellites themselves (Figure 3.1-2). So doing, the test masses motion would be driven in principle by gravity force only and the measurement of their relative distance variation would provide directly the fundamental observable d_G, without the need of subtracting the effect of the non-gravitational accelerations measured separately. However, there some technical implementation problems and programmatic aspects that advice to discard this solution for the NGGM:

- An “inertial sensor” (i.e. the cavity with the free floating test mass) is significantly more complex than an accelerometer due to the presence of the mandatory locking device of the test mass, of the interface between the test mass and the distance metrology (that implies for instance the presence of an optical window in the sensor housing) and very likely of a non-conductive discharge device.
- Unless a retro-reflector is embedded in the test mass (but the lack of this element in the inertial sensors designed so far for the LISA Pathfinder and LISA missions suggests

practical limitations in this solution) and the retro-reflection point is located precisely at the COM of the test mass, a very precise alignment and stability of the test mass reflecting surface with the measurement axis of the distance metrology is mandatory to avoid couplings between the test mass rotations and the distance measurement. This very precise alignment/stability can be avoided in a GRACE-like implementation of the ll-SST by using retro-reflectors for the distance metrology and knowing very precisely the alignment of the two satellites relative to the measurement axis.

- Unlike an accelerometer, the operation of an inertial sensor (starting from the initial acquisition of the free floating condition) needs a much quieter perturbation environment both external (e.g. drag forces, Earth gravity gradient) and internal (e.g. self-gravity). In fact, the only two missions making use of inertial sensors (LISA Pathfinder and LISA) operates far from the Earth.
- The use of the test mass of an inertial sensor as reference point for the distance measurement makes more complex the implementation of a redundant instrument.
- The development and implementation of high-precision accelerometers for space applications has been widely validated by the successful flight experience of CHAMP, GRACE and GOCE, while no inertial sensor has been launched yet. Moreover, the use of an inertial sensor in a very low-Earth orbit will likely need some extra development with respect to the models developed for LISA Pathfinder and LISA.

In conclusion, the GRACE-like implementation of the ll-SST in which the role of test masses immersed in the Earth gravity field is played by the satellites themselves and their non-gravitational acceleration is measured by accelerometers (to remove its effect on the overall satellite-to-satellite distance variation), is considered the baseline for the NGGM.
From a set of semi-analytical simulations spanning a wide range of mission performance factors [RD-12] it turns out that the required geoid height cumulative error at the spherical harmonic degree 150, 200, 250 can be achieved for instance with the following parameter combination:

- orbit altitude = 300 km,
- satellite-to-satellite distance = 100 km,
- satellite-to-satellite distance variation relative error spectral density $\leq 2 \cdot 10^{-13}$ $1/\sqrt{Hz}$,
- non-gravitational acceleration measurement error spectral density $\leq 10^{-11}$ $m/s^2/\sqrt{Hz}$.

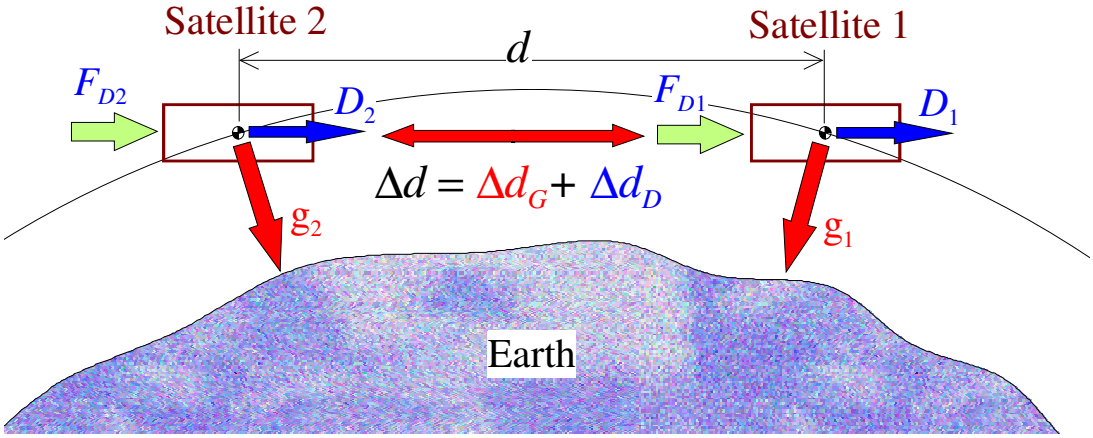

Figure 3.1-1 : Low-low satellite-to-satellite tracking concept (GRACE)

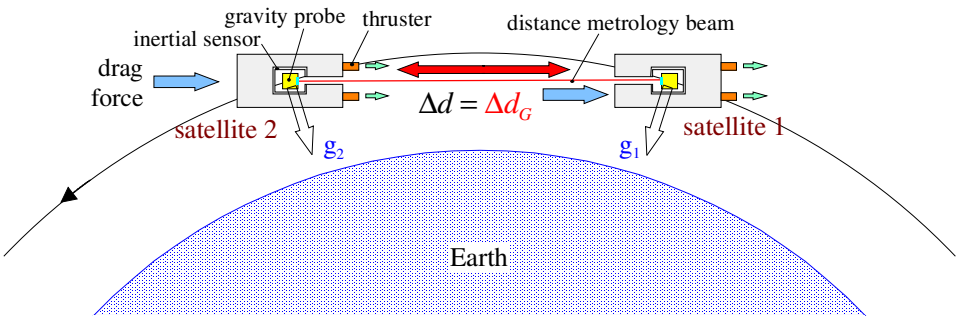

Figure 3.1-2 : Low-low satellite-to-satellite tracking concept (inertial sensor)

3.2 Top-Level Measurement Requirements for the ll-SST Observables

3.2.1 Satellite-to-Satellite Distance Measurement Requirement

The first fundamental physical observable of the II-SST technique is the distance d between the COMs of the two satellites. It is not mandatory to know accurately its absolute value, but its variation must be measured with very high resolution. In fact, the model of the Earth gravity field (and of its time variable part) is obtained from the variation that it produces on the relative distance between the satellites.

The error propagation from the physical observables to the geopotential spherical harmonics [RD-12] shows that the scientific objectives of the mission can be fulfilled for

- a distance d = 100 km measured with a relative error ≤$2\cdot10^{-13}$ 1/√Hz (absolute error ≤20 nm/√Hz),

or

- a distance d = 50 km measured with a relative error ≤$4\cdot10^{-13}$ 1/√Hz (absolute error ≤20 nm/√Hz).

For achieving such a distance measurement performance, the use of an optical metrology (laser interferometer) is mandatory. The ultimate limit of this metrology is given by the stability of the frequency of the laser source feeding the interferometer. The spectrum of the stabilized laser frequency is not always flat but shows nearly $1/f$ behaviour at low frequencies; consequently the distance variation measurement noise is not white. The corner frequency at which the transition from the flat noise to the $1/f$ noise occurs is set to 0.01 Hz from the typical shape of the spectrum of a stabilized laser frequency (see section 4.1).

The requirement on the satellite-to-satellite distance measurement error spectral density can be therefore expressed in function of frequency as (see also Figure 3.2-1):

$$\delta\tilde{d}(f) \le \begin{cases} 20\cdot10^{-9} & \text{for } f \ge 0.01\,\text{Hz} \\ 20\cdot10^{-9}\cdot\left(\dfrac{0.01}{f}\right) & \text{for } f < 0.01\,\text{Hz} \end{cases} \quad \frac{\text{m}}{\sqrt{\text{Hz}}} \qquad (3.2.1)$$

A similar coloured noise for the distance variation measurement error has been considered also in [RD-12].

The requirement (3.2.1) applies to a satellite-to-satellite distance d included between 50 km and 100 km.

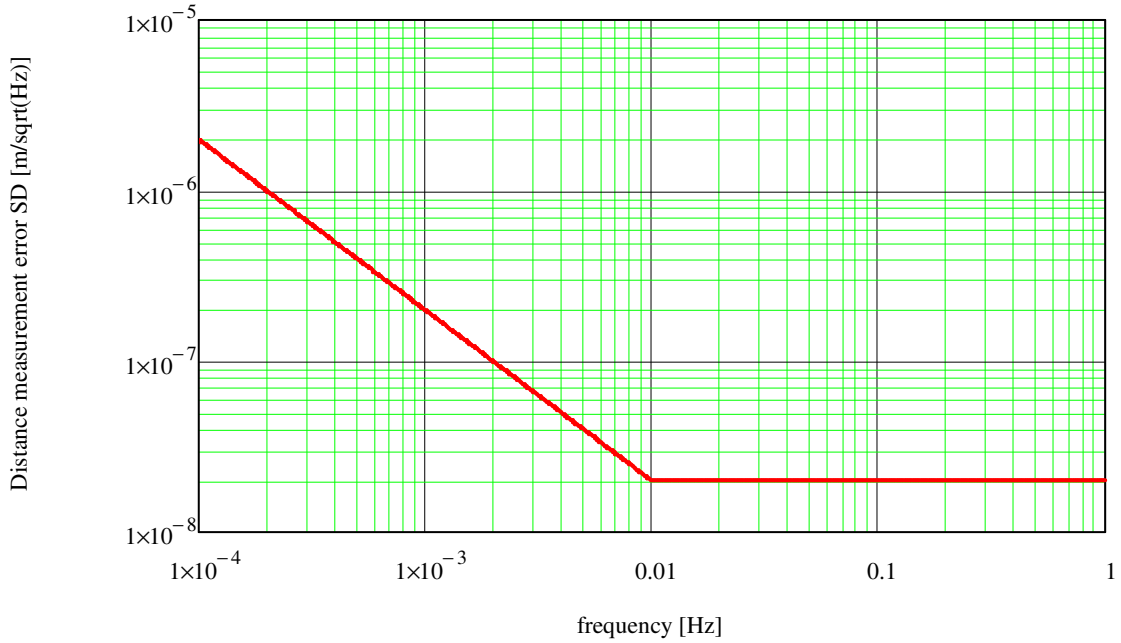

Figure 3.2-1 : Upper limit to the measurement error spectral density of the satellite-to-satellite distance (applicable to a relative distance between 50 km and 100 km).

3.2.2 Non-Gravitational Acceleration Measurement Requirement

The second fundamental physical observable of the II-SST technique is the relative non-gravitational acceleration of the satellite COMs along the line joining the COMs themselves (i.e. the segment whose length variation is nominally measured by the distance metrology):

$$\Delta\ddot{d}_D = D_1 - D_2$$

In fact, the integration of $\Delta\ddot{d}_D$ provides the variation of the satellite-to-satellite distance Δd_D produced by non-gravitational (i.e. drag) forces. Subtracting Δd_D from the product of the distance metrology (Δd), the distance variation between the satellite COMs produced by the sole action of the gravity field is obtained:

$$\Delta d_G = \Delta d - \Delta d_D$$

The error propagation from the physical observables to the geopotential spherical harmonics [RD-12] shows that the relative non-gravitational acceleration shall be measured with a noise

floor <10^{-11} m/s^2/√Hz (in conjunction with the distance variation measurement performance specified before) to fulfil for the scientific objectives of the mission.

The quantity $\Delta\ddot{d}_D$ is measured by accelerometers placed on the two satellites. Typically, the measurement noise of an accelerometer is not flat at all frequencies. Taking as reference the shape of the GOCE accelerometer intrinsic noise, as derived from models and extrapolated from the flight data (see section 4.2, 5.3.2), the requirement on the relative non-gravitational acceleration measurement error spectral density has been expressed in function of frequency as (see also Figure 3.2-2):

$$\delta\tilde{\tilde{d}}_D(f) \le \begin{cases} 10^{-11} & \text{for } f \ge 0.001 \text{ and } f \le 0.01\,\text{Hz} \\ 10^{-11}\cdot\left(\dfrac{0.001}{f}\right)^2 & \text{for } f < 0.001\,\text{Hz} \\ 10^{-11}\cdot\left(\dfrac{f}{0.1}\right)^2 & \text{for } f > 0.1\,\text{Hz} \end{cases} \quad \frac{\text{m}}{\text{s}^2\sqrt{\text{Hz}}} \qquad (3.2.2)$$

The transition frequency from the flat noise to the $1/f^2$ noise (1 mHz) and to the f^2 noise (0.1 Hz) has been established from the accelerometer measurement model.

A similar coloured noise for the relative non-gravitational acceleration measurement error has been considered also in [RD-12].

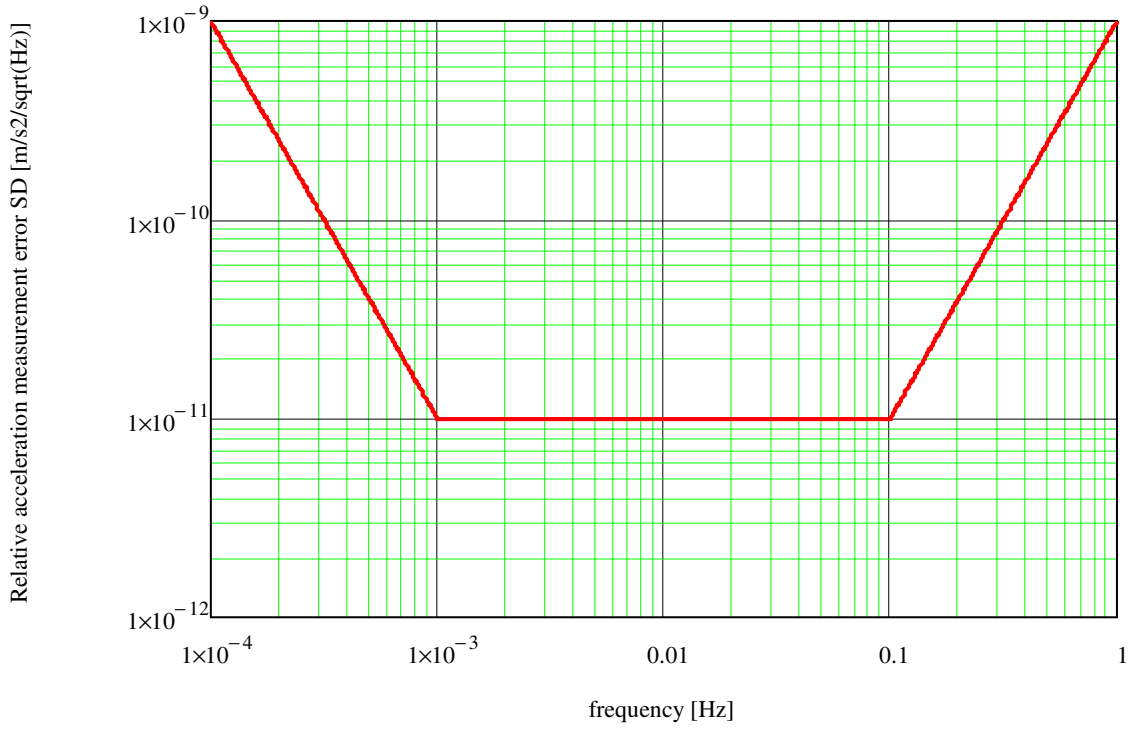

Figure 3.2-2 : Upper limit to the measurement error spectral density relative non-gravitational acceleration.

3.2.3 Combined Measurement Requirements

The distance variation and the relative non-gravitational acceleration measurements both concur to the mission scientific performance. It is therefore useful to translate the requirements (3.2.1) and (3.2.2) in the same unit in order to compare the relative contributions to the final performance.

Figure 3.2-3 shows the requirement (3.2.2) on $\delta\tilde{\ddot{d}}_D(f)$ superimposed to the requirement (3.2.1) on $\delta\tilde{d}(f)$ translated in relative acceleration by double derivation:

$$\delta\tilde{\ddot{d}}(f) = \delta\tilde{d}(f)\times(2\pi f)^2 \quad \frac{\mathrm{m}}{s^2\sqrt{\mathrm{Hz}}}$$

The total error on the relative acceleration obtained by adding quadratically $\delta\tilde{\ddot{d}}(f)$ and $\delta\tilde{\ddot{d}}_D(f)$ can be regarded as the measurement noise of the relative acceleration between the satellites caused by the Earth gravity field only:

$$\delta\tilde{\ddot{d}}_G(f) = \sqrt{\left(\delta\tilde{\ddot{d}}(f)\right)^2 + \left(\delta\tilde{\ddot{d}}_D(f)\right)^2} \quad \frac{\mathrm{m}}{s^2\sqrt{\mathrm{Hz}}}$$

Figure 3.2-4 shows the requirement on $\delta\tilde{\ddot{d}}_D(f)$ and $\delta\tilde{d}(f)$ both translated in range rate by integration and derivation respectively:

$$\delta\tilde{\dot{d}}_D(f) = \frac{\delta\tilde{\ddot{d}}_D(f)}{2\pi f} \quad \frac{\mathrm{m}}{s\sqrt{\mathrm{Hz}}}, \quad \delta\tilde{\dot{d}}(f) = \delta\tilde{d}(f)\times(2\pi f) \quad \frac{\mathrm{m}}{s\sqrt{\mathrm{Hz}}}$$

From the observation of the two plots the following considerations arise:

- The measurement error of the satellite-to-satellite distance variation becomes dominant for frequencies above 1 mHz. Therefore, for the purposes of the ll-SST technique, would be unnecessary to require that the noise of the relative non-gravitational acceleration measurement remains below 10^{-11} m/s^2/√Hz up to 0.1 Hz. However, since the accelerometers intrinsic noise is expected to remain below this threshold, it was not deemed necessary to specify a looser requirement, even to not limit a possible performance improvement at the higher frequencies in case of better than specified behaviour of the distance metrology above 1 mHz and/or to exploit the acceleration measurement in this frequency band for auxiliary gradiometry. This bearing in mind that a possible violation of the requirement on $\delta\tilde{\ddot{d}}_D(f)$ above 10 mHz wouldn't have important consequences on the mission scientific performance.

- The measurement error of the relative non-gravitational acceleration is by far dominating for frequencies <1 mHz, and therefore an even worse measurement of the relative distance variation would be tolerable. However, since the distance metrology intrinsic noise is expected to have a 1/f type physical behaviour of low-frequency, it was not deemed necessary to specify a looser requirement, even to not limit a possible

performance improvement at the lower frequencies in case of better than specified measurement relative non-gravitational acceleration below 1 mHz. This bearing in mind that a possible violation of the requirement on $\delta\tilde{d}(f)$ below 1 mHz wouldn't have important consequences on the mission scientific performance.

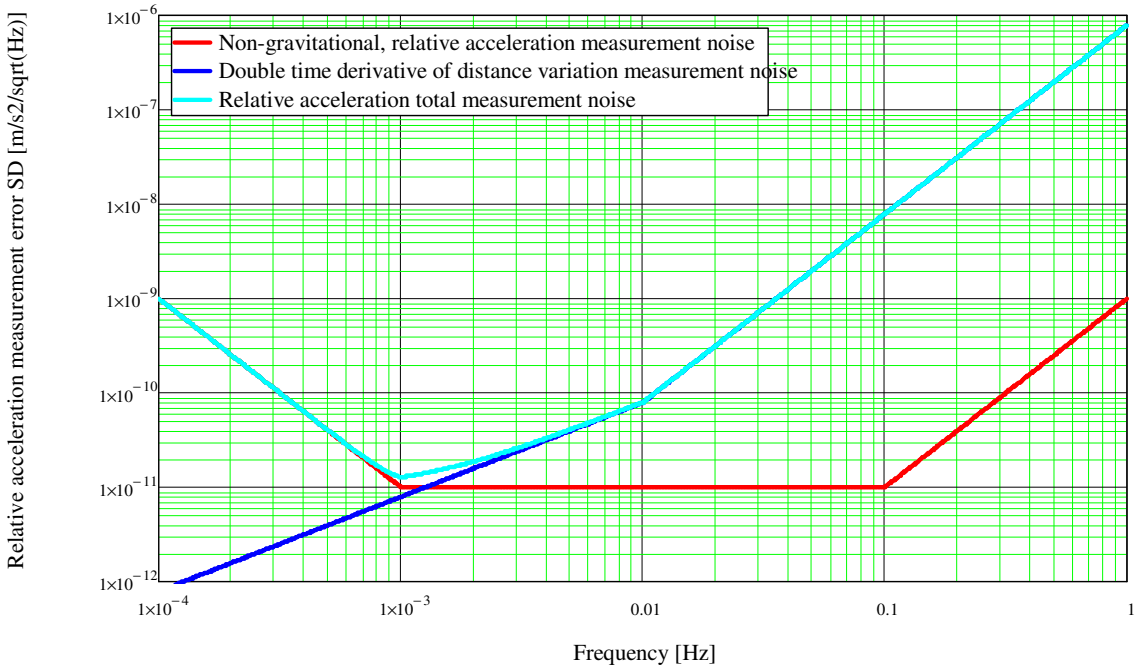

Figure 3.2-3 : Requirements on distance variation and relative non-gravitational acceleration measurement both expressed in relative acceleration.

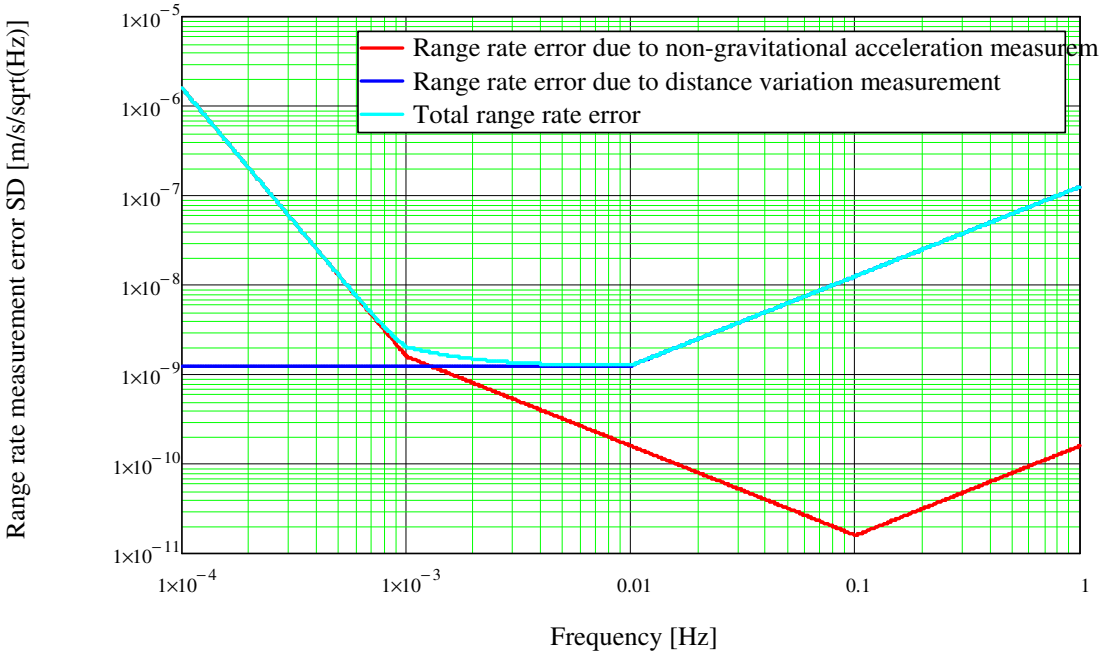

Figure 3.2-4 : Requirements on distance variation and relative non-gravitational acceleration measurement both expressed in range rate.

3.3 Satellite-to-Satellite Distance Measurement Model and Error Tree

A laser interferometer measures the distance variation (ΔL) between two optical references, schematized in Figure 3.3-1 by the retro-reflectors (RR) RR_1, RR_2. In general RR_1, RR_2 are not coincident with the COMs of the two satellites. Thus, any rotation of the satellite couples with the RR-COM offset and produces a variation of the distance measured by the interferometer. The knowledge of the RR offset from COM (unless this offset is kept almost null by construction) and of the satellite orientations relative to the satellite-to-satellite line are therefore necessary, in addition to the interferometer output, for obtaining the estimation ($\Delta\hat{d}$) of the distance variation between the COMs (Δd). With reference to Figure 3.3-1 and assuming that the RR doesn't move relative to the COM, we can approximately express $\Delta\hat{d}$ as follows [RD-5]:

$$\Delta\hat{d} \cong \Delta\hat{L} - \Delta\hat{\psi}_1 \hat{r}_{A,Y} + \Delta\hat{\theta}_1 \hat{r}_{A,Z} + \Delta\hat{\psi}_2 \hat{r}_{B,Y} - \Delta\hat{\theta}_2 \hat{r}_{B,Z} \quad (3.3.1)$$

where:

- $\Delta\hat{L}$ = distance variation between RR_1, RR_2 measured by the laser interferometer,
- $\hat{r}_{A,Y}$, $\hat{r}_{A,Z}$ ($\hat{r}_{B,Y}$, $\hat{r}_{C,Z}$) = offset between the S1 (S2) COM and the retro-reflector RR_1 (RR_2) along the Y, Z axes, known from on-ground and in-flight measurements,
- $\Delta\hat{\theta}_1$, $\Delta\hat{\psi}_1$ ($\Delta\hat{\theta}_2$, $\Delta\hat{\psi}_2$) = variation of the rotation angles of the S1 (S2) Satellite Reference Frame (SRF) in the Satellite-to-Satellite Reference Frame (SSRF, defined with reference to the satellite-to-satellite line), measured by a suitable angle metrology.

The estimation error of the distance variation between the satellites COMs (δd) depends on the errors by which the various terms of the (3.3.1) are measured and by the terms which have been neglected in the (3.3.1).

$$\delta d = \delta L - \delta\Delta\psi_1 r_{A,Y} - \Delta\psi_1 \delta r_{A,Y} + \delta\Delta\theta_1 r_{A,Z} + \Delta\theta_1 \delta r_{A,Z} + \delta\Delta\psi_2 r_{B,Y} + \Delta\psi_2 \delta r_{B,Y} - \delta\Delta\theta_2 r_{B,Z} - \Delta\theta_2 \delta r_{B,Z} + \Delta r_{A,X} - \Delta r_{B,X} + \delta d_J \quad (3.3.2)$$

where:

- δL = measurement error of ΔL.
- $\delta r_{A,Y}$, $\delta r_{A,Z}$ ($\delta r_{B,Y}$, $\delta r_{B,Z}$) = measurement error of $r_{A,Y}$, $r_{A,Z}$ ($r_{B,Y}$, $r_{B,Z}$).
- $\delta\Delta\theta_1$, $\delta\Delta\psi_1$ ($\delta\Delta\theta_2$, $\delta\Delta\psi_2$) = measurement error of $\Delta\theta_1$, $\Delta\psi_1$ ($\Delta\theta_2$, $\Delta\psi_2$).
- $\Delta r_{A,X}$ ($\Delta r_{B,X}$) = variation of the retro-reflector RR_1 (RR_2) position along X axis (~laser interferometer measurement line), neglected in the (3.3.1).

Another error contribution (denoted in the (3.3.2) by δd_J) is due to the coupling of the laser beam pointing jitter with the far-field wavefront distortions. The situation is illustrated in Figure 3.3-2: if the far-field wavefront of the laser beam emitted by the S1 is not a perfect sphere centered on the emission point (as it happens in practice), then angular jitter of the laser beam couples with the deviations from the spherical shape (wavefront errors) giving rise to apparent variation to the interferometer phase, and of the satellite-satellite distance measured by the interferometer.

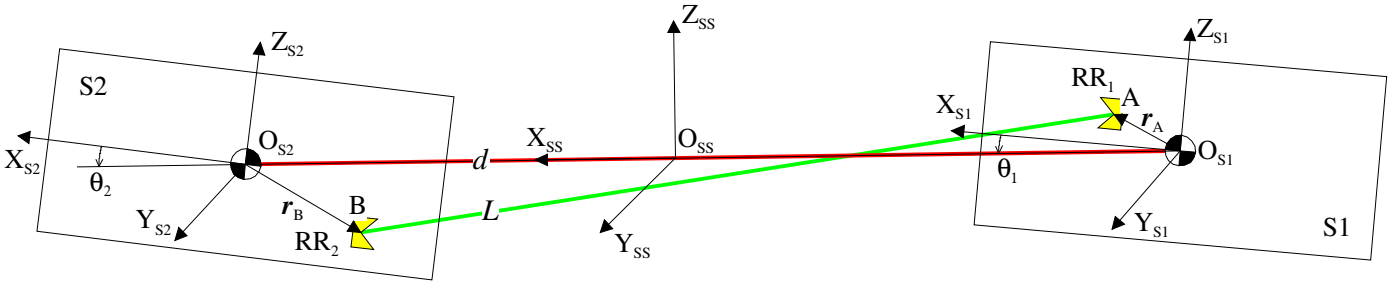

Figure 3.3-1 : Basic scheme of the distance measurement between the satellite COMs.

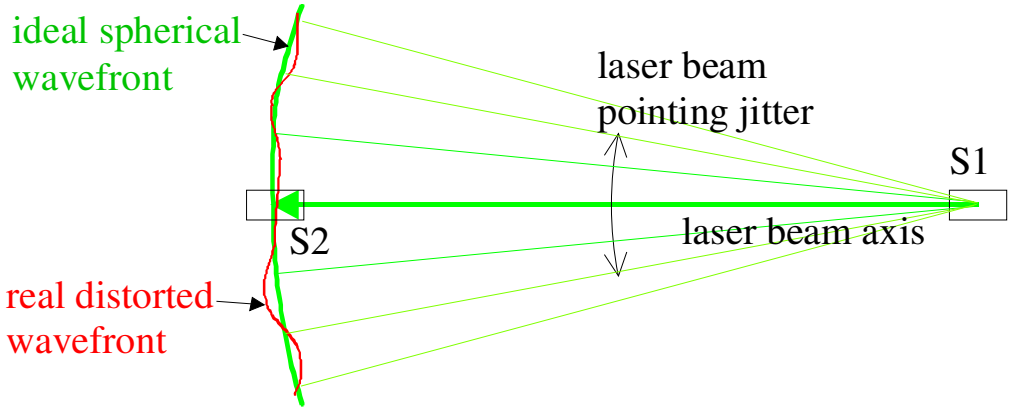

Figure 3.3-2 : Principle of the laser beam wavefront distortion coupling with the pointing jitter.

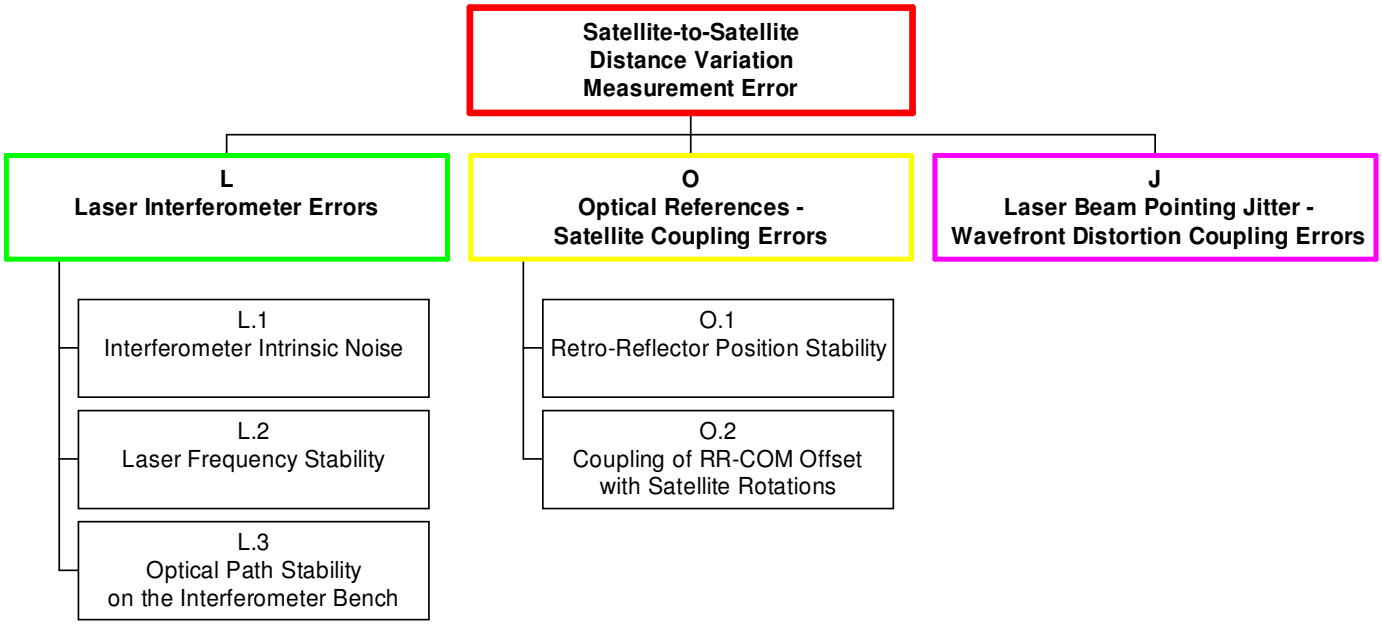

Figure 3.3-3 : First-level error tree for the satellite-to-satellite distance variation measurement.

The error terms of the (3.3.2) can be organized in an error tree as shown in Figure 3.3-3.
The "Laser Interferometer Errors" category includes all the errors affecting the measurement of ΔL:

- intrinsic noise of the laser interferometer;
- frequency stability of the laser source;
- stability of the optical path travelled by the laser beam on the interferometer bench.

The "Optical References – Satellite Coupling Errors" category includes:

- stability of the position of the RR relative to the COM ($\Delta r_{A,X}$, $\Delta r_{B,X}$)
- coupling between the RR-COM offset and the rotations of the satellites relative to the SSRF ($\delta\Delta\psi_1\ r_{A,Y}$, $\Delta\psi_1\ \delta r_{A,Y}$, $\delta\Delta\theta_1\ r_{A,Z}$, $\Delta\theta_1\ \delta r_{A,Z}$, $\delta\Delta\psi_2\ r_{B,Y}$, $\Delta\psi_2\ \delta r_{B,Y}$, $\delta\Delta\theta_2\ r_{B,Z}$, $\Delta\theta_2\ \delta r_{B,Z}$).

The last category is for the error contribution arising from the coupling of the laser beam pointing jitter with the far-field wavefront distortions.

This brief analysis shows that the distance metrology (i.e. the laser interferometer) is only one of the contributions to the overall measurement error of Δd. Therefore, its performance shall be better than requirement (3.2.1) specified for $\delta\tilde{d}(f)$. For the purpose of the distance metrology technology review and assessment, half of the requirement (3.2.1) is preliminarily allocated to the contribution of the interferometer intrinsic noise, which therefore reads (see Figure 3.3-4):

$$\delta\tilde{d}_{L.1}(f) < \begin{cases} 10\cdot 10^{-9} & \text{for } f \geq 0.01\ \text{Hz} \\ 10\cdot 10^{-9}\cdot\left(\dfrac{0.01}{f}\right) & \text{for } f < 0.01\ \text{Hz} \end{cases} \quad \frac{\text{m}}{\sqrt{\text{Hz}}} \qquad (3.3.3)$$

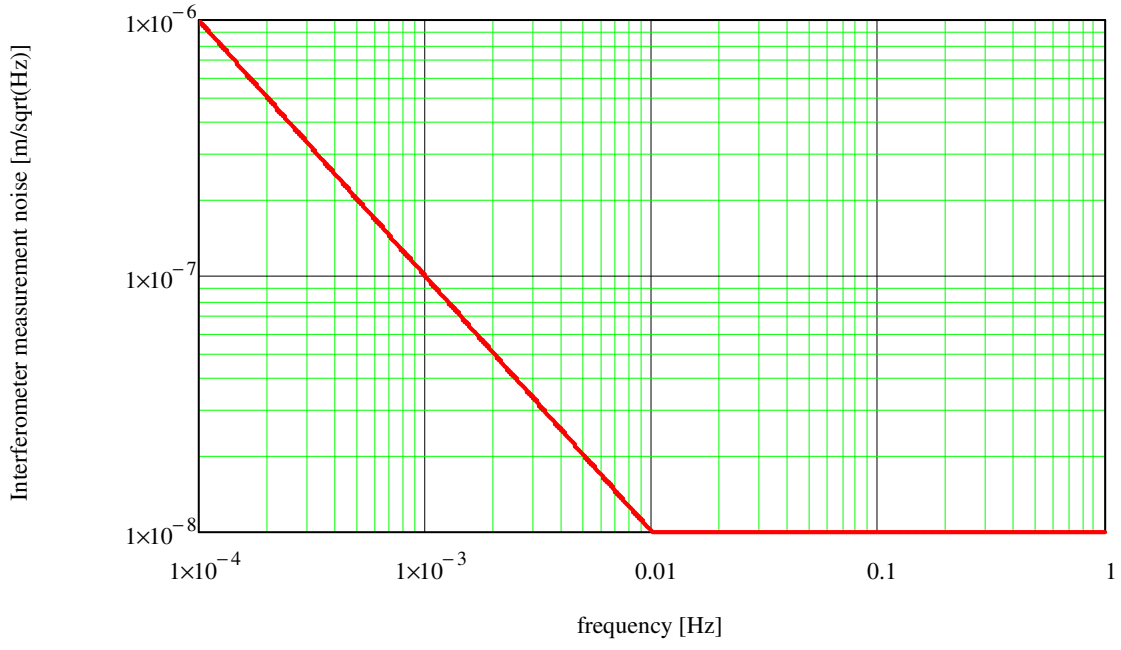

Figure 3.3-4 : Preliminary requirement on the laser interferometer noise.

3.4 Non-Gravitational Acceleration Measurement Model and Error Tree

Each satellite (S1, S2) shall carry at least an accelerometer (in general, a set of accelerometers) denoted as A_1 in Figure 3.4-1 for measuring the non-gravitational acceleration of the COM. In general the centre of the proof mass of A_1 is not coincident with the COM of the satellite. Thus, in addition to the non-gravitational acceleration, A_1 is subject to the gravity gradient, the centrifugal acceleration and the angular acceleration. Moreover, the variations of the offset between A_1 and the COM (due to thermo-elastic deformations of the structure of COM shifts) produce accelerations on A_1, directly or as the Coriolis accelerations. The list of the accelerations experienced by A_1 is completed by the gravity acceleration produced by the satellite masses (self gravity) and by the accelerations originated by possible couplings of electro-magnetic nature between accelerometer and environment (satellite and external).
With reference to Figure 3.4-1 we can express the total acceleration experienced by the proof mass of the accelerometer A_1 relatively to its cage as follows [RD-5]:

$$\underline{a}_1 = -([V] - [\Omega^2] - [\dot{\Omega}])\underline{r}_1 + 2[\Omega]\dot{\underline{r}}_1 + \ddot{\underline{r}}_1 + \underline{D}_1 - \underline{MS}_1 \quad (3.4.1)$$

where:

- $\underline{r}_1$, $\dot{\underline{r}}_1$, $\ddot{\underline{r}}_1$ = position of the centre of A_1 relative to the satellite COM and its time derivatives,
- $[V]$ = gravity gradient tensor (GGT): $[V] = \begin{pmatrix} V_{XX} & V_{XY} & V_{XZ} \\ V_{XY} & V_{YY} & V_{YZ} \\ V_{XZ} & V_{YZ} & V_{ZZ} \end{pmatrix}$, $V_{ij} = \frac{\partial^2 V}{\partial r_i \partial r_j}$ $i, j = X, Y, Z$,
- $[\Omega]$, $[\Omega^2]$, $[\dot{\Omega}]$ = angular rate matrix and its square, angular acceleration matrix:

$$[\Omega] = \begin{pmatrix} 0 & -\omega_Z & \omega_Y \\ \omega_Z & 0 & -\omega_X \\ -\omega_Y & \omega_X & 0 \end{pmatrix}, [\Omega^2] = \begin{pmatrix} -\omega_Z^2 - \omega_Y^2 & \omega_X\omega_Y & \omega_X\omega_Z \\ \omega_X\omega_Y & -\omega_Z^2 - \omega_X^2 & \omega_Y\omega_Z \\ \omega_X\omega_Z & \omega_Y\omega_Z & -\omega_X^2 - \omega_Y^2 \end{pmatrix}, [\dot{\Omega}] = \begin{pmatrix} 0 & -\dot{\omega}_Z & \dot{\omega}_Y \\ \dot{\omega}_Z & 0 & -\dot{\omega}_X \\ -\dot{\omega}_Y & \dot{\omega}_X & 0 \end{pmatrix}$$

- $\underline{D}_1$ = non-gravitational acceleration of the satellite S1 COM,
- $\underline{MS}_1$ = accelerations due to satellite self-gravity electro-magnetic couplings.

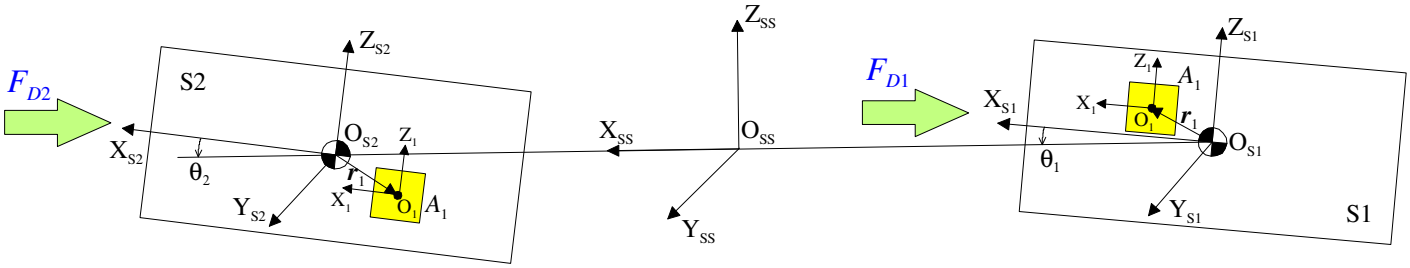

Figure 3.4-1 : Basic scheme of the relative non-gravitational acceleration measurement.

The output of the accelerometer A_1, i.e. the measurement of the acceleration $\underline{a}_1$, is affected by its transfer function (that includes at least a bias, a scale factor and a non-linear term), its noise and the coupling between the measurement axes. Moreover the sensitive axes of the accelerometer are not aligned to those of the satellite. Therefore, the acceleration $\underline{a}_1$ is measured by the accelerometer A_1 in its Accelerometer Reference Frame (ARF) as:

$$\underline{a}'_1 = ([1]_3 + [d\mathrm{K}]_1 + [d\mathrm{R}]_1 + [d\mathrm{S}]_1)\cdot\underline{a}_1 + [\mathrm{K2}]_1\cdot\underline{a}_1^{\,2} + \underline{b}_1 + \underline{n}_1 \equiv [\mathrm{M}]_1\cdot\underline{a}_1 + [\mathrm{K2}]_1\cdot\underline{a}_1^{\,2} + \underline{b}_1 + \underline{n}_1 \quad (3.4.2)$$

where

- $[d\mathrm{K}]_1 = \begin{pmatrix} K_{1,\mathrm{X}} & 0 & 0 \\ 0 & K_{1,\mathrm{Y}} & 0 \\ 0 & 0 & K_{1,\mathrm{Z}} \end{pmatrix}$, $K_{1,\mathrm{X}}$, $K_{1,\mathrm{Y}}$, $K_{1,\mathrm{Z}}$ = deviation from the unitary value of the scale factors of the accelerometer A_i along the X_{A1}, Y_{A1}, Z_{A1} axes.
- $[d\mathrm{R}]_1 = \begin{pmatrix} 0 & \psi_{A1} & -\theta_{A1} \\ -\psi_{A1} & 0 & \varphi_{A1} \\ \theta_{A1} & -\varphi_{A1} & 0 \end{pmatrix}$, φ_{A1}, θ_{A1}, ψ_{A1} = misalignment of the ARF relative to the SRF around the X_{A1}, Y_{A1}, Z_{A1} axes.
- $[d\mathrm{S}]_1 = \begin{pmatrix} 0 & \varepsilon_{A1} & \eta_{A1} \\ \varepsilon_{A1} & 0 & \varsigma_{A1} \\ \eta_{A1} & \varsigma_{A1} & 0 \end{pmatrix}$, ε_{A1}, η_{A1}, ζ_{A1} = cross coupling factors of the sensitive axes of the accelerometer A_1 (ε_{A1} = $\mathrm{X}_{A1} \leftrightarrow \mathrm{Y}_{A1}$ coupling factor, η_{A1} = $\mathrm{X}_{A1} \leftrightarrow \mathrm{Z}_{A1}$ coupling factor, ζ_{A1} = $\mathrm{Y}_{A1} \leftrightarrow \mathrm{Z}_{A1}$ coupling factor).
- $[\mathrm{M}]_1 = [1]_3 + [d\mathrm{K}]_1 + [d\mathrm{R}]_1 + [d\mathrm{S}]_1 = \begin{pmatrix} 1+K_{1,\mathrm{X}} & \psi_{A1}+\varepsilon_{A1} & -\theta_{A1}+\eta_{A1} \\ -\psi_{A1}+\varepsilon_{A1} & 1+K_{1,\mathrm{Y}} & \varphi_{A1}+\varsigma_{A1} \\ \theta_{A1}+\eta_{A1} & -\varphi_{A1}+\varsigma_{A1} & 1+K_{1,\mathrm{Z}} \end{pmatrix} = [1]_3 + [d\mathrm{M}]_1$
- $[\mathrm{K2}]_1 = \begin{pmatrix} K2_{1,\mathrm{X}} & 0 & 0 \\ 0 & K2_{1,\mathrm{Y}} & 0 \\ 0 & 0 & K2_{1,\mathrm{Z}} \end{pmatrix}$, $K2_{1,\mathrm{X}}$, $K2_{1,\mathrm{Y}}$, $K2_{1,\mathrm{Z}}$ non-linear (quadratic) factors of the accelerometer A_1 along the X_{A1}, Y_{A1}, Z_{A1} axes.
- $\underline{b}_1 = \begin{pmatrix} b_{1,\mathrm{X}} \\ b_{1,\mathrm{Y}} \\ b_{1,\mathrm{Z}} \end{pmatrix}$, $b_{1,\mathrm{X}}$, $b_{1,\mathrm{Y}}$, $b_{1,\mathrm{Z}}$ = biases of the accelerometer A_1 along the X_{A1}, Y_{A1}, Z_{A1} axes.
- $\underline{n}_1 = \begin{pmatrix} n_{1,\mathrm{X}} \\ n_{1,\mathrm{Y}} \\ n_{1,\mathrm{Z}} \end{pmatrix}$, $n_{1,\mathrm{X}}$, $n_{1,\mathrm{Y}}$, $n_{1,\mathrm{Z}}$ = noises of the accelerometer A_1 along the X_{A1}, Y_{A1}, Z_{A1} axes.

The knowledge of the "calibration matrix" $[M]_1$ is therefore necessary for obtaining the estimation ($\hat{\underline{a}}_1$) of the acceleration ($\underline{a}'_1$) measured by A_1:

$$\hat{\underline{a}}_1 = [\hat{M}I]_1 \cdot \underline{a}'_1 \cong \underline{a}_1 + [K2]_1 \cdot \underline{a}_1^2 + \underline{n}_1 + [\delta MI]_1 \cdot \underline{a}_1 \quad (3.4.3)$$

where $[\hat{M}I]_1$ is the estimated "inverse calibration matrix", i.e. the inverse of the matrix $[M]_1$ obtained from in-fight measurements of the accelerometer scale factors, axes misalignments and couplings (accelerometer in-flight calibration), and $[\delta MI]_1$ is the error in the $[\hat{M}I]_1$ estimation. The acceleration $\hat{\underline{a}}_1$ so obtained can be regarded as an estimate of the non-gravitational acceleration $\underline{D}_1$ in the Satellite Reference Frame, if the other terms in the (3.4.1) and the terms $[K2]_1 \cdot \underline{a}_1^2$, $\underline{n}_1$, $[\delta MI]_1 \cdot \underline{a}_1$ in the (3.4.3) are small:

$$\hat{\underline{D}}_1 = \begin{pmatrix} \hat{D}_{1SRFX} \\ \hat{D}_{1SRFY} \\ \hat{D}_{1SRFZ} \end{pmatrix} \cong \hat{\underline{a}}_1 = [\hat{M}I]_1 \underline{a}'_1 = \underline{D}_1 + \delta\underline{D}_1 \quad (3.4.4)$$

The term $\delta\underline{D}_1$ in the (3.4.4) represents the error committed in the estimation of $\underline{D}_1$ in the SRF:

$$\delta\underline{D}_1 = \begin{pmatrix} \delta D_{1SRFX} \\ \delta D_{1SRFY} \\ \delta D_{1SRFZ} \end{pmatrix} = ([V] - [\Omega^2] - [\dot{\Omega}])\underline{r}_1 - 2[\Omega]\dot{\underline{r}}_1 - \ddot{\underline{r}}_1 + \underline{MS}_1 + [K2]_1 \cdot \underline{a}_1^2 + \underline{n}_1 + [\delta MI]_1 \cdot \underline{a}_1 \quad (3.4.5)$$

Analogously, a similar expression can be derived for the measurement of the non-gravitational acceleration of the Satellite S2 COM in the SRF of the accelerometers A_1 installed on Satellite 2. The so obtained components of the non-gravitational acceleration must be then transformed from the SRF to the SSRF, using the rotation matrices $[R]_{SSRF,SRF1}$, $[R]_{SSRF,SRF2}$. The difference between the components along the SSRF X axis (i.e., along the line joining the two satellites) of the non-gravitational accelerations of the two satellites is the estimation of the quantity $\Delta\ddot{d}_D$ sought for:

$$\Delta\hat{\ddot{d}}_D = \hat{D}_{1SSX} - \hat{D}_{2SSX} = \left[[\hat{R}]_{SSRF,SRF1} \cdot \begin{pmatrix} \hat{D}_{1SRFX} \\ \hat{D}_{1SRFY} \\ \hat{D}_{1SRFZ} \end{pmatrix} \right]_X - \left[[\hat{R}]_{SSRF,SRF2} \cdot \begin{pmatrix} \hat{D}_{2SRFX} \\ \hat{D}_{2SRFY} \\ \hat{D}_{2SRFZ} \end{pmatrix} \right]_X \quad (3.4.6)$$

The error affecting this estimate is:

$$\delta\ddot{d}_D = \delta D_{1SSX} - \delta D_{2SSX} \quad (3.4.7)$$

$$\delta D_{1SSX} = \delta D_{1SRFX} - (\psi_1 \, \delta D_{1SRFY} + \delta\psi_1 \, D_{1SRFY}) + (\theta_1 \, \delta D_{1SRFZ} + \delta\theta_1 \, D_{1SRFZ})$$

$$\delta D_{2SSX} = \delta D_{2SRFX} - (\psi_2 \, \delta D_{2SRFY} + \delta\psi_2 \, D_{2SRFY}) + (\theta_2 \, \delta D_{2SRFZ} + \delta\theta_2 \, D_{2SRFZ})$$

where $\delta\theta_1$, $\delta\psi_1$ ($\delta\psi_2$, $\delta\theta_2$) are the measurement error of rotation angles θ_1, ψ_1 (ψ_2, θ_2) defining the orientation of the SRF of S1 and S2 in the SSRF.

The errors affecting the measurement of D_{1SSX} (D_{2SSX}) can be grouped in the following main categories:

- Accelerometers Intrinsic Measurement Noise (I), produced by the sensing and control system of the proof mass motion and by the readout chain.
- Accelerometer-Satellite Coupling Errors (C), depending on the interaction of the accelerometer (through its scale factor, misalignment in the SRF, quadratic factor) with the satellite and mission environment (linear and angular accelerations of the satellite, gravity gradient).
- Satellite Generated Errors (S), depending on the satellite only (position and stability of the COM, variable self-gravity field produced by the satellite masses).
- Transformation Errors (T), related to the transformation of the components of $\underline{D}_1$ ($\underline{D}_2$) from the ARF, in which they are measured by the accelerometer A_1, to the SRF, and then from the SRF to the SSRF.

The tree of the non-gravitational differential acceleration measurement errors identified and classified in the previous sections is provided in Figure 3.4-2.

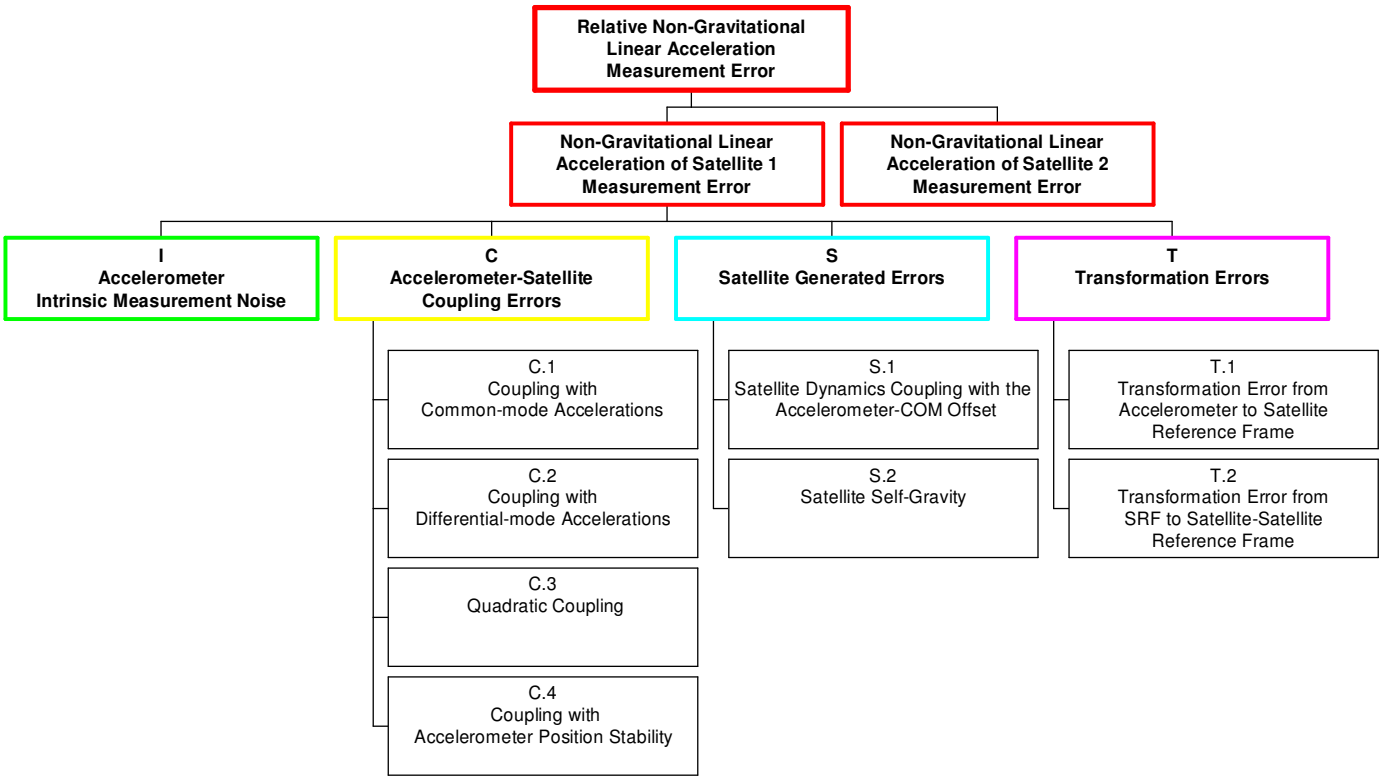

Figure 3.4-2 : First-level error tree for the relative non-gravitational acceleration measurement.

Being the accelerometer intrinsic measurement noise only one of the contributions to the overall measurement error of $\Delta\ddot{d}_D$, its performance shall be better than requirement (3.2.2) specified for $\delta\tilde{\ddot{d}}_D(f)$. For the purpose of the acceleration measurement technology review and assessment, 30% of the requirement (3.2.2) is preliminarily allocated to the contribution of the accelerometer intrinsic measurement noise, which therefore reads (see Figure 3.4-3):

$$\delta\tilde{\ddot{d}}_{D,I}(f) \leq \begin{cases} 3\cdot10^{-12} & \text{for } f \geq 0.001 \text{ and } f \leq 0.01\,\text{Hz} \\ 3\cdot10^{-12}\cdot\left(\dfrac{0.001}{f}\right)^2 & \text{for } f < 0.001\,\text{Hz} \\ 3\cdot10^{-12}\cdot\left(\dfrac{f}{0.1}\right)^2 & \text{for } f > 0.1\,\text{Hz} \end{cases} \quad \frac{\text{m}}{\text{s}^2\sqrt{\text{Hz}}} \qquad (3.4.8)$$

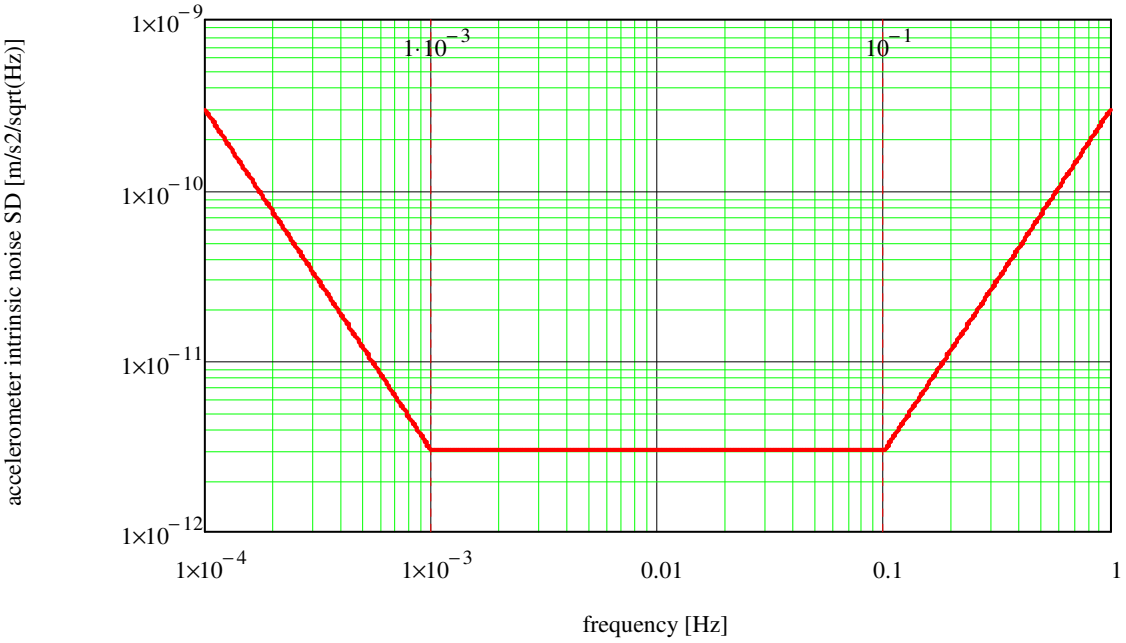

Figure 3.4-3 : Preliminary requirement on the accelerometer intrinsic measurement noise.

- Acceleration measurement accuracy (accelerometer bias): ≤2·10^{-7} m/s^2 (all axes)
- Accelerometer scale factor stability (all axes):

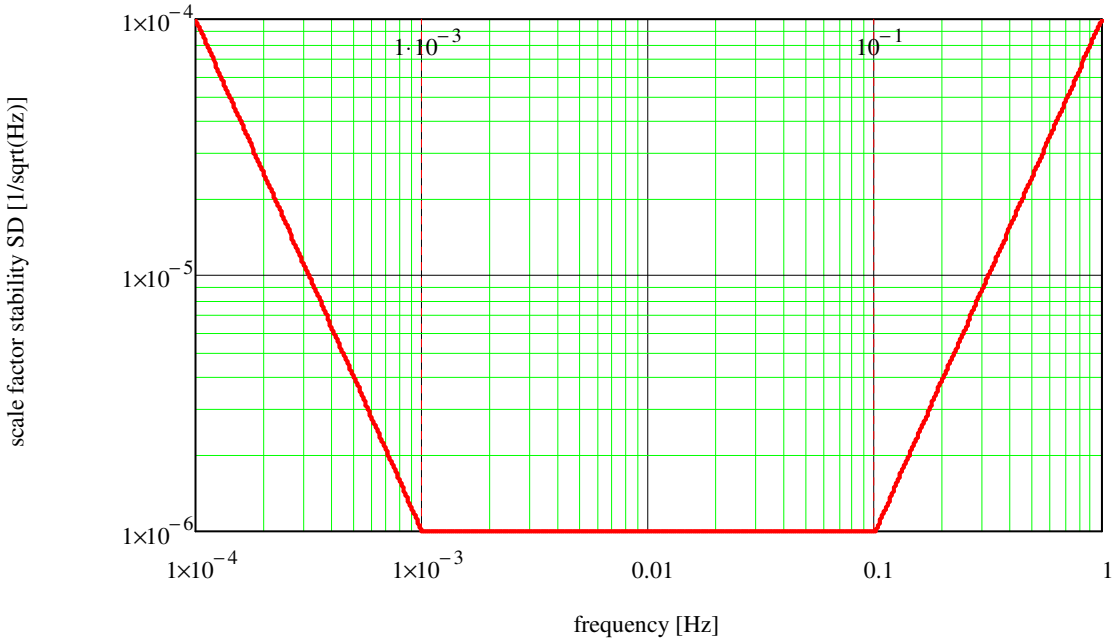

- Angular acceleration measurement noise (Y and Z axes):

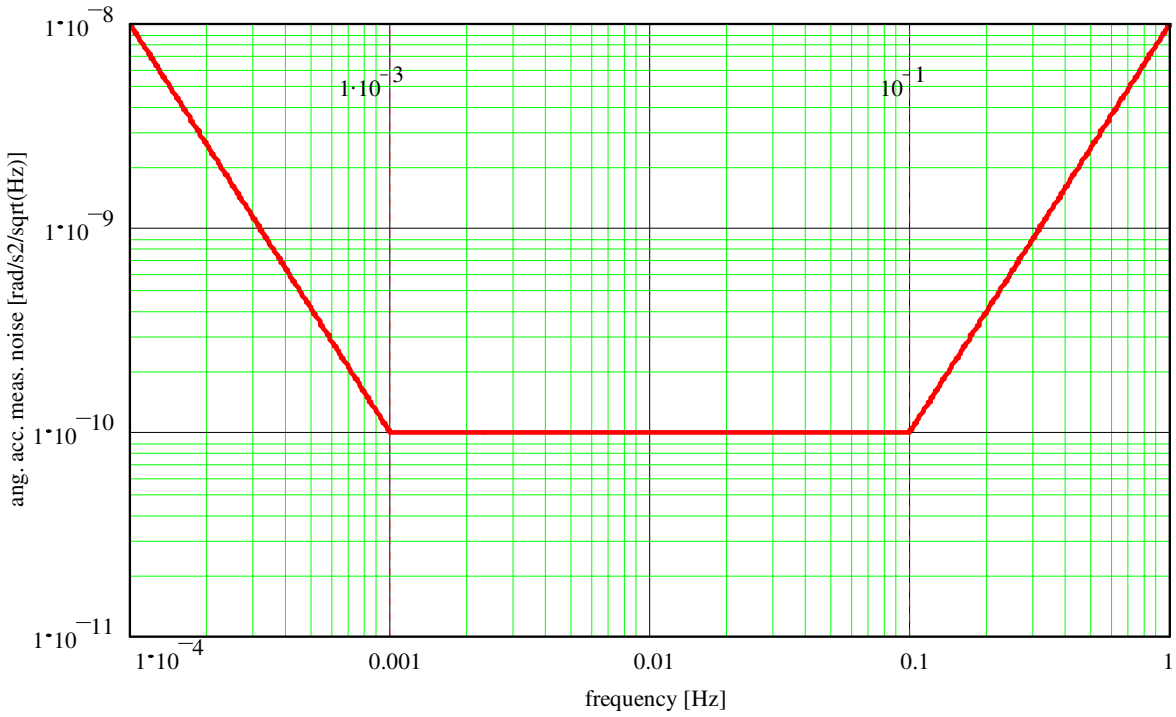

4. REVIEW AND RECOMMENDATION OF THE MEASUREMENT TECHNOLOGIES

4.1 Satellite-to-Satellite Optical Metrology Technologies Review

4.1.1 Distance metrology

In GRACE, the distance variation between the two satellites is provided by a "K-Band Ranging System (KBR)" consisting of K/Ka-band (ν = 24, 32 GHz, λ = 1.25, 0.94 cm) transmitters/ receivers integrated with JPL-developed BlackJack GPS receivers and ultra-stable oscillators. This metrology system (which essentially performs a phase measurement) can measure the distance variation rate with a noise level ≅ 1.0 µm/s/√Hz [RD-1],[RD-6] and the distance variation with an error ≅ 10 µm RMS [RD-9]. This distance measurement performance corresponds to a resolution of ~1/1000 of the RF wavelength utilized by the metrology. A straightforward way to improve the distance variation measurement is therefore to use a shorter wavelength. In particular, for achieving a resolution at nanometer level, a wavelength around 1 µm (~1000 x resolution) is necessary. In practice the RF metrology must be replaced by laser metrology (having typical wavelengths ~10,000 times smaller than typical microwave wavelengths). The need for replacing the K/Ka microwave instrument with laser metrology if the GRACE performances have to be improved by a factor >10, was already highlighted at the first workshop on Future Gravity Mission [RD-14].

Laser interferometry is by far the best technique for measuring long distance variations. Several interferometric schemes are possible, but all of them are based on the interference principle: the distance variation is obtained from the phase variation in the interference signal between two laser beams generated by the same source and travelling along different paths (one fixed, reference path and one from satellite to satellite) before their recombination. The heterodyne technique (consisting in applying a frequency shift between the two laser beams of the interferometer) is usually adopted in high-performance distance metrology because it allows to operate the photodiodes in AC mode (thus removing the DC noise and low-frequency drift of these devices) and to identify the sign of the distance variation. The laser interferometer becomes significantly more complex if a precise measurement of the absolute distance between the satellites is required. Since these needs within a NGGM can be satisfied by a differential GNSS technique (and the GNSS is a mandatory sensor on each satellite), it is unnecessary to charge the laser metrology with this additional function.

Among the various laser interferometer schemes, the heterodyne Michelson-type interferometer (whose basic scheme and working principle is shown in Figure 4.1-1) is the most appropriate for measuring the distance variation between two satellites several kilometres apart. This interferometer type has been proposed for LISA [RD-20], [RD-21] and for the laser-based GRACE follow-on mission studied in US (also known with the name EX-5 [RD-15]).

So far, two versions of the heterodyne Michelson-type interferometer have been specifically designed, breadboarded and tested in view of an application for a NGGM.

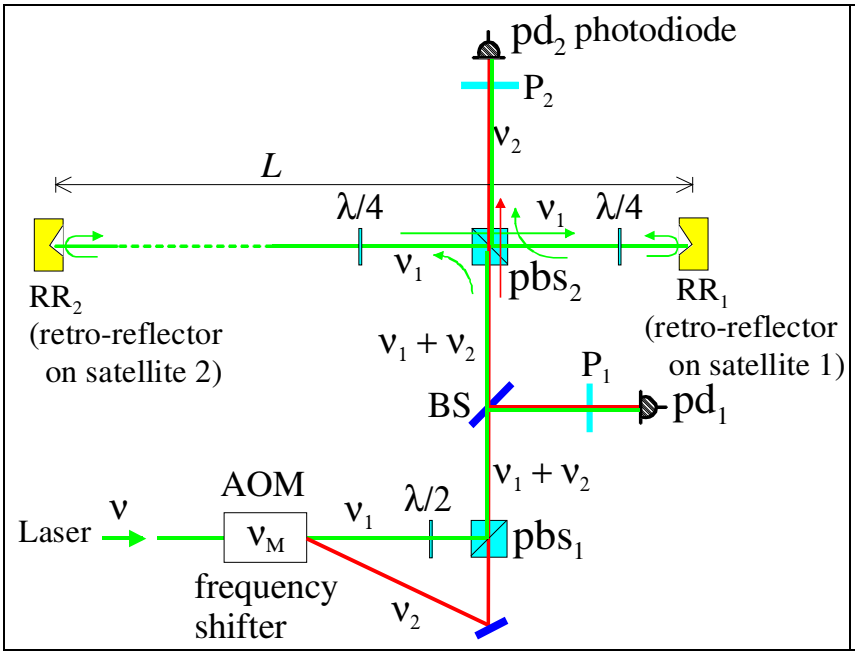

$\delta L = \frac{1}{2}\frac{\delta\phi}{2\pi}\lambda$: distance variation

$\delta\phi = (\phi_1 - \phi_2)$: phase difference between the two optical paths travelled by the reference beam (with frequency ν_2) and the measurement beam (with frequency ν_1), obtained from the interference signals (S_{D1}, S_{D2}) on the two photodiodes (pd_1, pd_2).

$S_{D2} = 2I''\cdot\{1 + \cos[2\pi(\nu_1-\nu_2)t + \delta\phi]\}$
$S_{D1} = 2I'\cdot\{1 + \cos[2\pi(\nu_1-\nu_2)t]\}$
λ = laser wavelength
I', I'' = laser beam intensity on pd_1, pd_2

Figure 4.1-1: Basic scheme and working principle of the heterodyne Michelson interferometer for measuring the distance variation between two satellites.

The heterodyne Michelson interferometer developed by TAS-I in cooperation with the Italian Metrology Institute (INRIM) ([RD-3], [RD-4]) makes use of a single laser installed on the Satellite 1 and frequency stabilized, whose beam is sent to the Satellite 2 where it is passively retro-reflected by a “corner-cube” optical system, according to the classical scheme of Figure 4.1-1. The interference signal formed on the photodiode pd_2 is suitably mixed with that formed on the photodiode pd_1; the distance variation between the satellites (δL) is computed from the relative phase $\delta\phi$ between the two signals. By referring the phase measurement to the interference signal picked up by pd1 allows removing from the inter-satellite distance measurement the effects of phase variations that may occur outside the interferometer bench. A peculiarity of this interferometer consists in the periodic chopping (on-off switch) of the measurement laser beam (that sent to the Satellite 2) with a half-cycle period equal to the round-trip time between the two satellites (which can be measured by the interferometer itself). This operation makes applicable the passive retro-reflection scheme to the measurement of long distances, in which the amount of optical power returning from Satellite 2 is a small fraction of that that leaks through the polarizing beam-splitter pbs_2 and reaches directly the photodiode pd_2, without taking the round-trip path. The chopping of the measurement beam is achieved through a fiber-coupled acousto-optic amplitude modulator.
The tests performed on the breadboard of this metrology system demonstrated an intrinsic measurement noise with spectral density <1 nm/√Hz above 0.01 Hz (see Figure 4.1-2).

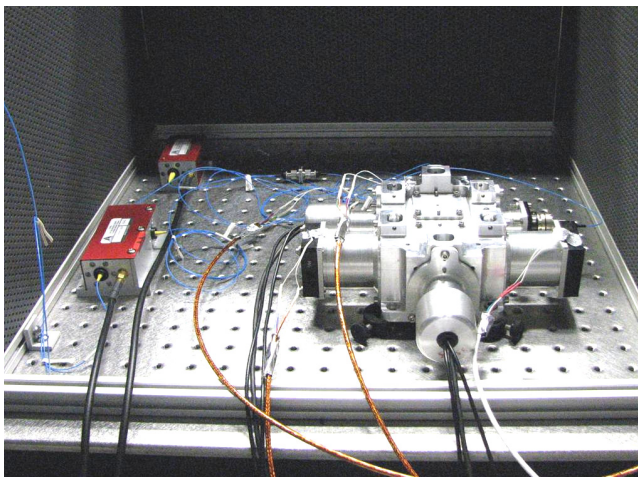

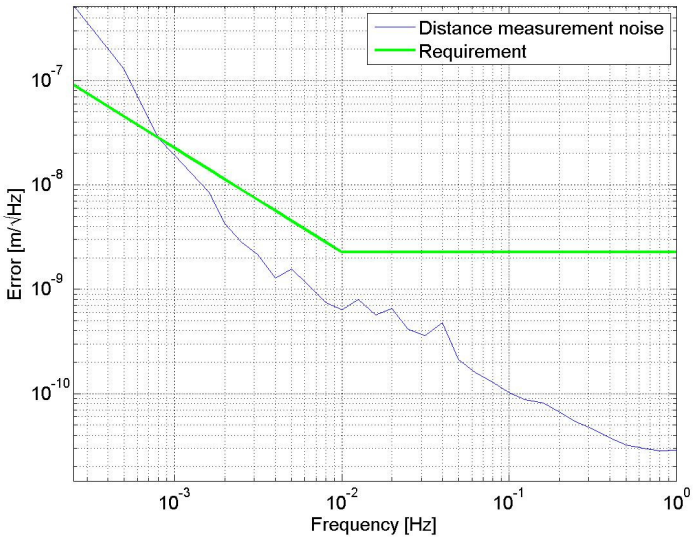

Figure 4.1-2: Breadboard and measured performance of the laser interferometer developed by TAS-I in preparation of a NGGM.

The version of the heterodyne Michelson-type interferometer developed by JILA and JPL in preparation of the GRACE follow-on EX-5 mission is based on a transceiver scheme (the same proposed for the LISA mission [RD-20], [RD-21]) which is particularly suitable for measurements at very long distances, because it allows to “regenerate” the weak signal coming from the far satellite before sending it back, yet maintaining the phase information. It makes use of two lasers placed on the two spacecraft: the first (“master”) is frequency stabilized by means of an optical cavity and on a molecular reference (for short and long term stability respectively) and the second (“slave”) is phase-locked to the first one in “frequency-offset”. The “master” laser on the first spacecraft is sent through a refractive telescope towards the second spacecraft where the light is collected by a telescope, reflected on the proof mass and sent on a detector. Here it is mixed with a small amount of radiation coming from the “slave” laser creating a beat signal. This last is used to lock the “slave” to the “master” laser in order to maintain a fixed frequency offset. The radiation of the locked laser is then sent back towards the first spacecraft. where it is reflected on the second proof mass and sent on the detector where is mixed with a small amount of radiation coming from the master laser creating a beat signal, which provides the required measurement (see Figure 4.1-3).
The implementation of this scheme needs two laser sources simultaneously operating in order to perform the distance measurement, implying an increase of complexity and a decrease of reliability with respect to a scheme making use of a single laser source and a retro-reflector to send back the beam from the far satellite.

A breadboard to demonstrate the interferometer performance has been built [RD-16] making use of two 1064 nm Nd:YAG lasers, obtaining a distance measurement noise below 1 nm/√Hz from 30 mHz to 10 Hz (see Figure 4.1-4).

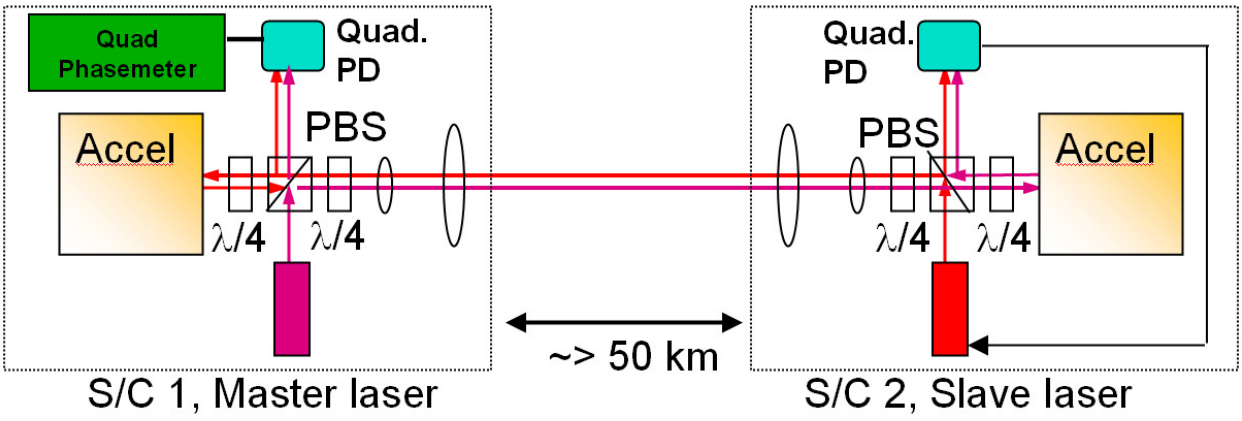

Figure 4.1-3: Laser interferometer concept for the EX-5 mission.

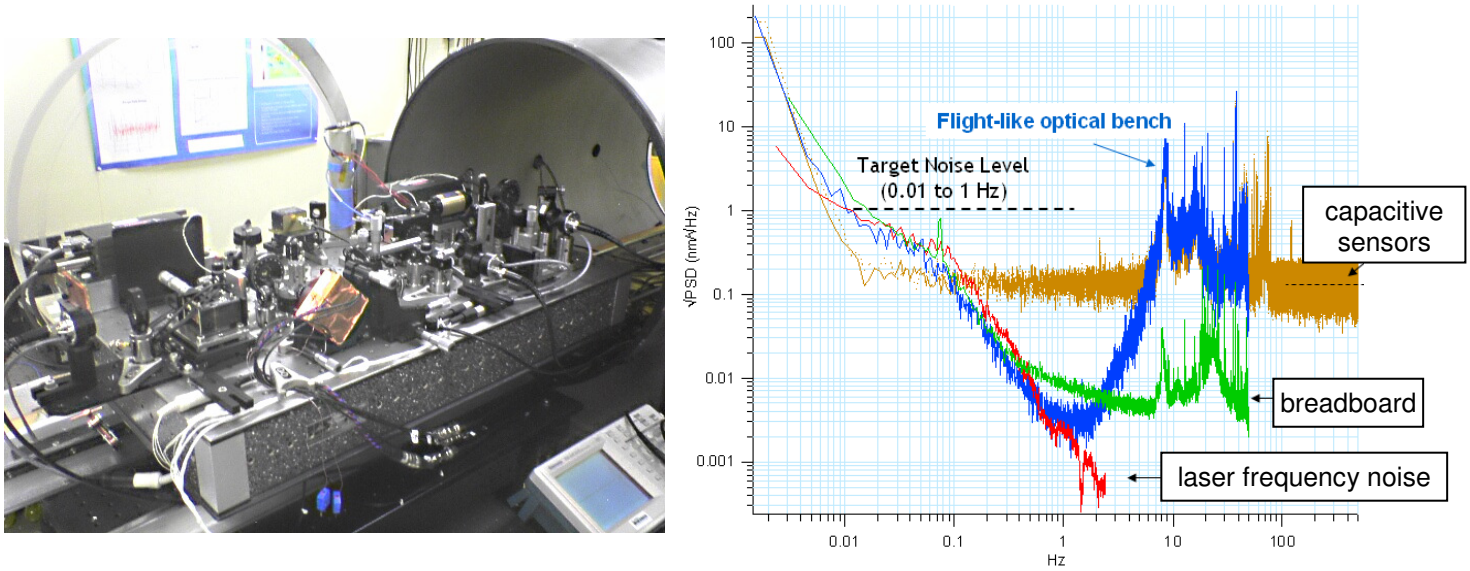

Figure 4.1-4: Breadboard and measured performance of the laser interferometer under development in preparation of the follow-on to the GRACE mission

4.1.2 Laser source frequency stability

At long distances, another factor limits the measurement performance below the intrinsic potential of the interferometer: the frequency stability of the laser source. In both the interferometers (JILA/JPL, TAS-I/INRIM) a variation of the laser frequency ($\delta\nu$) produces on the measurement the same effect of a distance variation (δL): $\delta L/L = \delta\nu/\nu$.

There are essentially two techniques that can be used for stabilizing the laser frequency (see Figure 4.1-5):

1) An optical resonator (or Fabry-Perot cavity, made by two faces spherical mirrors connected by a spacer) is kept dimensionally stable by proper material choice and precise temperature control. A fraction of the laser beam is injected in the resonator and its frequency is controlled in such a way as to maintain the resonance condition (integer number of half-wavelengths contained in the resonator).

2) A fraction of the laser beam is injected in a cell containing a gas (like iodine I_2) having at least an absorption line with the frequency within the laser tuning range. The laser frequency is controlled so as to maximize the excitation of that absorption.

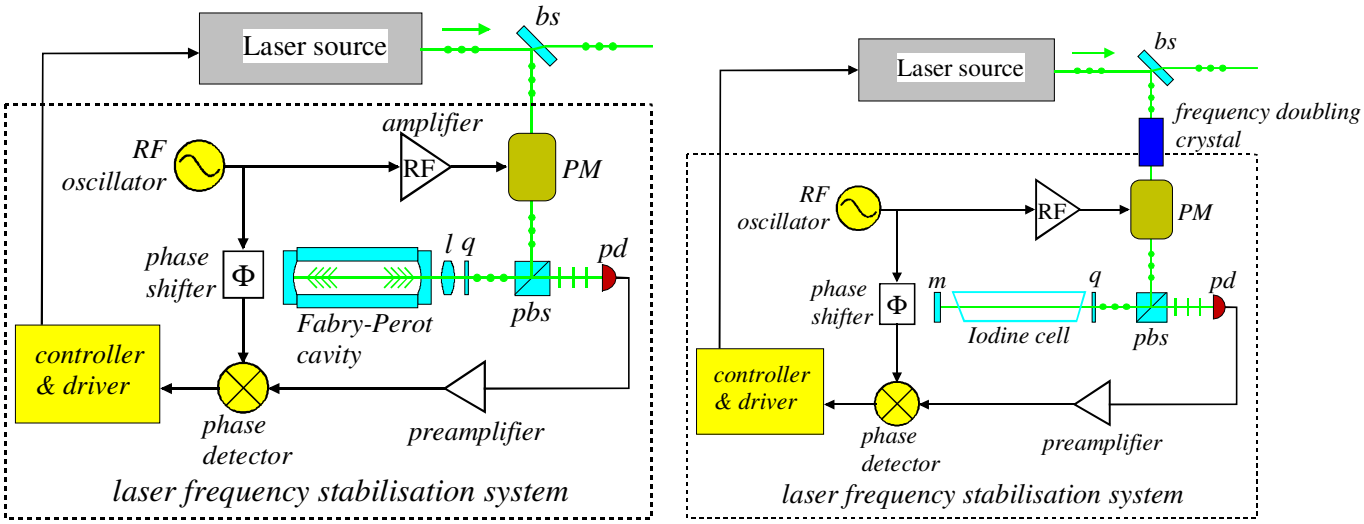

Figure 4.1-5: Schemes of the laser frequency stabilization using an optical cavity (left) and a molecular absorption line (right)

The best frequency stabilization performances achieved in laboratory with these techniques on a Nd:YAG laser (λ = 1064 nm; usual reference source for the high-performance interferometers) in the bandwidth of interest for a NGGM (1 ÷ 100 mHz) is $\delta\nu/\nu \cong 3.5 \cdot 10^{-14}/\sqrt{\text{Hz}}$ ($\delta\nu \cong 10$ Hz/$\sqrt{\text{Hz}}$) (Figure 4.1-6, [RD-22]). Therefore, the distance measurement noise limit (even for a negligible intrinsic noise of the interferometer) is $\delta L \cong 3.5 \cdot 10^{-14} \cdot L/\sqrt{\text{Hz}}$: ~0.35 nm/$\sqrt{\text{Hz}}$ at 10 km, ~3.5 nm/$\sqrt{\text{Hz}}$ at 100 km, and so on.

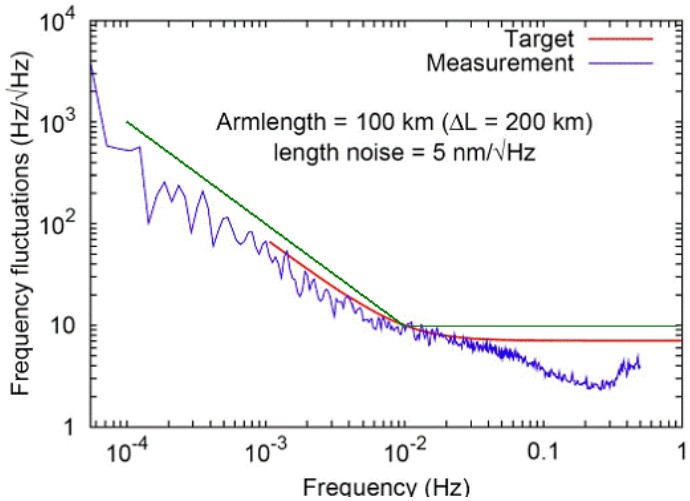

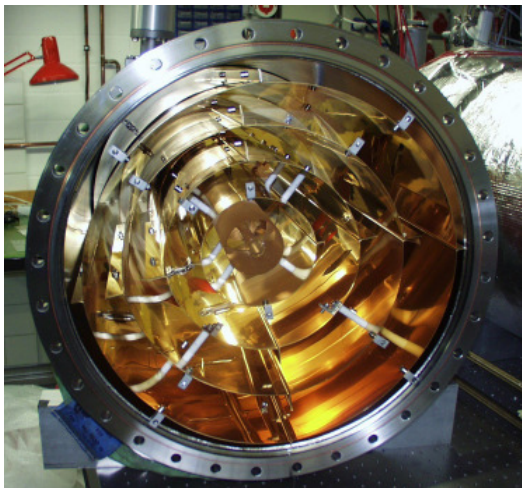

Figure 4.1-6 : Best frequency stability (left) achieved in laboratory using a reference optical cavity (right) [RD-22]

4.1.3 Angle metrology

As pointed out in section 3.3 and section 3.4, the knowledge of the orientation of the two satellites relative to the line joining the two satellites plays an important role in the ll-SST technique.
The angle metrology system developed by TAS-I in cooperation with INRIM [RD-4] is particularly suitable to work over long distances, in conjunction with the laser interferometer. In fact it measures the satellite orientation relative to the laser beam travelling between the two satellites, which over long distances, coincides in practice with the satellite-to-satellite line. A portion of the laser beam illuminating the satellite is picked up by a small telescope and focused on a Position Sensing Detectors, a four-electrode photodiode measuring the position and power of the light spot focused on its surface. The light spot position provides the direction of the incoming laser beam, and thus the satellite orientation relative to the beam.
By arranging three of such small telescopes (T_1, T_2, T_3) at the vertices of an equilateral triangle and measuring the optical power unbalance collected by the three detectors, it is possible to obtain the lateral displacement of the satellite w.r.t. the axis of the laser beam exploiting the property that the optical power has a theoretical Gaussian distribution in each cross section of the beam (see Figure 4.1-7). The tests performed on the breadboard of this angle (and lateral displacement) metrology system demonstrated an intrinsic measurement noise with spectral density $<10^{-6}$ rad/√Hz above 0.01 Hz (see Figure 4.1-8), the noise al lower frequencies being limited by the amplitude fluctuations of the utilized laser source.

In the GRACE follow-on EX-5 mission, the pointing offset of each satellite relatively to the incoming laser beam delivered by the other satellite is detected through the photodiodes of the laser interferometers placed on each satellite. These photodiodes have a four quadrant configuration that allows (by looking at the phase difference between the quadrants) to measure the angular-misalignment of the laser beam incident on the quadrant photodiode (Figure 4.1-3). Of course, this kind of angle metrology can be utilizes only in combination with a distance metrology based on a transceiver scheme, in which there is a laser and an interferometer

operative on each satellite. No lateral displacement metrology has been defined for the EX-5 mission, as far as it is known from the available literature.

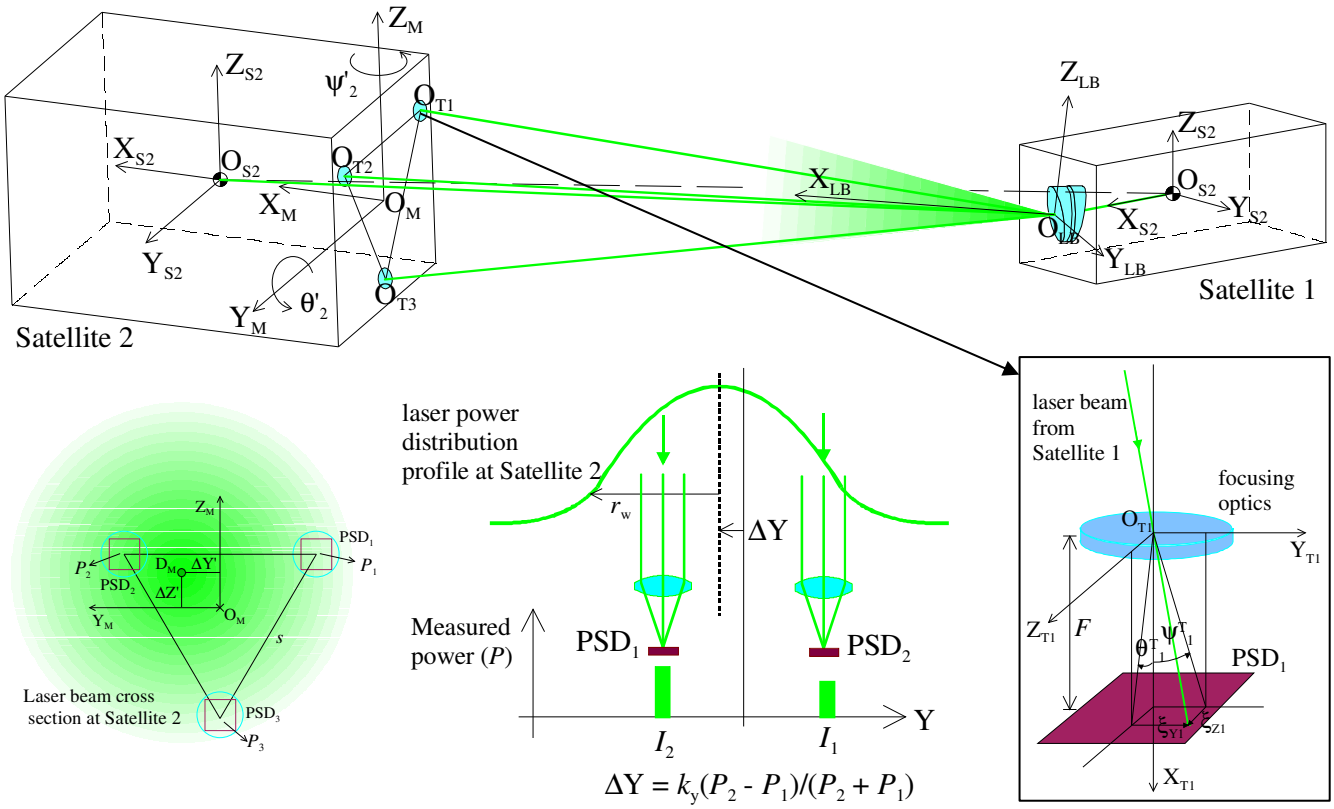

Figure 4.1-7 : Measurement principle of the satellite orientation and lateral displacements relative to the laser beam.

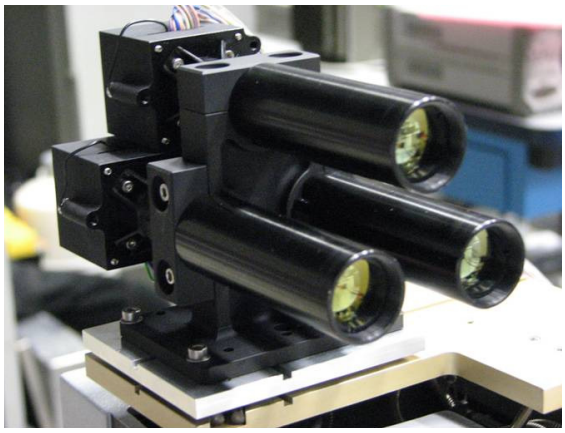

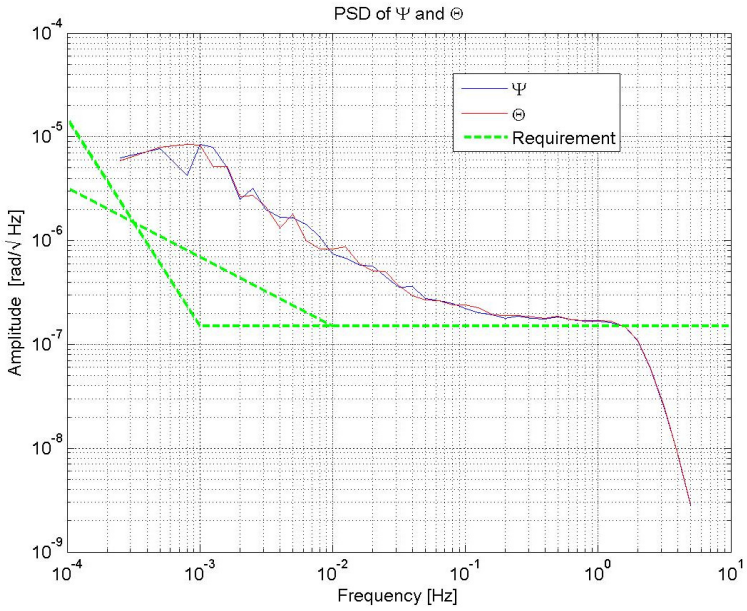

Figure 4.1-8: Breadboard and measured performance of the angle/lateral displacement metrology developed by TAS-I in preparation of a NGGM.

4.2 Accelerometers Technologies Review

The survey of the state-of-the-art accelerometers for in-space applications and of the related technologies is provided in a separate technical note [RD-23]. A (partial) summary of this survey is provided in Table 4.2-1.
In conclusion, the accelerometer (GRADIO) developed and implemented by ONERA for the GOCE mission (Figure 4.2-1) appears adequate without substantial modifications to fulfil the needs of the NGGM.

Table 4.2-1: Comparison between three accelerometers developed by ONERA for GRACE (SuperSTAR), GOCE (GRADIO) and for future interplanetary missions (MicroSTAR).

	SuperSTAR (GRACE)	GRADIO (GOCE)	MicroSTAR
Mass	11.4 kg (w/o EEU)	5.2 kg (ASH) 6.3 kg (FEEU for 2 ASH) 6.6 kg (GAIEU for 6 ASH)	3 kg (incl. Bias Rej Syst)
Consumption	2 W (only FEE)	15 W (FEEU for 2 ASH) 16.5 W (GAIEU for 6 ASH)	3 W
Size	13.7 litres (w/o EEU)	165x165x187 mm (ASH) 250x250x133 mm (FEEU for 2 ASH) 353x250x104 mm (GAIEU for 6 ASH)	3 litres
Noise	10^{-10} m/s²/Hz$^{1/2}$	2 10^{-12} m/s²/Hz$^{1/2}$	10^{-10} m/s²/Hz$^{1/2}$
MBW	10^{-4} – 0.1 Hz	5 10^{3} – 0.1 Hz	10^{-3} – 0.1 Hz
Range	5 10^{-5} m/s²	6 10^{-6} m/s²	2 10^{-5} m/s²

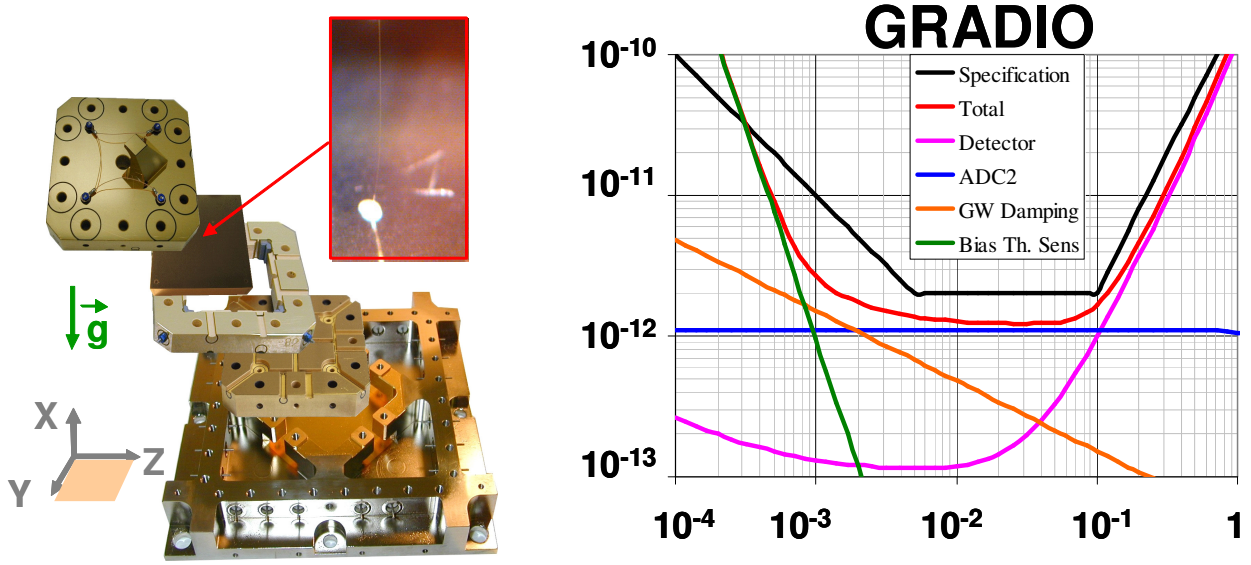

Figure 4.2-1: Mechanical core of the GRADIO accelerometer (left) and predicted measurement noise with the main contributors (right).

5. INSTRUMENT CONCEPTS DEFINITON AND TRADE-OFF

5.1 Concepts for the Satellite-to-Satellite Laser Metrology

As anticipated in section 4.1.1 the laser interferometer measuring the distance variation between to distant satellites can be implemented according to two different schemes:

1. scheme based on the passive retro-reflection of the laser beam emitted from Satellite 1 towards Satellite 2, back to Satellite 1;
2. scheme based on the optical transponder in which the optical power of the laser beam received by Satellite 2 is amplified using a second laser on Satellite 2 before being sent back to Satellite 1.

The two concepts have been studied and developed up to breadboard level respectively by TAS-I/INRIM ([RD-3], [RD-4]) and JILA/JPL [RD-16]. The laboratory tests results (presented in section 4.1.1) show that the two breadboards have similar measurement performances. The difference consists in the operative distance, which is potentially much longer for the JILA/JPL interferometer. However, the performance model and the optical link budget shows that the TAS-I/INRIM interferometer can achieve the (preliminarily) established performance with merely 1 pW on the photodiode pd_2 and, using a laser source emitting 500 mW, this minimum power is ensured up to the considerable distance of ~100 km ([RD-4] and section 5.3.1 of this document). Therefore, the passive retro-reflection solution has been preferred by TAS-I/INRM to the optical transponder scheme, because the latter one is more complex and less robust/reliable being two laser sources simultaneously operating (and phase locked) required for performing the distance measurement.

The selection of the retro-reflector scheme implies also the selection of the angle/later displacement metrology concept studied and developed by TAS-I/INRIM [RD-4] (see section 4.1.3), because the alternative option envisaged for the GRACE follow-on EX-5 mission is applicable only to the optical transponder scheme.

As far as the frequency stabilizations is concerned, the technique based on the reference optical cavity (see section 4.1.2) is currently preferred because it can potentially provide the required performance (see Figure 4.1-6) and can be implemented in a simpler and more robust way than the technique based on the molecular absorption line.

The precise pointing of the laser beam emitted from Satellite 1 towards Satellite 2 is a critical issue for the implementation of the laser based ll-SST technique. In the previous preparatory studies for the NGGM ([RD-4], [RD-5]) it was proposed to use a dedicated mechanism (called Beam Steering Mechanism) consisting of two wedge prisms integrated in two rotation stages which are mounted back-to-back (see Figure 5.1-1). The BSM was sized to change the orientation of the laser beam outgoing from Satellite 1 in a cone with semi-aperture angle = 3° and supported the functions of the optical link acquisition between the two satellites and of the precision pointing maintenance of the laser beam during the measurement phase. Its utilization has the advantage of decoupling the function of the satellite attitude control from that of the

laser beam pointing, i.e. a fine pointing of Satellite 1 towards the Satellite 2 in not necessary with the BSM.
The implementation and testing of a breadboard of the BSM made by TAS-I [RD-24] demonstrated the technical feasibility of the concept and its capability of achieving the specified performance.

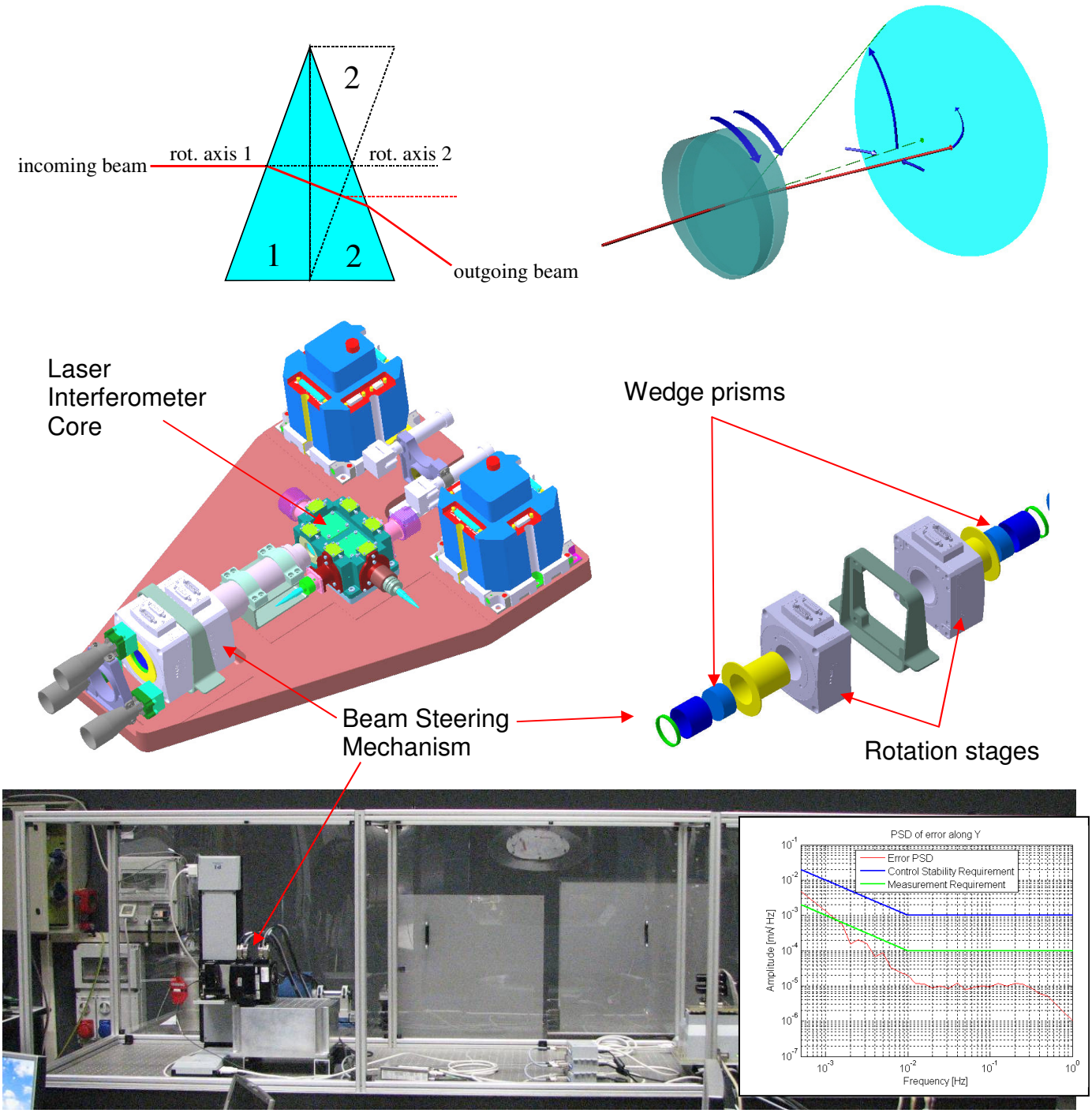

Figure 5.1-1: Working principle of the BSM (top). Arrangement of the BSM on the metrology optical bench as defined in the previous NGGM studies (middle). Breadboard of the BSM mounted on the test bench and test result (bottom).

On the other hand, the presence of a continuously operating mechanism on a long-duration mission represents certainly a weak point (lower reliability), besides being another source distance measurement error and a potential source of disturbance for the accelerometer measurements (although in [RD-5] the disturbances on the platform due to BSM operation were assessed compatible with the accelerometer operation). In fact, while the two wedge prisms of the BSM rotate, the laser beam crosses different glass thicknesses and the optical path measured by the laser interferometer consequently changes. This optical path variation induced by the BSM operation and not by the variation of the inter-satellite distance is large (up to 34.5 μm) and must be estimated (through a model and the measurements of the rotation stage encoders) and subtracted from the interferometer measurement. Since the estimation of this effect is not perfect, another error term (called “laser beam bending errors” in [RD-5]) has to be added in the tree shown in Figure 3.3-3. This error is present even if the BSM is realized in other ways (for example using a pair of steerable mirrors in place of the wedge prisms) because the presence of moving elements along the path of the laser beam and the unavoidable manufacturing imperfections in the realization of the BSM produce always an apparent variation of the measured distance.

The alternative to the BSM is of course to point the laser beam through the attitude of the whole satellite. The viability of this solution depends on the laser beam pointing requirements and on the availability of fine attitude control actuators. In the previous preparatory studies for the NGGM ([RD-4], [RD-5]), the performance requirements were derived for an inter-satellite distance of 10 km. The allocation to the laser beam pointing stability was consequently stringent (10^{-7} rad/√Hz) and very challenging for the attitude control. In the new scenario, with all the requirements rescaled for a distance of 100 km, the task for the attitude control becomes easier. Moreover, by removing the BSM, the “laser beam bending errors” can be re-allocated and the used for relaxing furthermore the laser beam pointing. The possibility of using high-resolution, wide bandwidth and low not thrusters, like the mini-Radiofrequency Ion Thrusters [RD-25], increases the chances of managing the laser beam pointing by means of the satellite attitude control only. In a scenario without the BSM, the laser beam remains always nominally aligned to the X-axis of the Satellite 1 (it is not oriented by the BSM independently from the Satellite 1 attitude). It is therefore possible determine the Satellite 1 orientation relative to the satellite-to-satellite line from the measurement of the lateral displacement of the Satellite 2 relative to laser beam axis (measured by the lateral displacement metrology on Satellite 2) and from the knowledge of the distance between the satellites (measured by the differential GNSS), as shown in Figure 5.1-2.

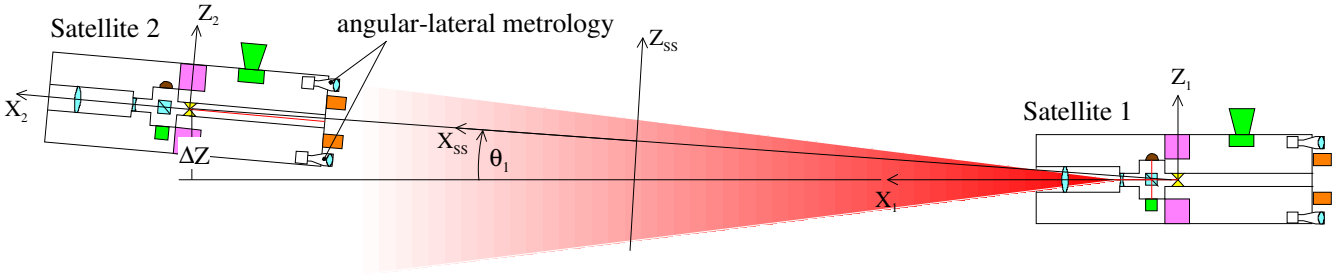

Figure 5.1-2: Measurement principle of the Satellite 1 orientation (θ_1, ϕ_1) relative to the satellite-to-satellite line from the lateral displacement (Δ_Z, Δ_Y) of the Satellite 2 relative to laser beam axis.

5.2 Concepts for the Acceleration Measurement

In the previous preparatory studies for the NGGM ([RD-4], [RD-5]) a concept making use of two GOCE-like accelerometers (i.e. the GRADIO model developed by ONERA) on each satellite were devised. The accelerometers were arranged on the same optical bench of the laser interferometer, symmetrically w.r.t. the COM, and aligned along the Y-axis of the satellite (which, in a GRACE-like in-line formation, is nominally pointed along the direction orthogonal to the orbit plane). The advantages of this accelerometer arrangement (shown in Figure 5.2-1) are:

- the satellite COM is free for the accommodation of the retro-reflector for the laser interferometer;
- two accelerometers provide a single-failure tolerance in the measurement of the non-gravitational acceleration (although with degraded performance);
- two satellite angular accelerations (around the X and Z axes, $\dot{\omega}_X$, $\dot{\omega}_Z$) can be obtained from the difference of the linear accelerations measured by the accelerometers;
- the accelerometer pair forms a one-axis gradiometer enabling to measure also one component of the Earth gravity gradient tensor (the cross-track component, V_{YY}, in an in-line formation).

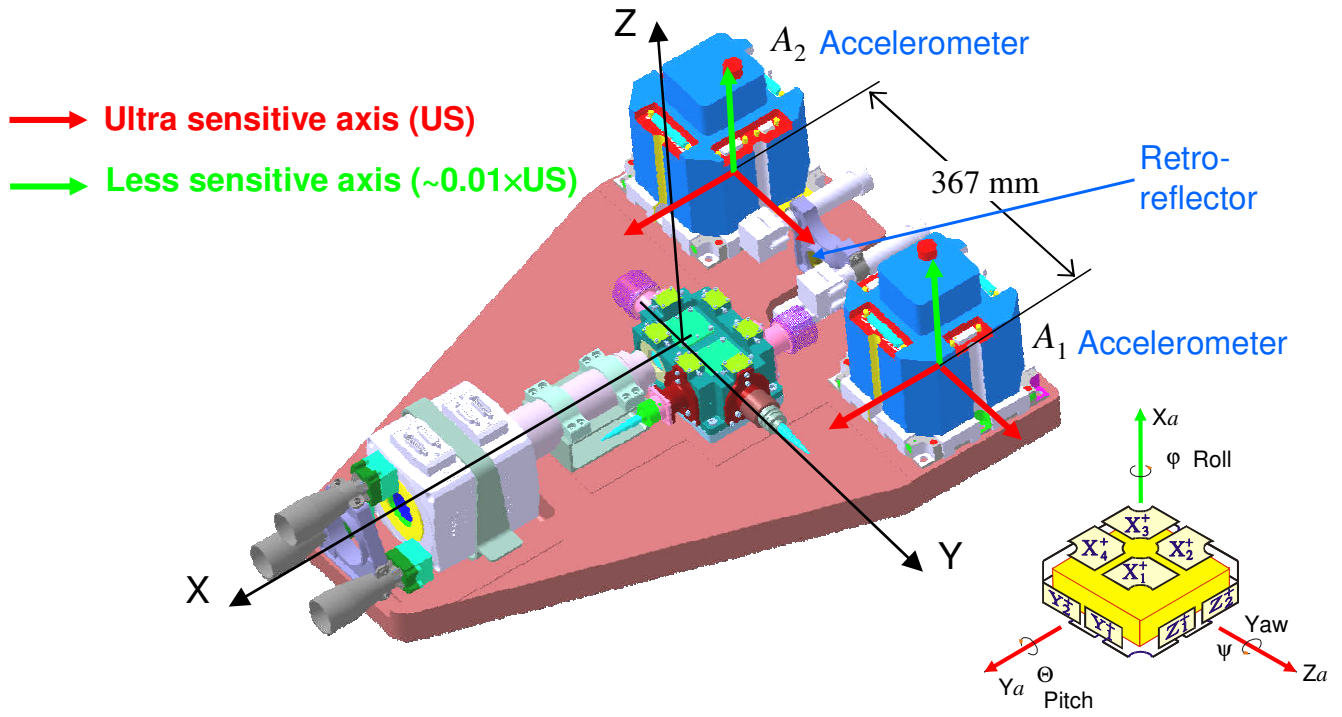

Figure 5.2-1 : Arrangement of two GOCE-like accelerometers as defined in the previous NGGM studies. Arrangement of proof mass control electrodes and of ultra-sensitive, less-sensitive axes.

This arrangement however has the drawback that $\dot{\omega}_X$ is measured with less sensitive axes only (hence with poorer precision) and the angular acceleration around Y ($\dot{\omega}_Y$, important for the laser

beam pointing as well as $\dot{\omega}_Z$) cannot be measured by difference of linear accelerations. Indeed, each accelerometer can measure the angular acceleration of the proof mass about its three sensitive axes (by difference of the linear accelerations measured by the control electrodes) but, in this particular arrangement, $\dot{\omega}_Y$ is measured by electrodes of the less sensitive axis (hence again with poorer precision).

In order to measure $\dot{\omega}_Y$ and $\dot{\omega}_Z$ with the same (good) precision (see preliminary requirement on angular acceleration on paragraph 3.4), while keeping one ultra-sensitive axis oriented in along X (main direction for the measurement of the linear acceleration), the two accelerometers shall be mounted rotated through 90° around the satellite X axis so that the proof masses are arranged as in **Figure 5.2-2**. So doing, $\dot{\omega}_X$, $\dot{\omega}_Z$ are obtained from the difference of the linear accelerations measured by the accelerometers along ultra-sensitive axes, while $\dot{\omega}_Y$ is measured at the level of the proof mass by electrodes of the ultra sensitive axes. The drawback of this arrangement is that the component V_{YY} of the GGT is measured by less sensitive axes only (hence it is practically useless).

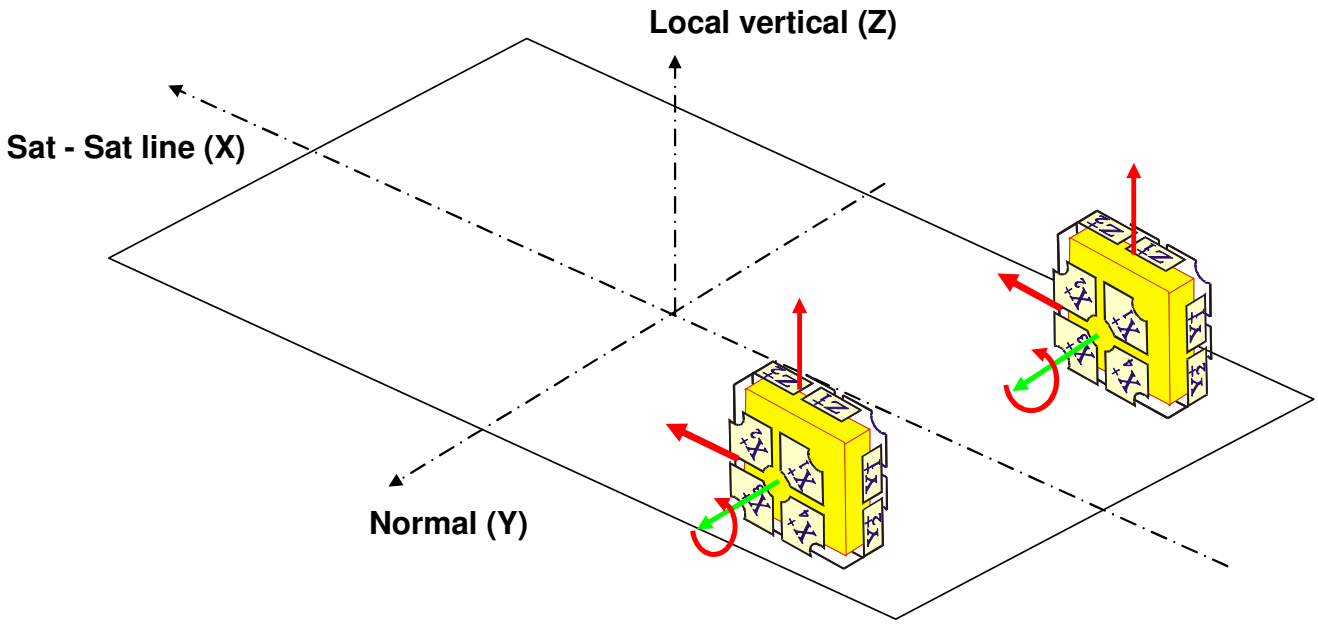

Figure 5.2-2 : Alternative arrangement of two accelerometers.

In order to measure $\dot{\omega}_Y$ and $\dot{\omega}_Z$ with the same (good) precision, and still maintaining the possibility of measuring one component of the GGT with good precision too, a set of four accelerometers is needed (with just three accelerometers, the measurement precision of $\dot{\omega}_Y$ and $\dot{\omega}_Z$ wouldn't be the same). Three different arrangements of four accelerometers providing these measurements have been identified and are shown in Figure 5.2-3, Figure 5.2-4,and Figure 5.2-5 (here the optical bench is shown in the configuration without the Beam Steering Mechanism). Indeed, another four-accelerometer layout exists (Figure 5.2-6) but it doesn't provide the measurement of GGT components with ultra-sensitive axes.

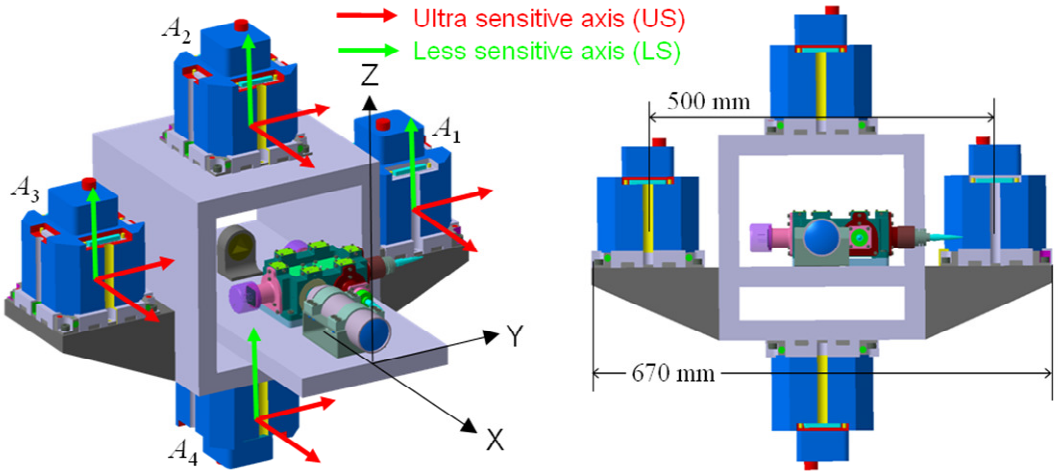

Linear acceleration X: $a_X = (a_{1X} + a_{2X} + a_{3X} + a_{4X})/4$ (US axes only)
Linear acceleration Y: $a_Y = (a_{1Y} + a_{2Y} + a_{3Y} + a_{4Y})/4$ (US axes only)
Linear acceleration Z: $a_Z = (a_{1Z} + a_{2Z} + a_{3Z} + a_{4Z})/4$ (LS axes only)
Angular acceleration X: $d\omega_X/dt = [(a_{1Z} - a_{3Z})/L - (a_{2Y} - a_{4Y})/L]/2$ (US + LS axes)
Angular acceleration Y: $d\omega_Y/dt = (a_{2X} - a_{4X})/L + V_{XZ} - \omega_X\omega_Z$ (US axes only)
Angular acceleration Z: $d\omega_Z/dt = (a_{3X} - a_{1X})/L - V_{XY} + \omega_X\omega_Y$ (US axes only)
GGT components: $V_{YY} = (a_{3Y} - a_{1Y})/L - \omega_X^2 - \omega_Z^2$

Figure 5.2-3 : Arrangement of four accelerometers: option 1.

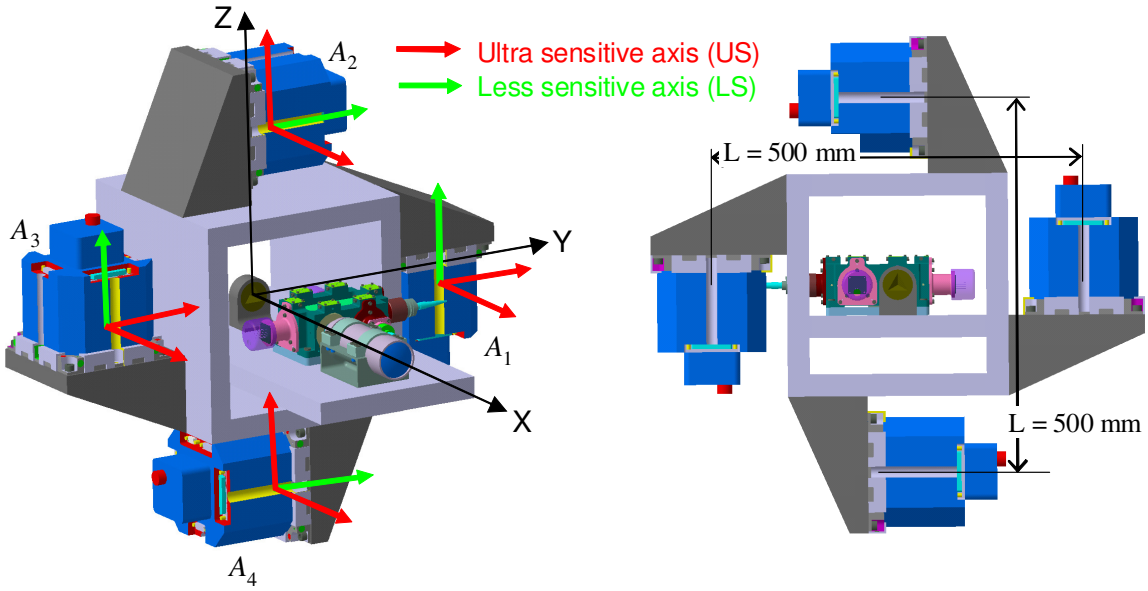

Linear acceleration X: $a_X = (a_{1X} + a_{2X} + a_{3X} + a_{4X})/4$ (US axes only)
Linear acceleration Y, Z: $a_Y = (a_{1Y} + a_{3Y})/2$, $a_Z = (a_{2Z} + a_{4Z})/2$ (US axes only)
Angular acceleration X: $d\omega_X/dt = [(a_{1Z} - a_{3Z})/L - (a_{2Y} - a_{4Y})/L]/2$ (LS axes only)
Angular acceleration Y: $d\omega_Y/dt = (a_{2X} - a_{4X})/L + V_{XZ} - \omega_X\omega_Z$ (US axes only)
Angular acceleration Z: $d\omega_Z/dt = (a_{3X} - a_{1X})/L - V_{XY} + \omega_X\omega_Y$ (US axes only)
GGT components: $V_{YY} = (a_{3Y} - a_{1Y})/L - \omega_X^2 - \omega_Z^2$, $V_{ZZ} = (a_{4Z} - a_{2Z})/L - \omega_X^2 - \omega_Y^2$

Figure 5.2-4 : Arrangement of four accelerometers: option 2.

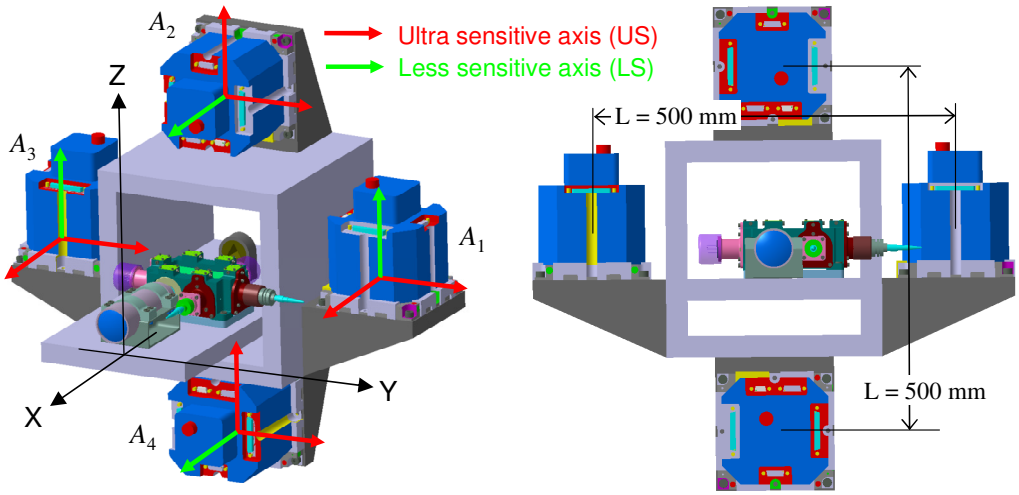

Linear acceleration X, Z: $a_X = (a_{1X} + a_{3X})/2$, $a_Z = (a_{2Z} + a_{4Z})/2$ (US axes only)
Linear acceleration Y, Z: $a_Y = (a_{1Y} + a_{2Y} + a_{3Y} + a_{4Y})/4$ (US axes only)
Angular acceleration X: $d\omega_X/dt = [(a_{1Z} - a_{3Z})/L - (a_{2Y} - a_{4Y})/L]/2$ (US + LS axes)
Angular acceleration Y: $d\omega_Y/dt = (a_{2X} - a_{4X})/L + V_{XZ} - \omega_X\omega_Z$ (LS axes only)
Angular acceleration Z: $d\omega_Z/dt = (a_{3X} - a_{1X})/L - V_{XY} + \omega_X\omega_Y$ (US axes only)
GGT components: $V_{YY} = (a_{3Y} - a_{1Y})/L - \omega_X^2 - \omega_Z^2$, $V_{ZZ} = (a_{4Z} - a_{2Z})/L - \omega_X^2 - \omega_Y^2$

Figure 5.2-5 : Arrangement of four accelerometers: option 3.

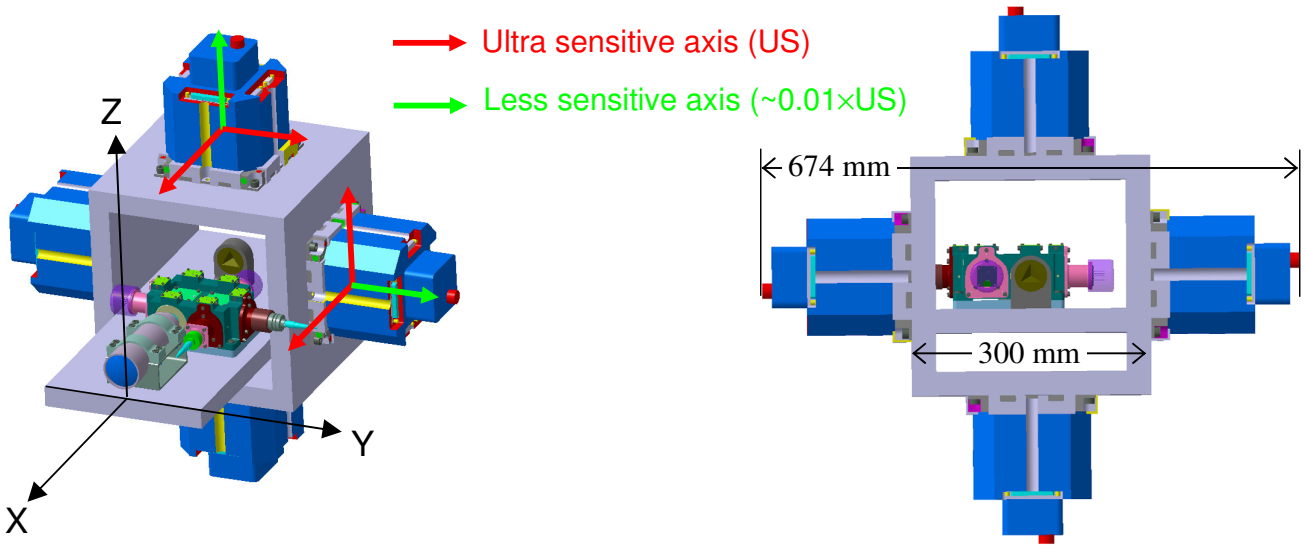

Figure 5.2-6 : Arrangement of four accelerometers: option 4.

Among the first tree options, option 1 doesn't provide a measurement of the linear acceleration along each direction with US axes (the linear acceleration Z is measured with LS axes only).
In option 2 two angular accelerations ($\dot{\omega}_Y$, $\dot{\omega}_Z$) are measured with US axes.
In option 3 only $\dot{\omega}_Z$ is measured with US axes. Moreover the linear acceleration X is measured with only two US axes instead than four (like in option 1 and 2).

5.3 Recommended Reference Payload of the NGGM

5.3.1 Satellite-to-Satellite Laser Metrology

Among the metrology concepts described in paragraph 5.1, we confirm the recommendation of the laser interferometer based on the retro-reflector complemented with the angle/lateral displacement metrology making use of three telescopes with Position Sensing Detectors accommodated on Satellite 2. The reasons are:

- The concept is simple and robust.
- It provides the required performance up to 100 km still using a relatively small laser source emitting 500 mW of optical power and a small receiving optics (40 mm diameter telescope for the interferometer, 10 mm diameter telescope for the angle/lateral metrology).

Concerning the laser beam pointing, after having assessed that the new requirements (section 6.5) are within the reach of the attitude control system [RD-13], it is recommended to remove the Beam Steering Mechanism in favour of a simpler, less risky system having a smaller impact on the performance of the laser interferometer and (potentially) of the accelerometers.

The functional scheme of this metrology system is shown in Figure 5.3-1. The detailed block diagrams of the laser interferometer, of the angle/lateral displacement metrology and of the laser frequency stabilization system and of their electronics remains unchanged with respect to those already provided in [RD-4].

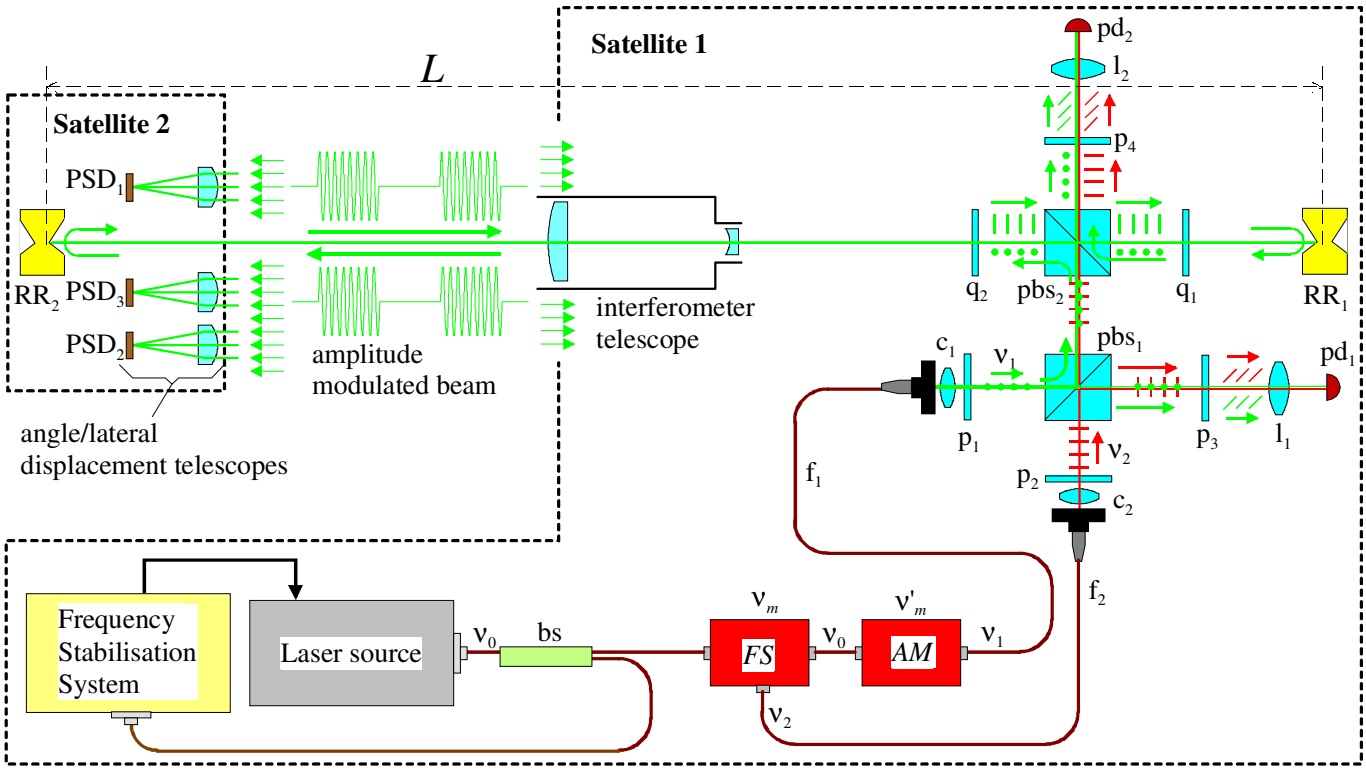

Figure 5.3-1 : Functional scheme of the metrology system proposed for the NGGM.

The configuration of the optical bench where the laser interferometer is accommodated is shown in Figure 5.3-2. With respect to the configuration defined in the previous preparatory studies for the NGGM [RD-4], the optical bench now includes only the interferometer core, the interferometer telescope and the retro-reflectors (two hollow corner cubes mounted back to back with the vertices coincident). Apart from the BSM, also the angle/lateral displacement metrology has been removed from the bench. The three small telescopes of the angle/lateral metrology have been moved on the back side of each satellite (i.e. the side of the Satellite 2 which is illuminated by the laser beam emitted by the Satellite 1) for increasing the baseline between the 3 telescopes and to reduce the diameter of the baffle feedthrough through which the laser beam reaches the optical bench. The accelerometers are also not installed on the bench since in the preferred configuration option (see section 5.3.2 and Figure 5.2-4) they (four) are arranged on a square frame surrounding the optical bench in correspondence of the retro-reflector (i.e. the nominal position of the satellite COM).

Again the same bench is duplicated on both satellites so that, if a failure occurs on Satellite 1 that prevents the interferometer operation, the scientific mission can continue after having exchanged the position of the two satellites (i.e. the Satellite 2 becomes the active satellite).

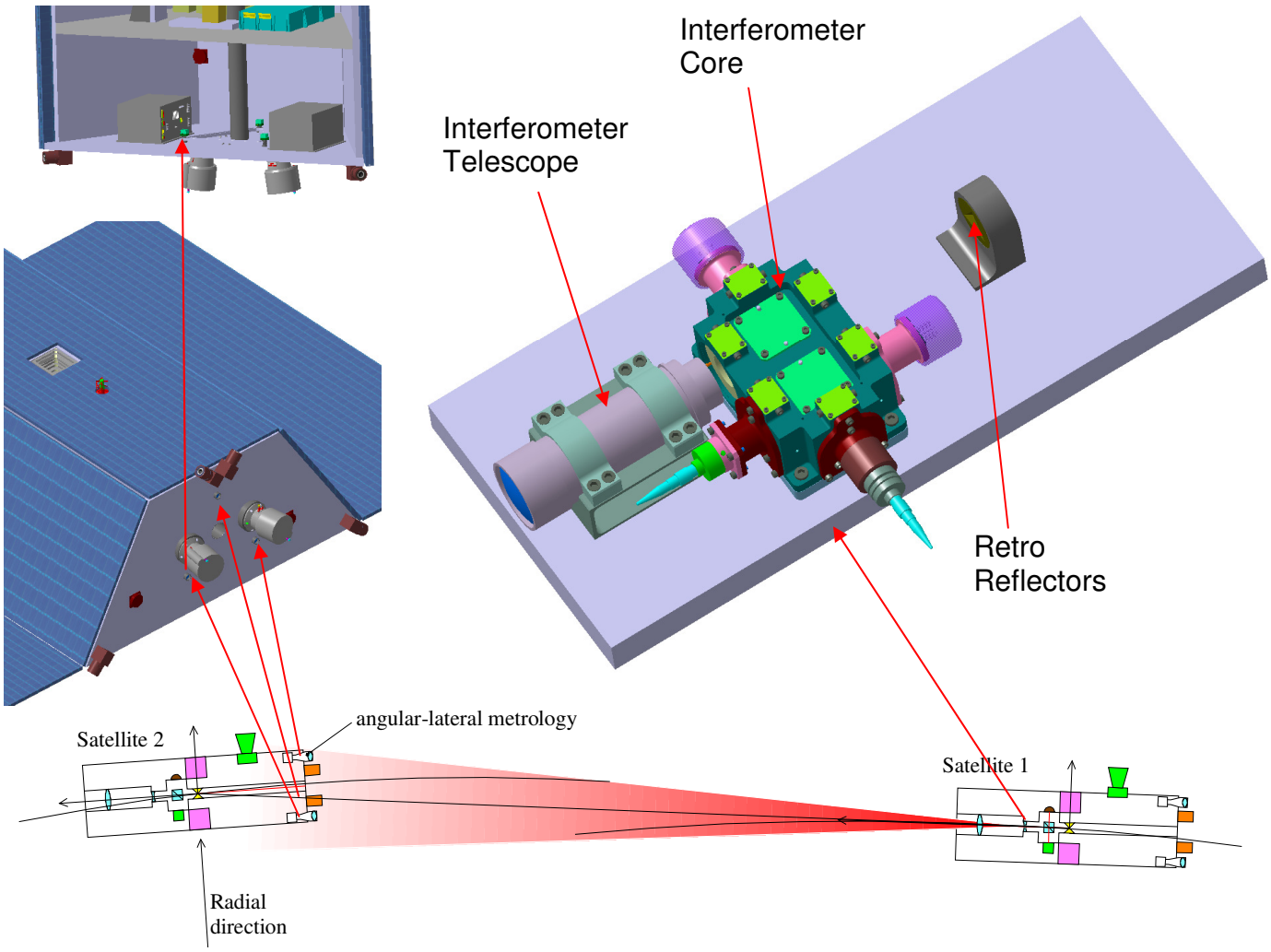

Figure 5.3-2 : Optical bench configuration.

The preliminary mass and power consumption budget of the reference satellite-to-satellite laser metrology system is provided in Table 5.3-1. The mass and power of the electronics has been estimated by similarity with items performing similar functions. The laser source mass derives from the item under development for LISA. The mass of the Frequency Shifter and Amplitude modulator is that of the COTS devices which have been used in the metrology system breadboard [RD-4].
A 25% conservative contingency margin has been added to the mass and power total figures to account for the design maturity status.

Table 5.3-1: Mass and power consumption budget for the satellite-to-satellite laser metrology.

Item	Mass [kg]	Power [W]
Interferometer core	2.7	
Interferometer telescope	0.88	
Laser retro-reflector	0.12	
Optical bench & accelerometers support structure	12.6	
Angle metrology optical heads assembly	2.5	
Metrology Electronic Unit	4	30
Laser source (*)	6	
Laser frequency stabilization system	4	
Laser Control and Driving Unit	10	17
Frequency Shifter and Amplitude Modulator	0.5	
FS, AM Driving Unit	4	20
Total	**47.3**	**67**
Margin (25%)	**11.8**	**16.8**
Total with margin	**59.1**	**83.8**

(*) power consumption included in the Laser Control and Driving Unit

The optical power budget for the measurement laser beam, travelling between the two satellites, is provided in Table 5.3-2. It has been computed for satellite-satellite distances d = 75 and d = 100 km, considering retro-reflectors on both satellites (RR_1, RR_2) with a useful area of 2.1 cm^2.

The power losses due to the various optical elements crossed by the laser beam along its path have been computed from the absorption coefficient of the glasses, from the reflectivity of the anti-reflection coatings (0.25%), and from the transmission efficiency declared by the manufacturer for the polarizer beam-splitters and linear polarisers. For the coupling efficiency of the Frequency Shifter and the Amplitude Modulator, the figures estimated by the manufactures for the integrated device (implementing the FS and AM functions) have been considered:

- -2.5 dB attenuation for the reference beam, frequency shifted at $\nu_2 = \nu_0$+110 MHz,
- -3 dB attenuation for the measurement beam, frequency shifted at $\nu_1 = \nu_0$+80 MHz and amplitude modulated

The optical power producing the beat signal on the photodiode pd_2 of the laser interferometer is computed considering for the collecting telescope a clear aperture of 40 mm. The optical power focused on each PSD of the angle/lateral metrology on Satellite 2 (S2) has been computed considering for each of the three collecting telescopes a clear aperture of 10 mm.
The amount of optical power received by these detectors is compared with minimum value required to fulfil the performance requirements of the metrology systems: see plots on Figure 5.3-3 and Figure 5.3-4, computed from the performance models provided in [RD-4].

The optical power outgoing from the laser source has been adjusted so to illuminate to photodiode pd_2 with ten times the minimum power fulfilling the requirement (10 pW) when the inter-satellite distance is 100 km. The optical link budget shows that an output power of 0.5 W from the laser source is sufficient to fulfil the minimum power requirements on all the detectors, of the heterodyne interferometer and of the angle/lateral displacement metrology up to a distance of100 km (see Table 5.3-2 and Figure 5.3-5, Figure 5.3-6).

However there are still design margins that can be exploited to increase the operational distance between the satellites, if necessary or, alternatively, to decrease the optical power of the laser source. These design margins are:

- The size of the aperture of the angle metrology telescopes on S2 that can be further increased (at present the diameter is 10 mm)
- A longer focal length of the angle metrology telescopes allows increasing the sensitivity to the angular displacements (but at the expenses of a FOV reduction)
- The cross section of the retro-reflector on S2 (now with a useful area of 2.1 cm^2) that can be further increased so increasing the amount of power reflected back to S1.

Table 5.3-2: Optical link budget for 75 km and 100 km inter-satellite distance.

Measurement beam	Power [W] (d = 75 km)	Power [W] (d = 100 km)	Minimum Requirement [W]	Power/Req. ratio for 75 (100) km
Emitted by the laser source	**0.500**	**0.500**		
Output from the optical fibre f_1	**0.223**	**0.223**		
Received by CCR2 (equivalent dia. 16.5 mm)	**4.5E-07**	**2.5E-07**		
Received back by telescope on S1 (dia. 40mm)	**4.3E-11**	**1.3E-11**		
Before the linear polarizer p_4	**3.9E-11**	**1.2E-11**		
Received by detector pd_2 (beat signal power)	**3.2E-11**	**1.0E-11**	**1.00E-12**	**32 (10)**
Received by each PSD detectors on S2 ($PSD_{1,2,3}$) (dia. 10mm)	**1.6E-07**	**9.0E-08**	**7.00E-08**	**2.3 (1.3)**

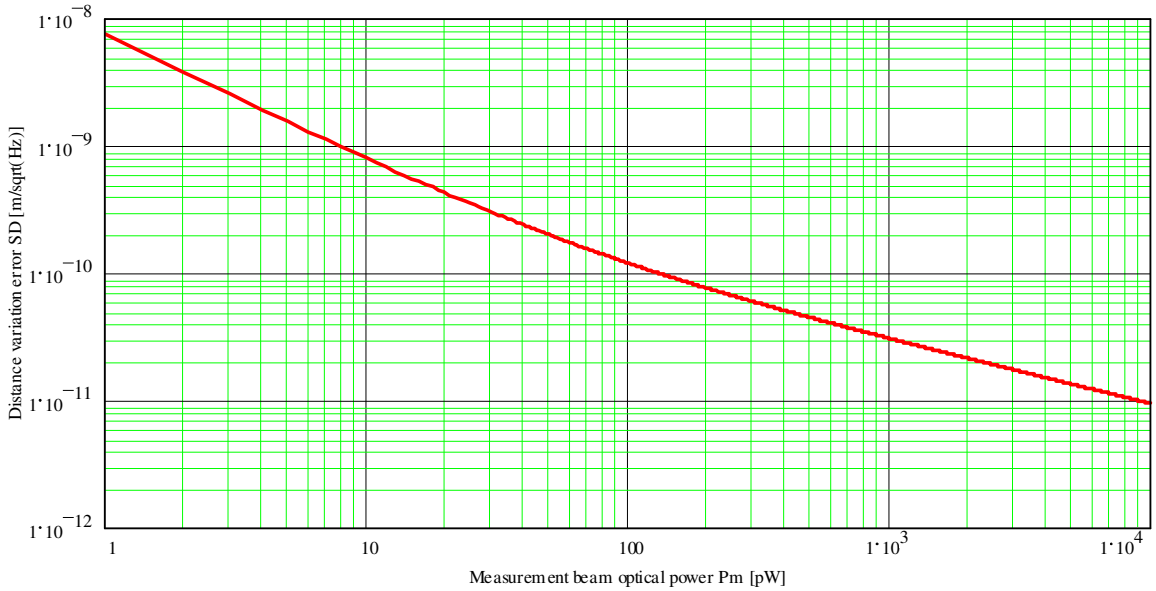

Figure 5.3-3: Distance variation measurement error spectral density $\tilde{N}_L$ versus optical power P_m. For each value of the optical power the error spectral density is approximately white.

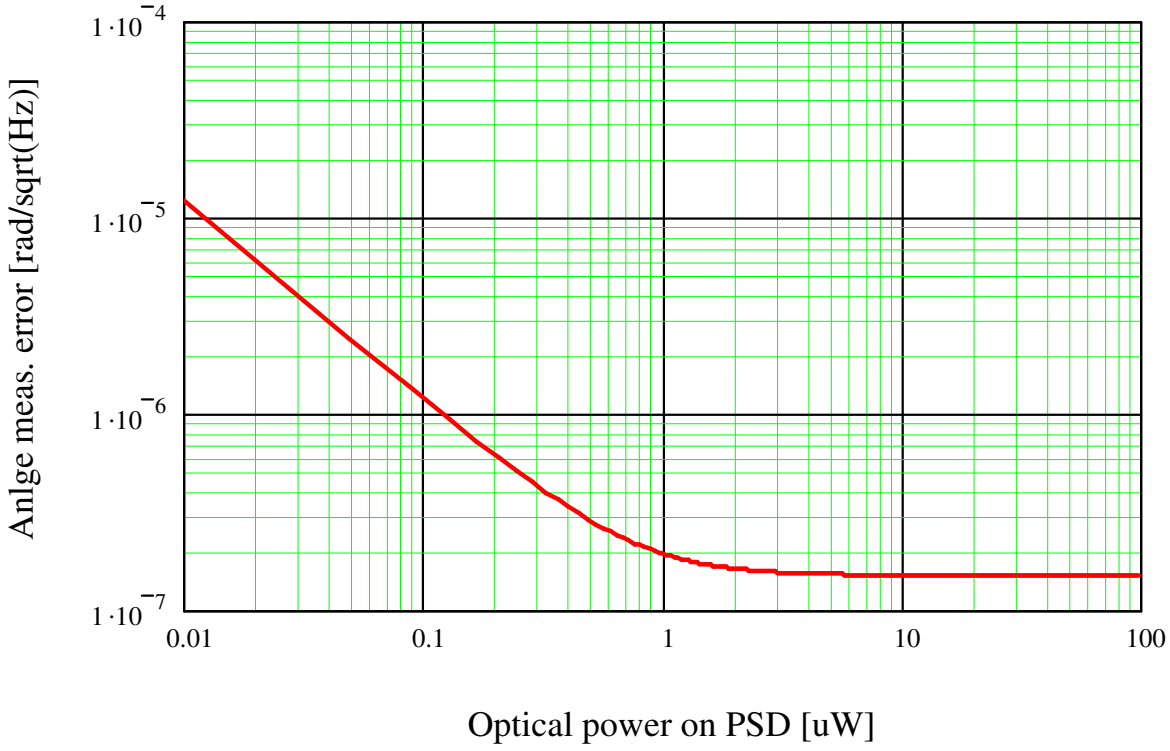

Figure 5.3-4: Angle measurement error spectral density versus optical power focused on the PSD.

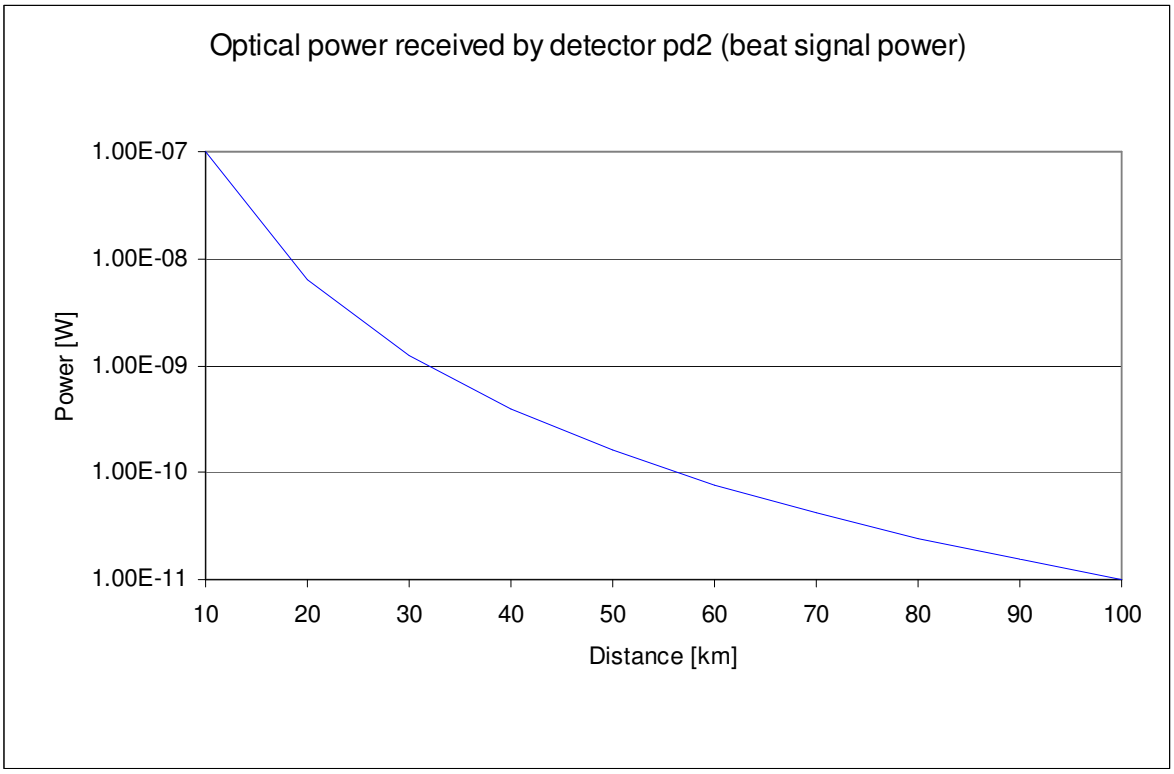

Figure 5.3-5: Optical power received by the photodiode of the distance variation metrology on S1 vs. inter-satellite distance

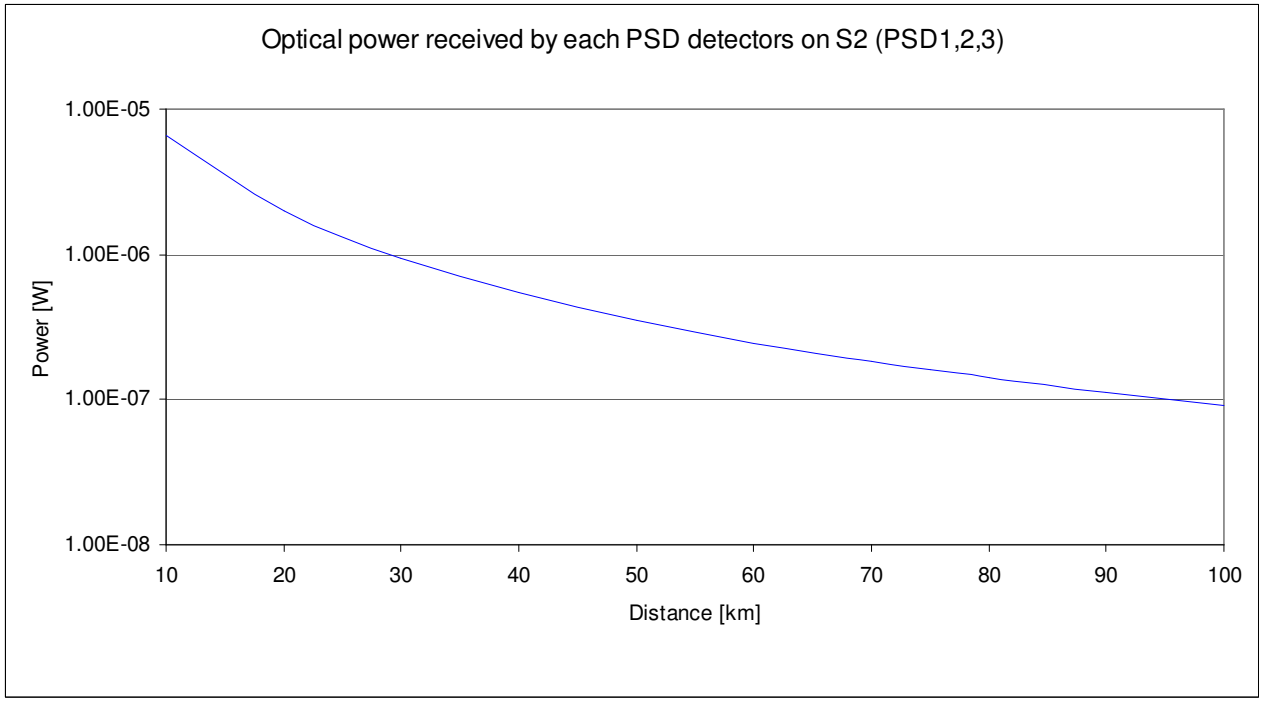

Figure 5.3-6: Optical power received by each PSD of the angle/lateral displacement metrology on S2 vs. inter-satellite distance

5.3.2 Acceleration Measurement System

Among the various accelerometer arrangements described in paragraph 5.2, the option 2 (Figure 5.2-4) based on four accelerometers is currently recommended for the following reasons:

- The linear accelerations a_X, a_Y, a_Z are all measured with US axes.
- There are four US axes in the X direction (nominally aligned to the satellite-to-satellite line). There is therefore more precision and more redundancy in the measurement of a_X.
- The angular accelerations $\dot{\omega}_Y$, $\dot{\omega}_Z$ (important for the laser beam pointing) can be obtained by difference of linear accelerations measured by the pairs (A_2, A_4), (A_1, A_3) along US axes, or from angular accelerations of the proof masses of the same pairs, again measured by sensitive axes electrodes.
- The cross-track and radial components of the GGT (V_{YY}, V_{ZZ}) are obtained by difference of linear accelerations measured with US axes. Although the GGT is not the primary scientific observable (like in GOCE) for the reconstruction of the Earth gravity field, the availability of one or two GGT components, in addition to the satellite-to-satellite distance variation, can be helpful for the computation of the gravity field solution.

Assuming for each accelerometer the same performance as predicted for GOCE[1] (Figure 5.3-7) and considering a baseline length L = 0.5 m between the accelerometers, the quantities:

- $a_X = (a_{1X} + a_{2X} + a_{3X} + a_{4X})/4$
- $a_Y = (a_{1Y} + a_{3Y})/2$
- $a_Z = (a_{2Z} + a_{4Z})/2$
- $\dot{\omega}_X = [(a_{1Z} - a_{3Z})/L - (a_{2Y} - a_{4Y})/L]/2$
- $\dot{\omega}_Y \cong (a_{2X} - a_{4X})/L$
- $\dot{\omega}_Z \cong (a_{3X} - a_{1X})/L$
- $V_{YY} \cong (a_{3Y} - a_{1Y})/L$
- $V_{ZZ} \cong (a_{4Z} - a_{2Z})/L$

are measured by the option 2 accelerometer system with the error spectral densities shown in Figure 5.3-8. Note however that the above expressions of $\dot{\omega}_Y$, $\dot{\omega}_Z$, V_{YY}, V_{ZZ} are only approximations. In fact, they include also centrifugal acceleration terms and off-diagonal GGT components (see Figure 5.2-4 for the complete expressions), that cannot be removed due to the lack of accelerometer along the X axis. The presence of these extra terms contribute to the measurement error of $\dot{\omega}_Y$, $\dot{\omega}_Z$, V_{YY}, V_{ZZ}.

[1] Only the low-frequency noise slope has been modified (reduced from $1/f^3$ to $1/f^2$) with respect to the original accelerometer noise model (shown in Figure 4.2-1). The $1/f^2$ trend (or, upper boundary of the trend) of the low-frequency noise has been inferred from the spectral density of trace of the gravity gradient measured by GOCE over a time period of 60 days (see Figure 5.3-9).

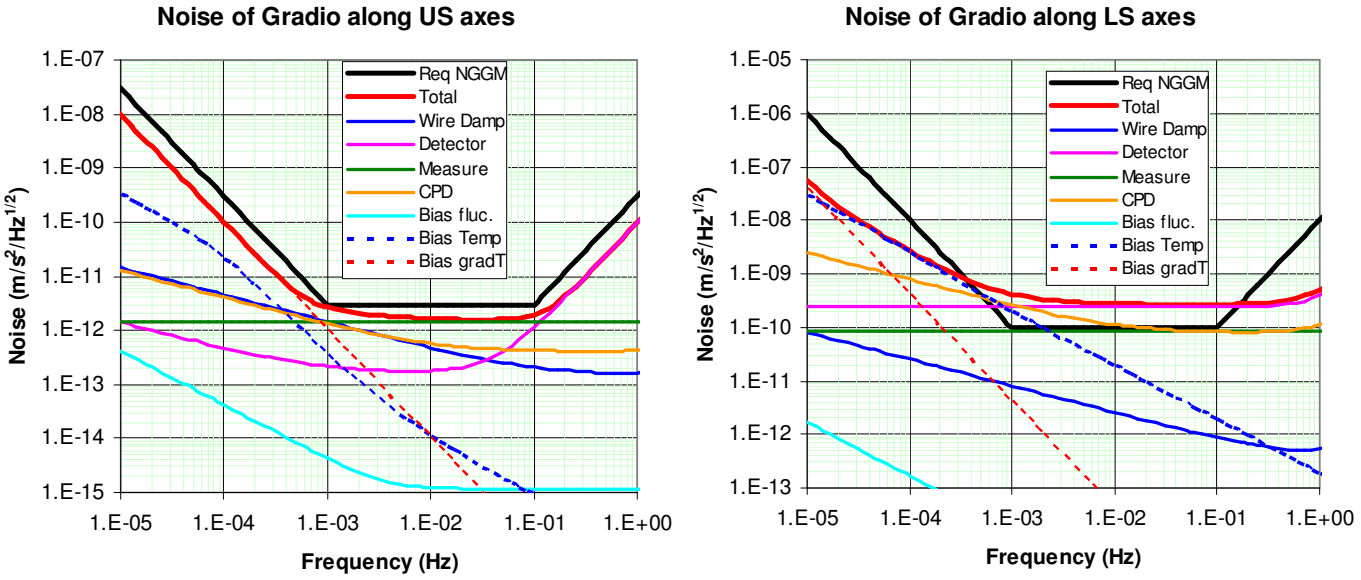

Figure 5.3-7 : Measurement noise predicted for the GOCE accelerometer along the US, LS axes.

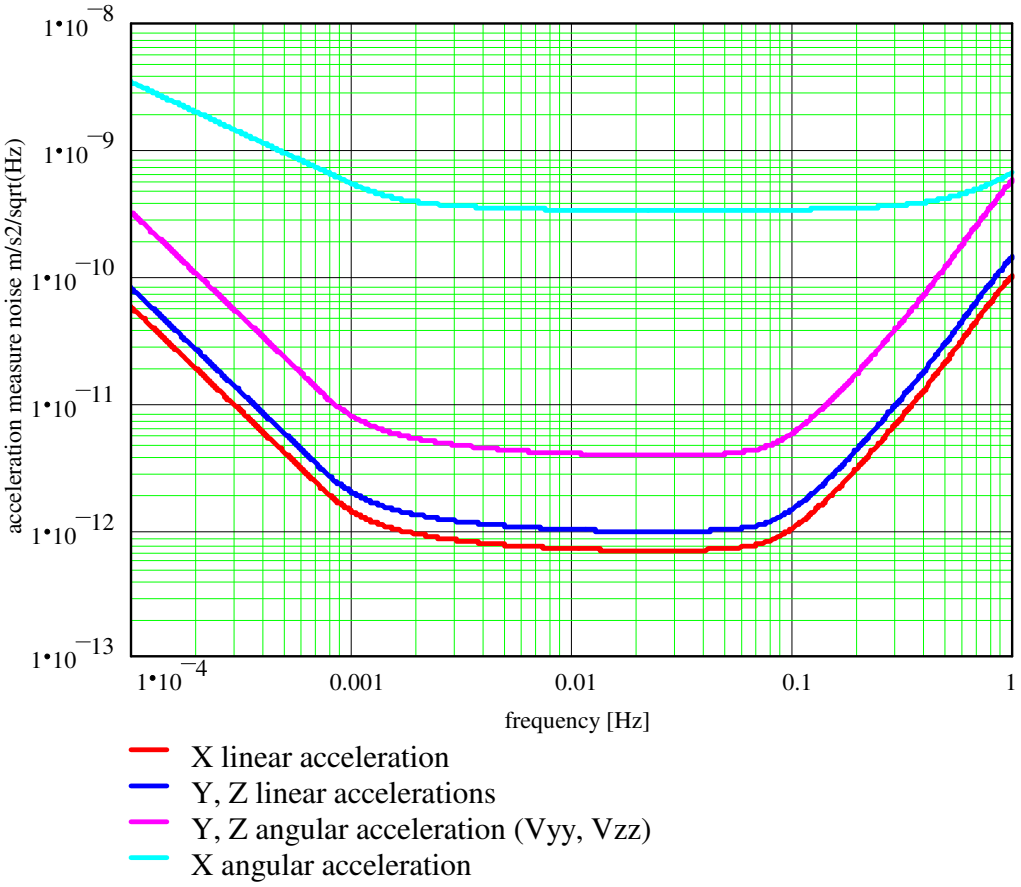

Figure 5.3-8 : Measurement error of linear, angular accelerations and GGT components by the option 2 accelerometer system.

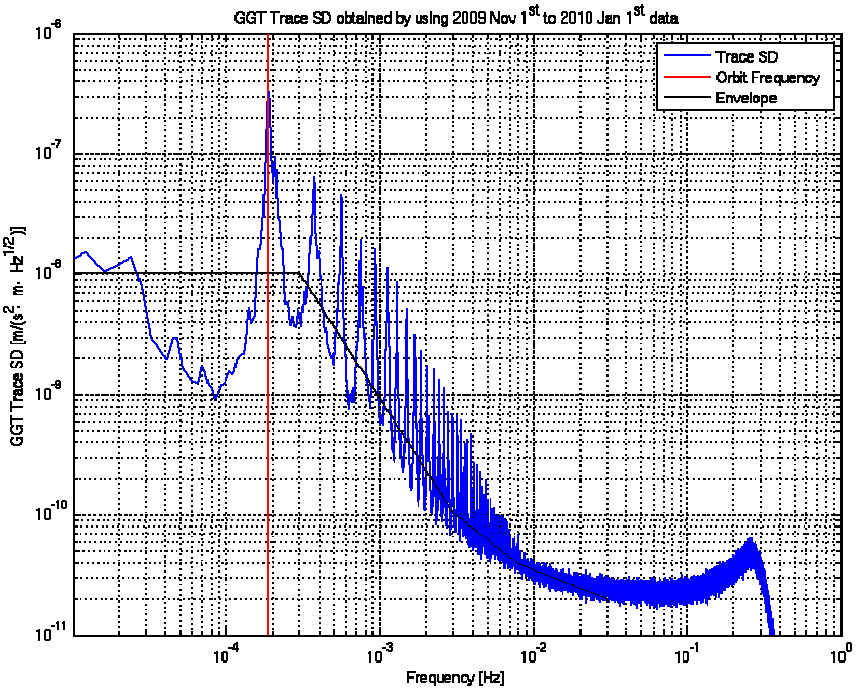

Figure 5.3-9 : Spectral density of the GGT trace measured by GOCE over a period of 60 days, showing a low-frequency trend increasing as $1/f^2$ down to the orbit frequency.

In the preferred option, the overall acceleration measurement system consists of:

- 4 accelerometers,
- 2 front-end electronics units,
- 1 digital electronics (plus 1 for redundancy) for controlling the accelerometers and interfacing with the spacecraft.

The mass and power consumption of the whole accelerometer system can be estimated by analogy with the flight hardware of GOCE.

Item	N.	Unit Mass	Total Mass	Unit Power	Total Power
Accelerometer	4	5.2	20.8	-	-
Front end electronics unit	2	6.3	12.6	15	30
Digital electronics unit	2(*)	6.6	13.2	16.5	16.5
Total			46.6		46.5

(*) Redundant unit; only one unit at a time is switched on

In case the resources needed for the accommodation/utilization of four accelerometers on the satellite will not be available, the recommended two-accelerometer option corresponds to the arrangement of the proof masses shown in Figure 5.2-2. The penalty is the lack of useful measurements of the GGT components, but a_X, $\dot{\omega}_Y$, $\dot{\omega}_Z$ are still measured by US axes.

6. INSTRUMENT AND SATELLITE-LEVEL PERFORMANCE SPECIFICATIONS

6.1 Satellite-to-Satellite Distance Measurement Error Breakdown

The breakdown of the satellite-to-satellite distance overall measurement error (Figure 3.2-1) according to the error tree of Figure 3.3-3, for the preferred metrology system (without BSM and without angular metrology on Satellite 1; section 5.3.1, 5.3.2) is provided in Figure 6.1-1.

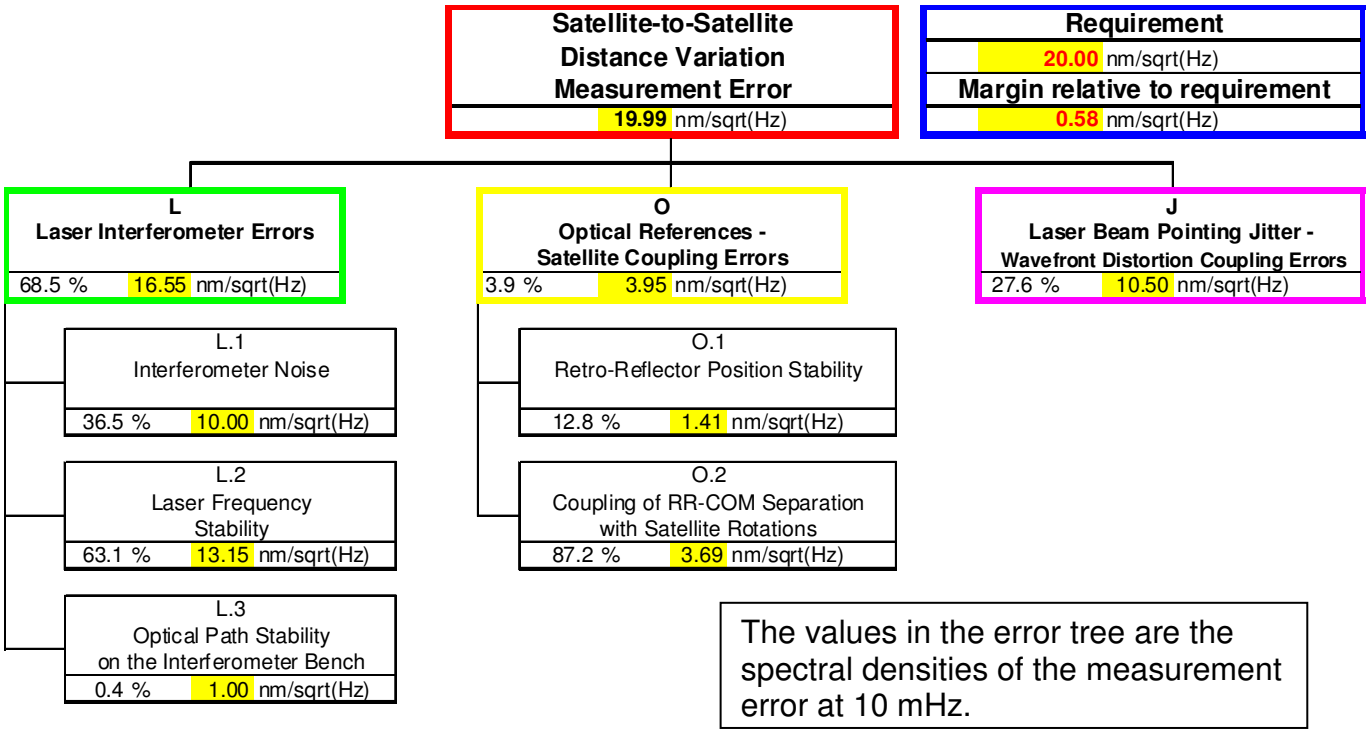

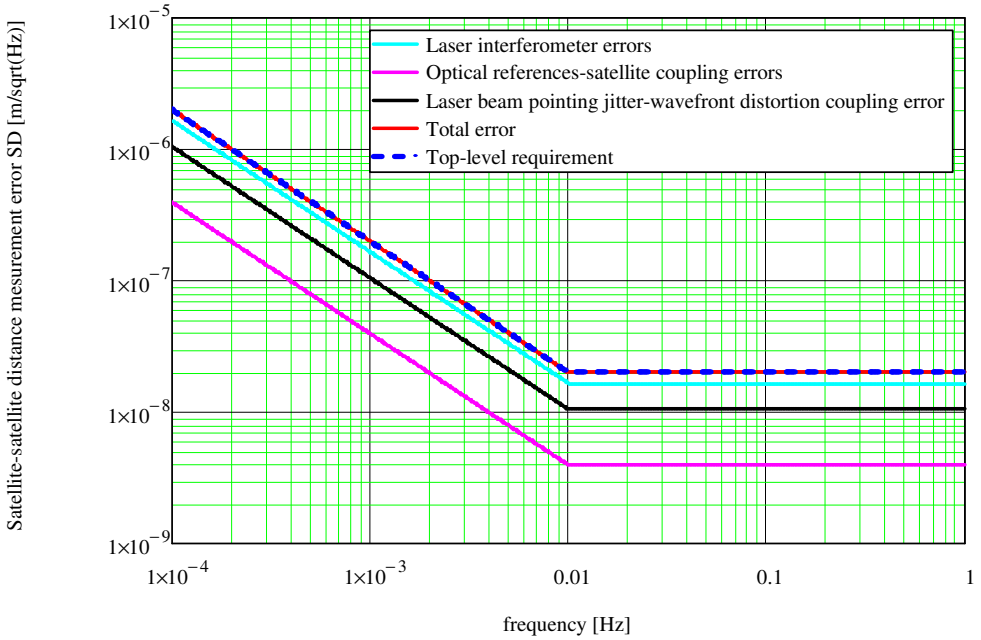

Figure 6.1-1 : Satellite-to-satellite distance variation measurement error breakdown.

The top-level requirement apportionment among the error contributors was performed according to the following criteria:

- The largest portion of the requirement are assigned to the laser frequency stability (L.2), which defines the ultimate limit in the satellite-to-satellite distance measurement noise and is technically very challenging.
- The next largest requirement portion is assigned to the coupling of the laser beam pointing jitter with the wavefront errors (J). The objective is to relax the laser beam pointing requirements up to the point in which they can be fulfilled through the satellite attitude control, without the use of a BSM.
- The third largest requirement portion is for the interferometer intrinsic measurement noise (L.1), to make it achievable up to a relative distance of 100 km using a retro-reflector and a still “modest” laser source (output optical power = 500 mW).
- The requirement portion on the satellite rotation coupling with the retro-reflector offset from the COM (O.2) makes the angle metrology capable to provide the required performance working with the laser source sized for the laser interferometer.
- The smallest portions of the requirement are assigned to the optical bench stability (L.3) and to the retro-reflector position stability (O.1); however the derived thermal and thermo-elastic stability requirements appear still affordable.

6.2 Non-Gravitational Acceleration Measurement Error Breakdown

The breakdown of the relative non-gravitational acceleration overall measurement error (Figure 3.2-2) according to the error tree of Figure 3.4-2, for the preferred accelerometer system (four-accelerometer option 2; section 5.3.2) is provided in Figure 6.2-1.

The top-level requirement apportionment among the error contributors was performed according to the following criteria:

- The requirement portion assigned to the accelerometer noise (I.1) is consistent with the predicted performance of the GOCE accelerometer.
- The requirement portion assigned to the Instrument-Satellite coupling errors (C) leads to the derivation of drag-free control requirements similar to that of GOCE (along the flight direction) and proved achievable from the in-flight experience.
- The requirement portion assigned to the transformation errors from SRF to SSRF (T.2) leads to knowledge and control requirements of the satellite orientation in the SSRF consistent with those deriving from the measurement of the satellite-to-satellite distance variation.
- The requirement portion on the satellite dynamics coupling with the COM position (S.1) leads to positioning and stability requirements consisted with those deriving from the measurement of the satellite-to-satellite distance variation (about the retro-reflector – COM relative position and stability).

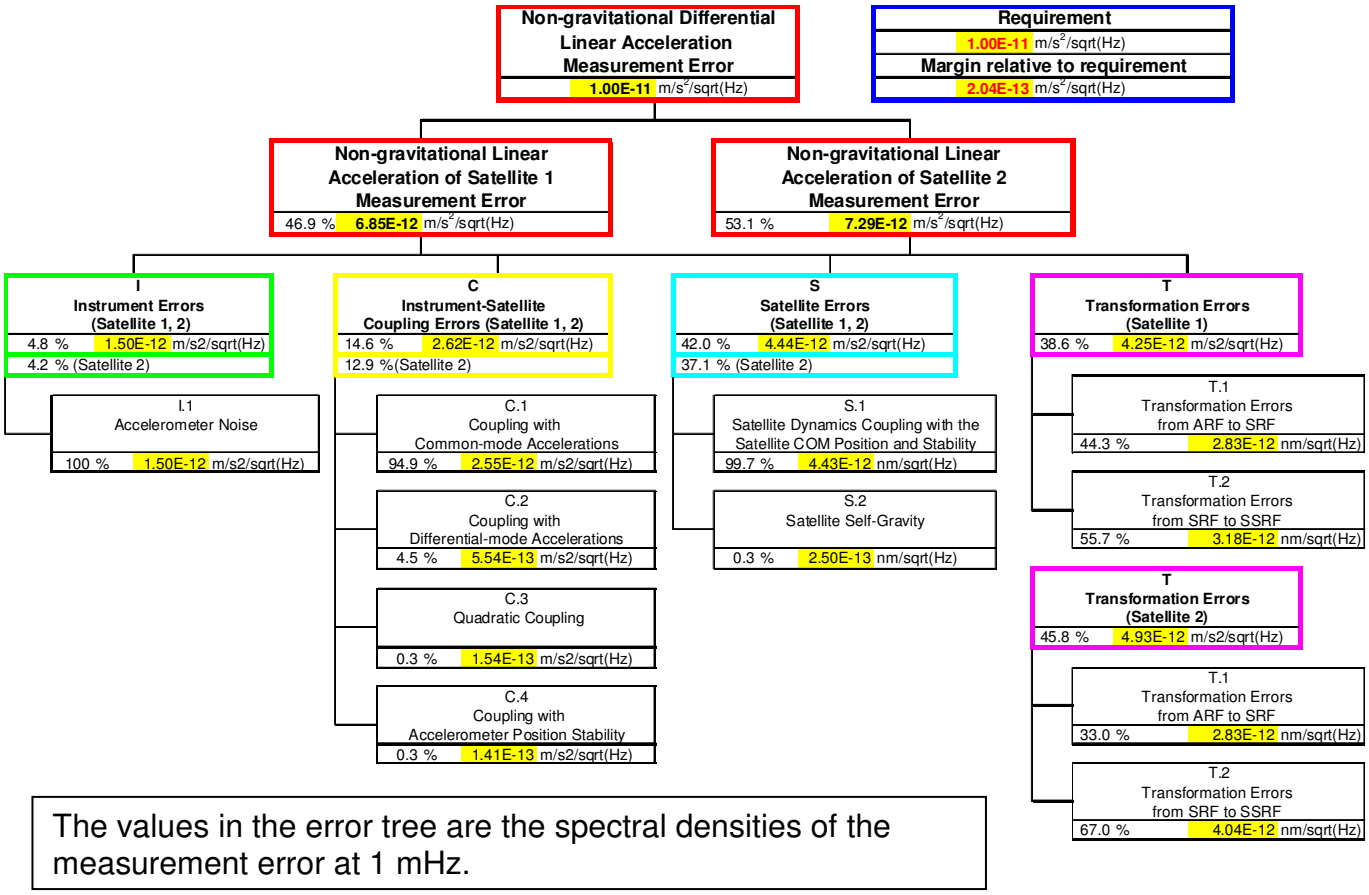

The values in the error tree are the spectral densities of the measurement error at 1 mHz.

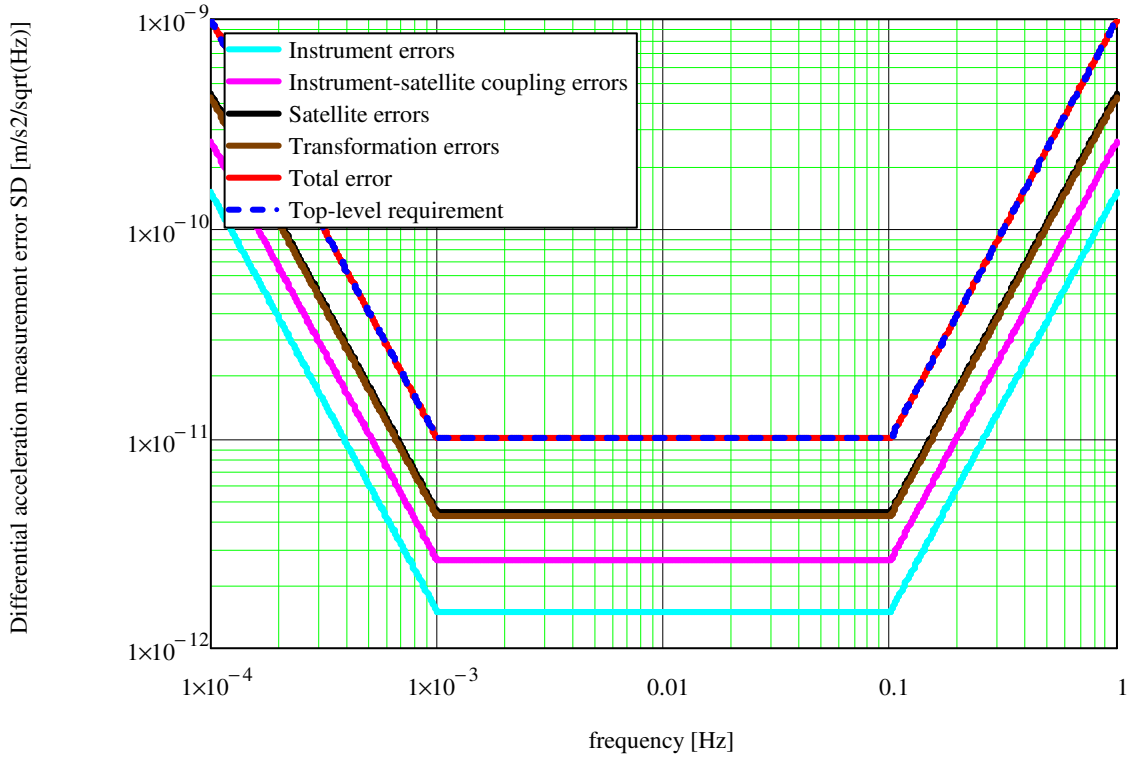

Figure 6.2-1 : Relative non-gravitational acceleration measurement error breakdown.

6.3 Satellite-to-Satellite Laser Metrology System Requirements

On the basis of the top-level requirements apportionment of section 6.1 and of the measurement model of section 3.3 the following requirements are derived for the elements of the satellite-to-satellite laser metrology system.

- Laser interferometer intrinsic noise measurement error spectral density (equal to the preliminary requirement of section 3.3):

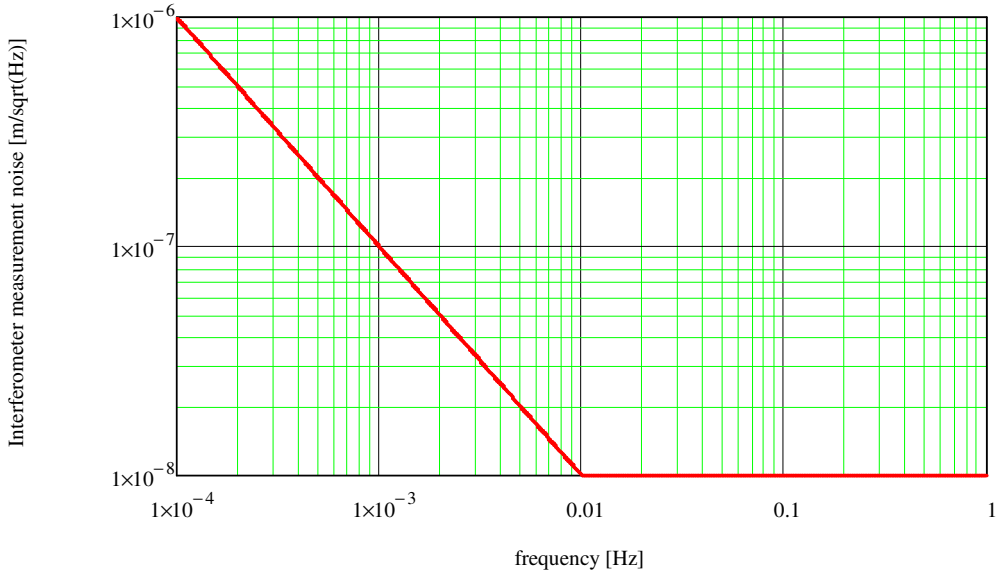

- Laser source frequency stability (close to the specification of the LISA mission [RD-20], [RD-21] and ~4 times from the best performance ever achieved in laboratory [RD-22]):

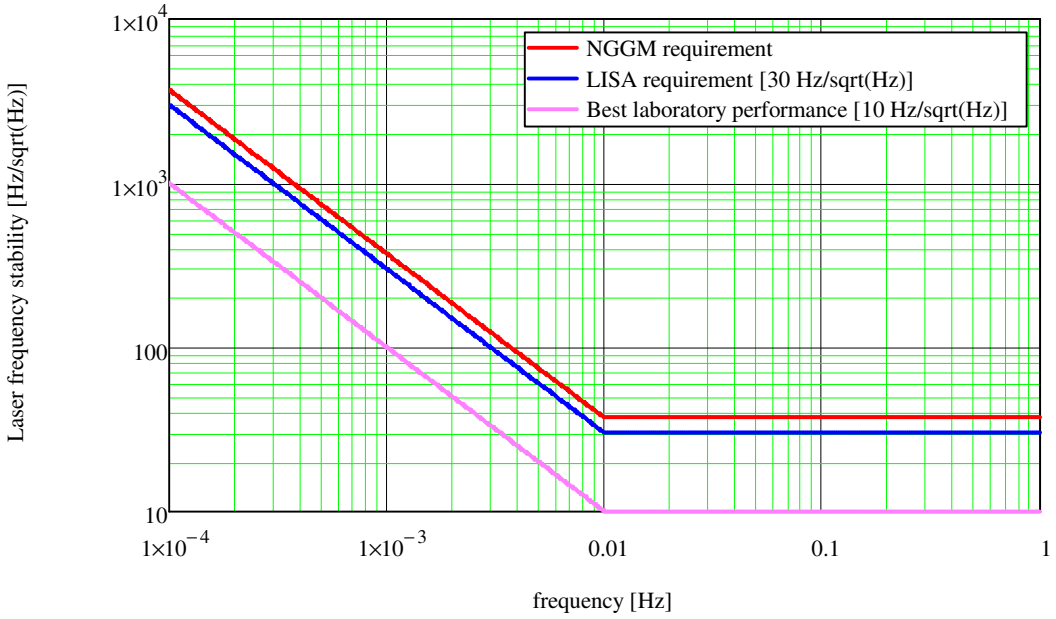

- Satellite attitude measurement error relative to the satellite-to-satellite line (in charge of the angle metrology for Satellite 2 and of the lateral displacement metrology + relative GNSS for Satellite 1):
    - 10^{-4} rad about the Y, Z axes (for Satellite 2)
    - $2 \cdot 10^{-5}$ rad about the Y, Z axes (for Satellite 1, consistent with the laser beam pointing requirement)

- Satellite attitude measurement error spectral density relative to the satellite-to-satellite line (in charge of the angle metrology for Satellite 2 and of the lateral displacement metrology + relative GNSS for Satellite 1):

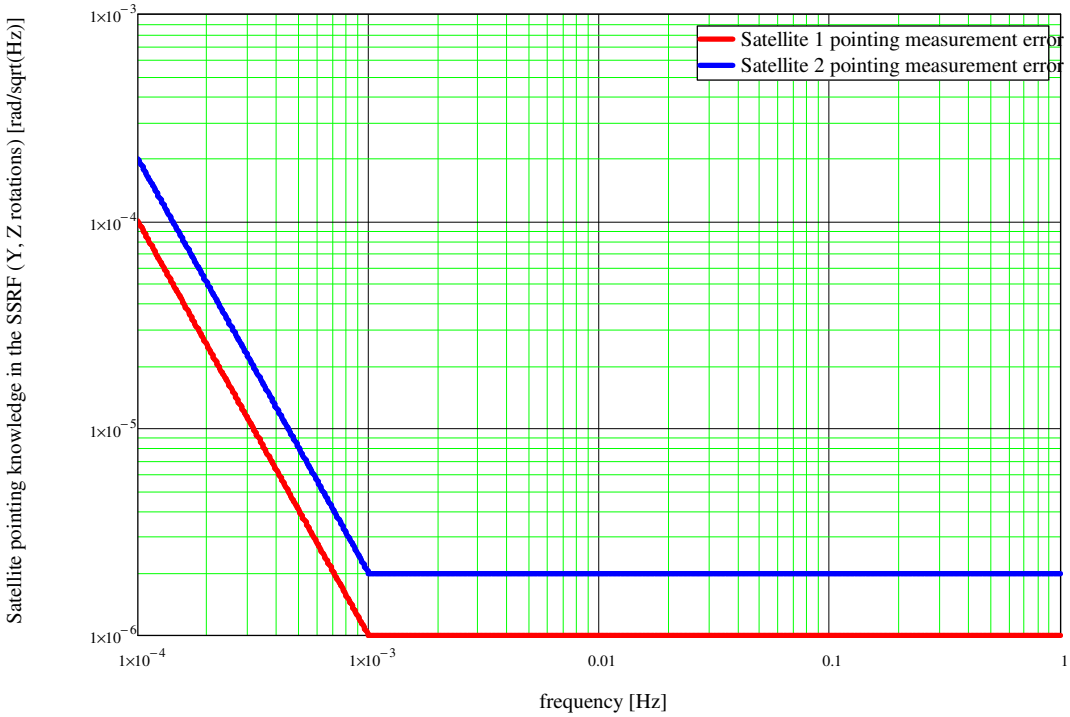

Note: this requirement combines the needs of the satellite-to-satellite distance measurement and of the non-gravitational acceleration measurement.

6.4 Accelerometer Requirements

On the basis of the top-level requirements apportionment of section 6.2 and of the measurement model of section 3.4 the following requirements are derived for the accelerometers (for the preferred accelerometer system made of four GOCE-like accelerometers).

- Accelerometer bias:$\leq 2 \cdot 10^{-7}$ m/s^2 (ultra-sensitive axes),$\leq 2 \cdot 10^{-5}$ m/s^2 (less-sensitive axes)

- Accelerometer intrinsic noise along the ultra-sensitive (US) and less-sensitive (LS) axis (the US noise is equal to the preliminary requirement of section 3.4):

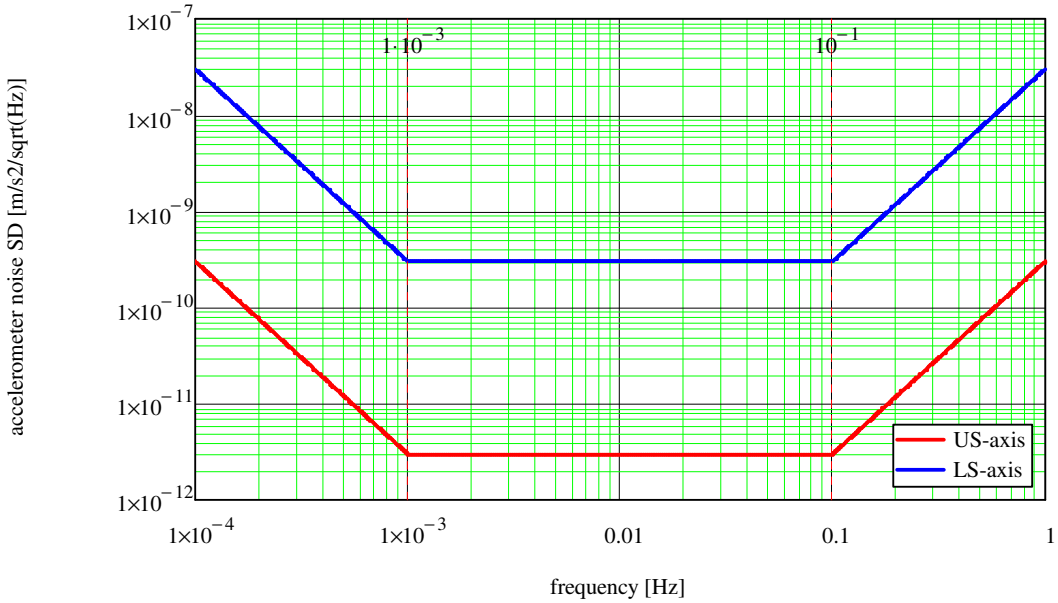

These requirements are consistent with the predicted performance of the GOCE accelerometer (see Figure 5.3-7). Note that for the purpose of the ll-SST application, it is not necessary to specify a flat noise up to 0.1 Hz (the reason is explained in section 3.2.3). However the requirement has been specified in this way because:

1. it is within the reach of the GOCE accelerometer
2. a low acceleration measurement noise in the region from 10 to 100 mHz can be useful for auxiliary gradiometric measurements or in case the laser interferometer performs better than specified at these frequencies.

- Accelerometer absolute scale factor knowledge error: $\leq 2 \cdot 10^{-4}$ for the US axes aligned along the X-axis of the satellite; $\leq 1 \cdot 10^{-3}$ for the other axes.
- Accelerometer scale factor stability along the all axes (equal to the preliminary requirement of section 3.4):

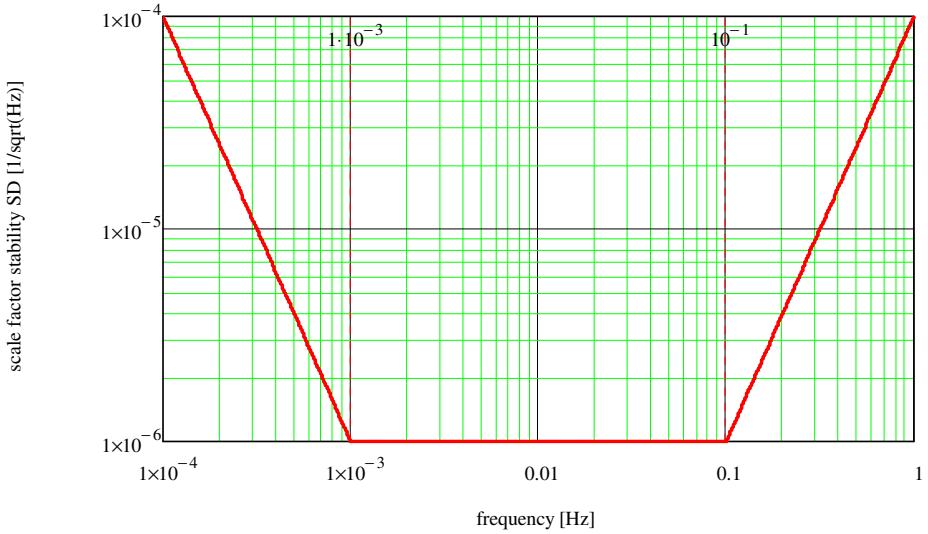

6.5 Satellite Control Requirements

On the basis of the top-level requirements apportionment of sections 6.1, 6.2 and of the measurement model of sections 3.3, 3.4 the following requirements are derived for the control of the satellite pointing, angular acceleration, angular rate and linear acceleration of the COM. The requirements combine the needs of the satellite-to-satellite distance measurement (where the laser beam pointing is provided by the satellite attitude control) and of the non-gravitational acceleration measurement (provided by a set of four accelerometers).

The X-axis of the each satellite shall be aligned to the satellite-to-satellite line (i.e. the line joining the COMs of the two satellites, as shown in Figure 6.5-1) with the following accuracy:

- Satellite 2: ≤ 1° (thanks to the use of a retro-reflector);
- Satellite 1: ≤ $2 \cdot 10^{-5}$ rad (driven by the laser beam pointing).

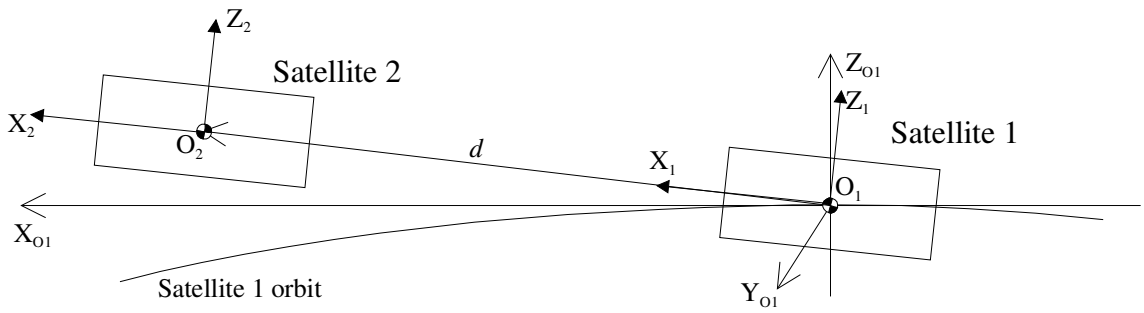

Figure 6.5-1 : Definition of the satellite-to-satellite alignment.

The X-axis of the each satellite shall be maintained aligned to the satellite-to-satellite line with the following stability:

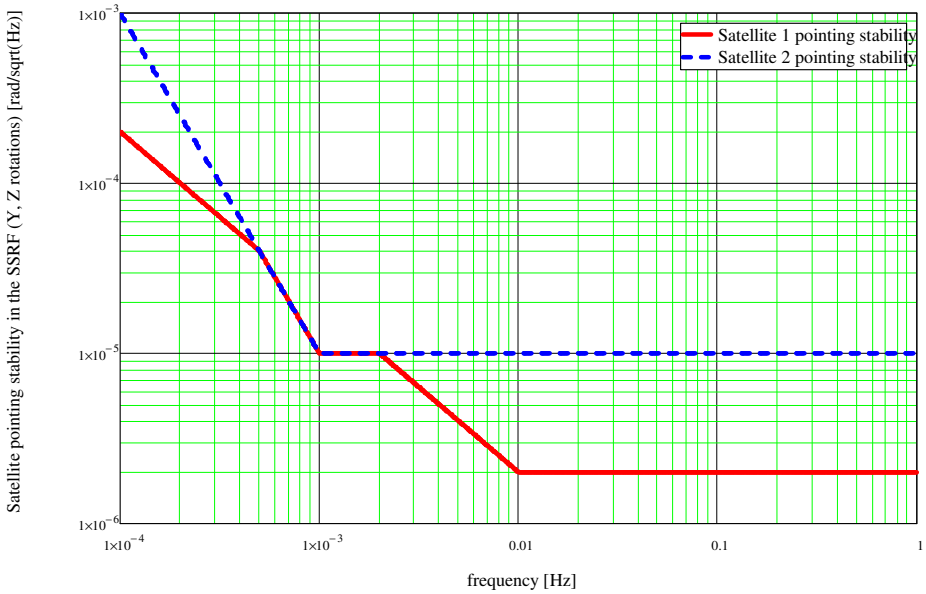

The derivation of the satellite attitude stability requirement defines the angular rate and angular acceleration control requirements around the Y and Z axes. By combining these derived requirements with those related to the measurement of the non-gravitational accelerations (defined for limiting the centrifugal and angular acceleration sensed by the accelerometers), the following limits are established for the angular rates and angular accelerations respectively.

- The angular rates of Satellite 1, 2 around the X, Z axes shall be ≤ $1 \cdot 10^{-4}$ rad/s ($1.2 \cdot 10^{-3}$ rad/s around Y).
- The angular rates of Satellite 1, 2 around the X, Y, Z axes shall be controlled with the following stability:

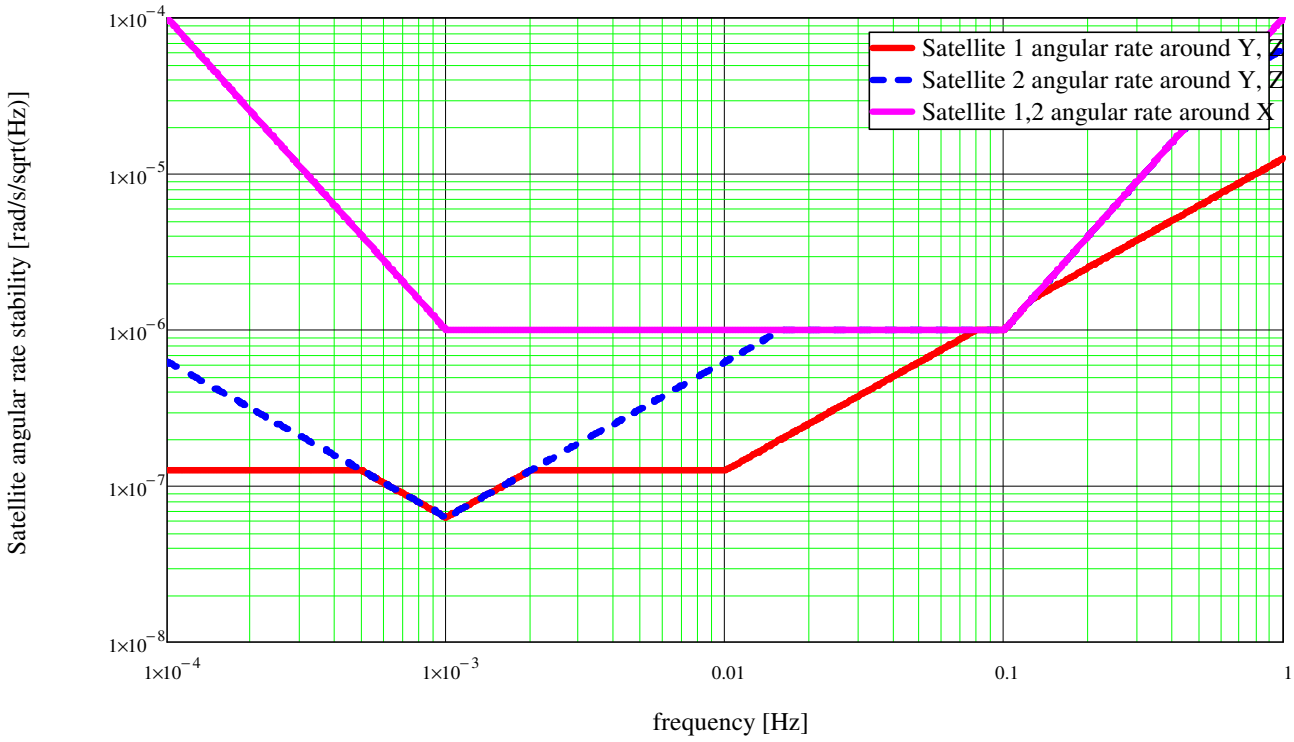

- The angular accelerations of Satellite 1, 2 around the X, Y, Z axes shall be ≤ $1 \cdot 10^{-6}$ rad/s^2.
- The angular accelerations of Satellite 1, 2 around the X, Y, Z axes shall be controlled with the following stability:

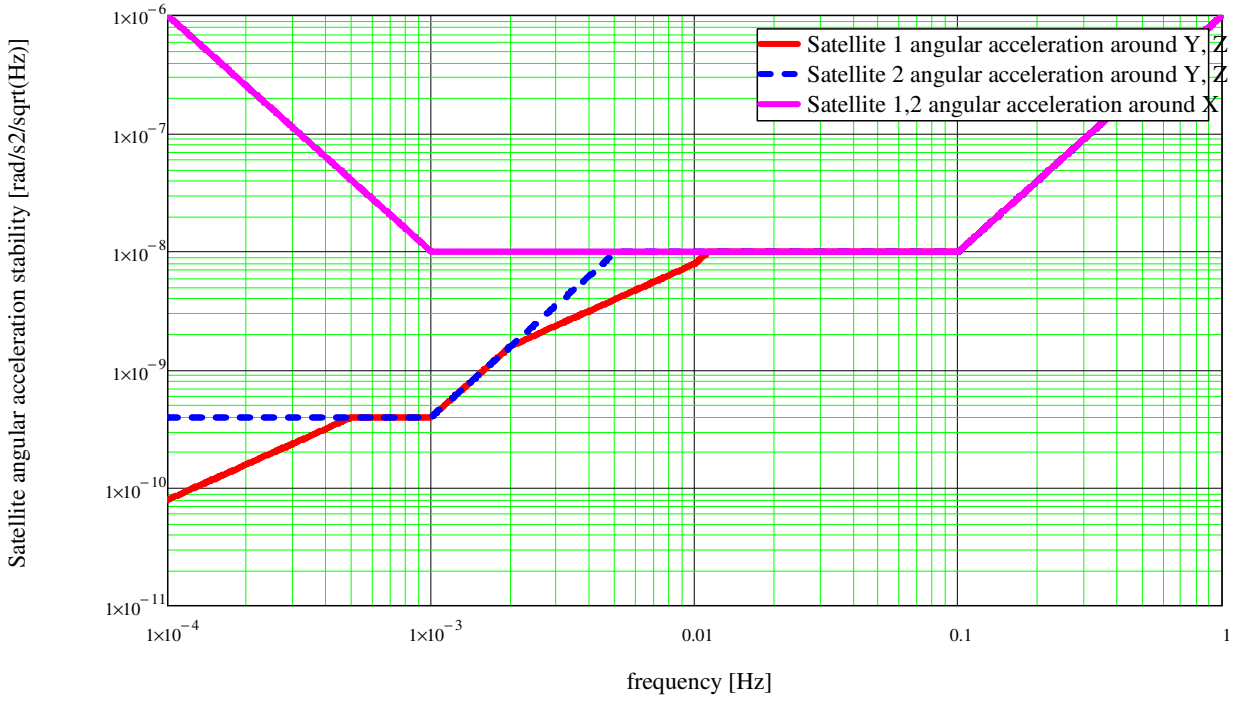

The coupling of the satellite linear acceleration with the non-unitary scale factors and the misalignments of the accelerometer axes, gives rise to the following drag-free control requirements.

- The non-gravitational linear accelerations of the Satellite 1, 2 COM along the X, Y, Z axes shall be ≤ $1 \cdot 10^{-6}$ rm/s^2.
- The non-gravitational linear accelerations of the Satellite 1, 2 COM along the X, Y, Z axes shall be controlled with the following stability:

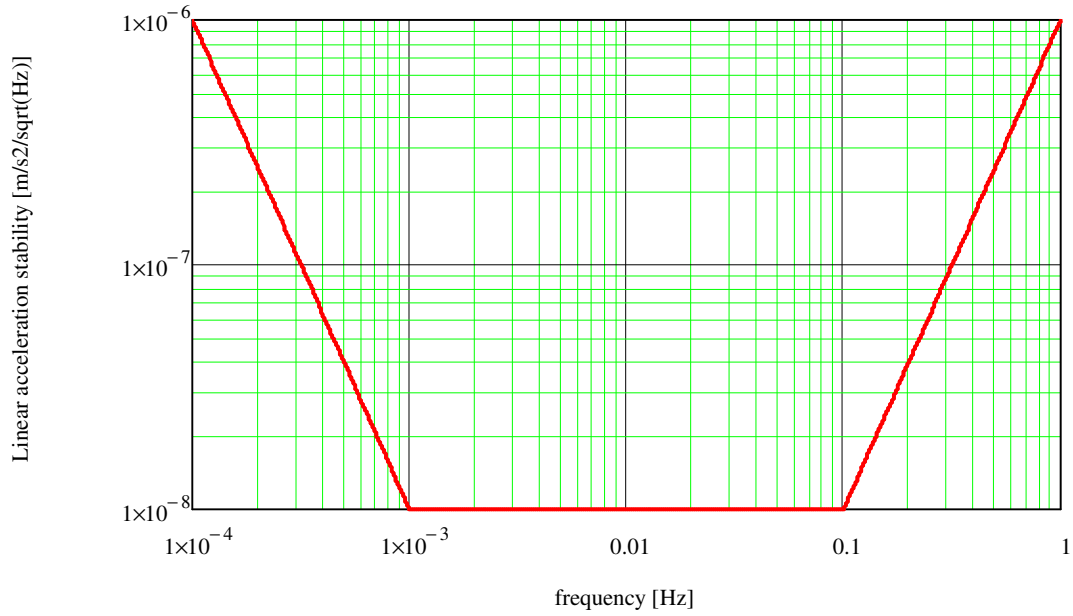

From the above requirements, it turns out that the accelerometer set, utilized as sensors in the drag-free and attitude control (DFAC) loop, shall be able to provide the measurement of (Figure 6.5-2):

- the linear acceleration with a noise level <10^{-9} m/s^2/√Hz along each axis;
- the angular acceleration with a noise level <10^{-9} rad/s^2/√Hz along around the X axis;
- the angular acceleration with a noise level <10^{-10} rad/s^2/√Hz along around the Y, Z axes.

These acceleration measurement requirements are fulfilled by the reference configuration of four GOCE-like accelerometers (see Figure 5.3-8). For the purpose of the attitude pointing stability, it is not required that the angular acceleration measured by the accelerometer set is small at low frequency (<1 mHz), since here the accelerometers are hybridized with the angle metrology (whose angle measure has a lower drift than the acceleration measurement integrated twice). Moreover, the utilization of the accelerometer in the attitude control loop applies only to an in-line (GRACE-like) satellite formation, where the satellite-to-satellite pointing control is performed around a zero angular acceleration, and not to a “pendulum” or “cartwheel” satellite formation, where the satellite-to-satellite pointing follows the satellite relative motion that induces a natural non-zero angular acceleration.

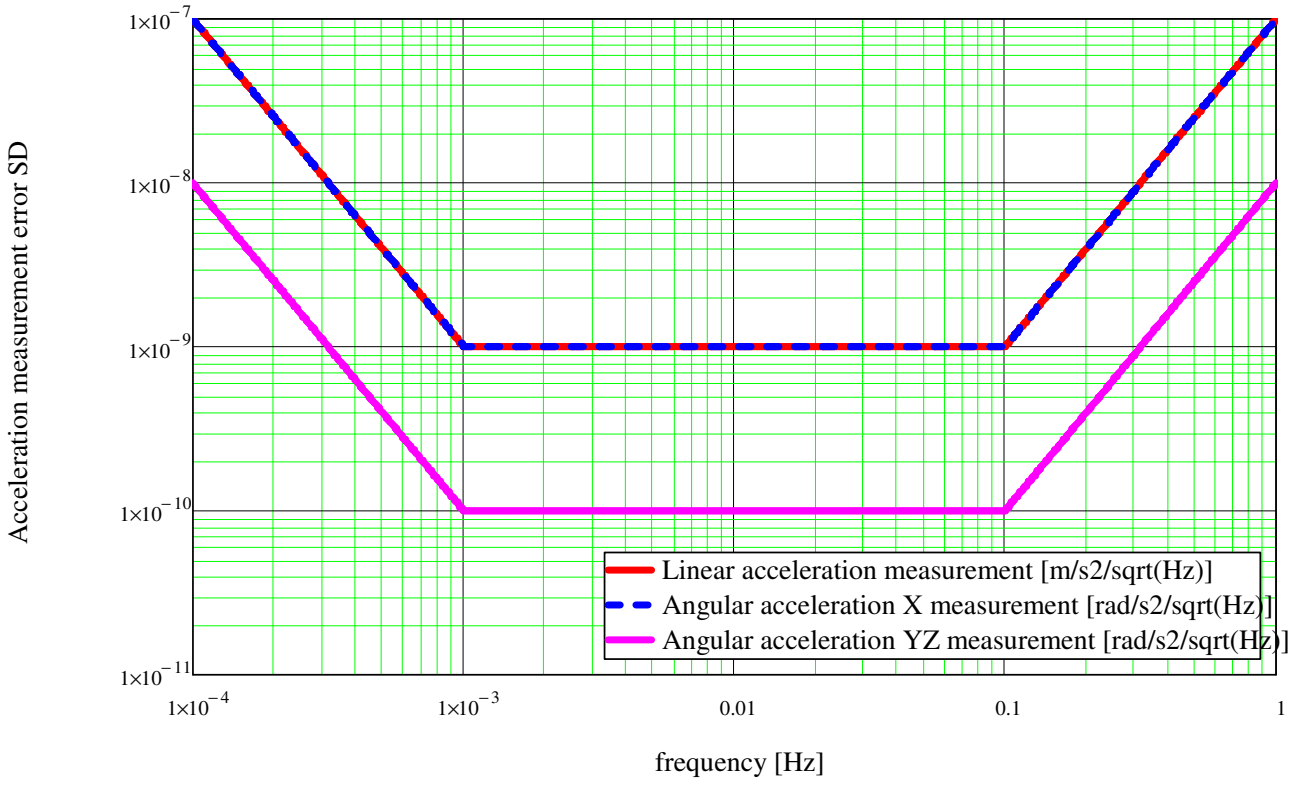

Figure 6.5-2 : Measurement requirements of the accelerometer set as DFAC sensors.

The measurement models for the satellite-to-satellite distance and for the non-gravitational acceleration don't provide any indication about the control of the relative position of the two satellites (formation control). This control doesn't need to be tight. In fact, the satellites shall be left free to move under the action of the Earth gravity field (the quantity we want to measure) with the minimum disturbance from the formation control action. The minimum requirements that are preliminarily applied to the formation control are:

- to maintain the satellite relative distance within 10% of the reference working value, and possibly within a maximum of 100 km (current sizing distance for the laser metrology);
- to maintain the lateral deviations of the Satellite 2 from the nominal reference trajectory in the Local Orbital Reference Frame of Satellite 1 within 1% of the relative distance.

The requirement on the lateral displacement is strictly applicable to an in-line (GRACE-like) satellite formation and is such to avoid excessive exposure to the drag of the satellite lateral surfaces (since the satellite orientation shall be aligned to the satellite-to-satellite line). Deviations from this constraint are acceptable for the "pendulum" and "cartwheel" satellite formations.

6.6 Positioning and Alignments Requirements

6.6.1 Retro-reflectors and accelerometer positioning relative to the satellite COM

The vertex of the retro-reflector of the laser interferometer (A in Figure 6.6-1) shall be positioned within 1 mm (along Y, Z) from the satellite COM. This positioning shall be maintained all along the mission lifetime.
This relative position shall be always known with a precision of 0.1 mm.
This relative position shall be stable within the following limits:

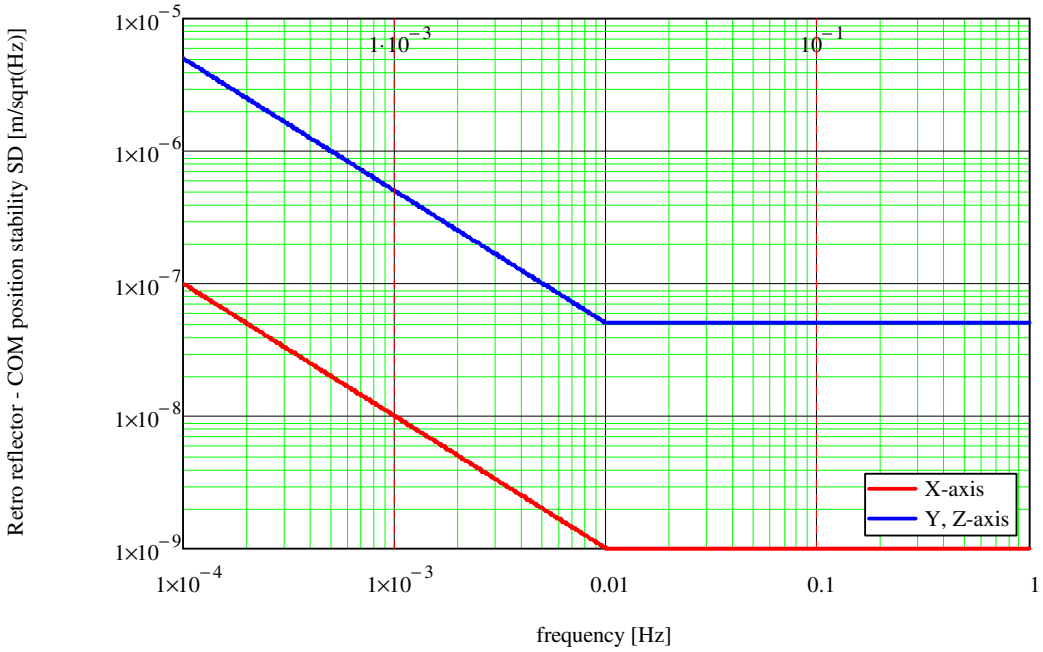

The geometric center of each accelerometer pair (O_{AP1} in Figure 6.6-1) shall be positioned within 0.1 mm (all axes) from the satellite COM. This positioning shall be maintained all along the mission lifetime.
The stability of this relative position shall be such that its second time derivative (acceleration) doesn't exceed the following limits:

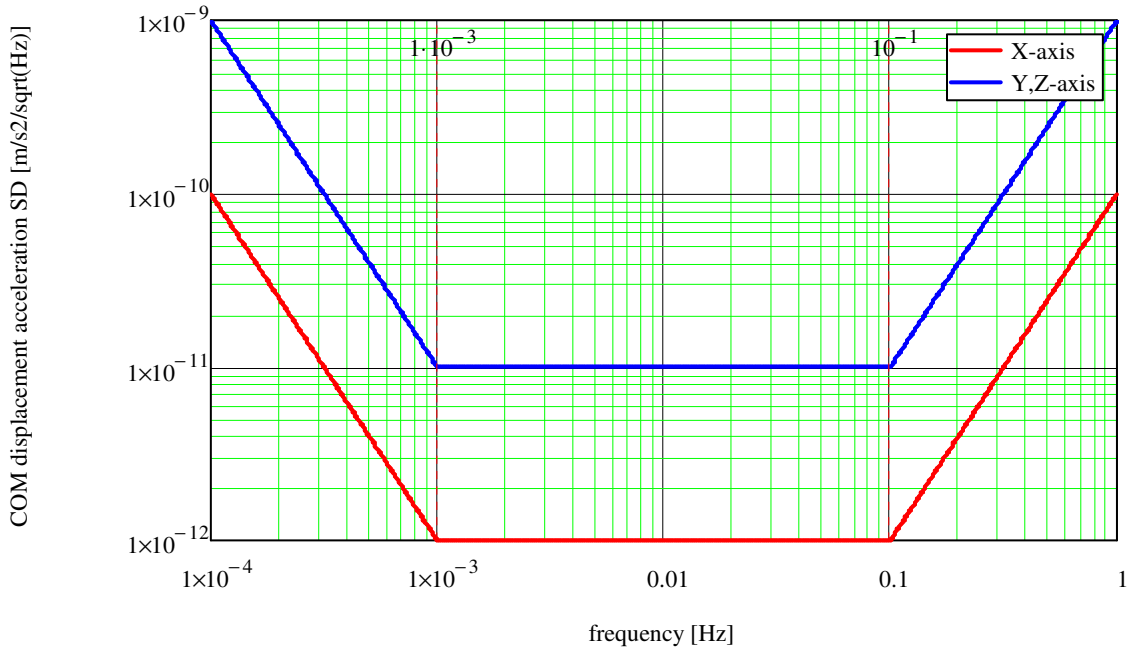

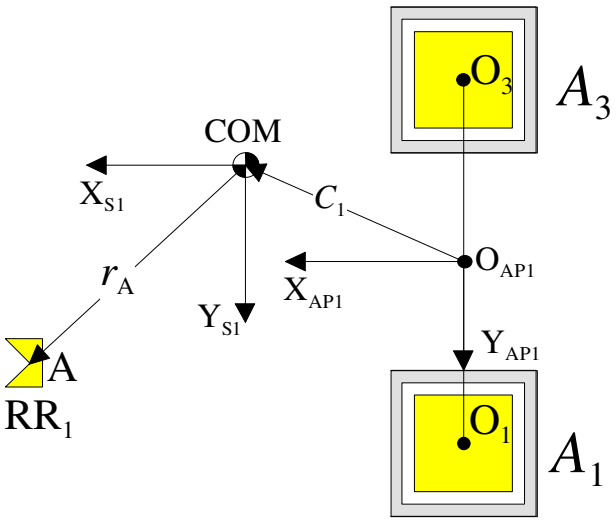

Figure 6.6-1 : Positioning of the accelerometer pair and of the retro-reflector relative to the COM.

6.6.2 Accelerometer alignment to the Satellite Reference Frame

Each accelerometer shall be aligned in the Satellite reference Frame with a maximum deviation:

$$\leq 2 \cdot 10^{-4} \text{ rad (all axes)}$$

This limit shall not be exceeded all along the mission lifetime as the result of the on-ground assembly and alignment of the accelerometers in the satellite, the launch effects (1g-0g transition, temperature environment change, etc..) and the in-flight effects (thermo-elastic misalignment, ageing,..).
From the in-flight measurement of the misalignments of the GOCE accelerometers during the various calibration campaigns [RD-26], this requirement appears achievable.

The accelerometer alignment shall be stable within the following limit:

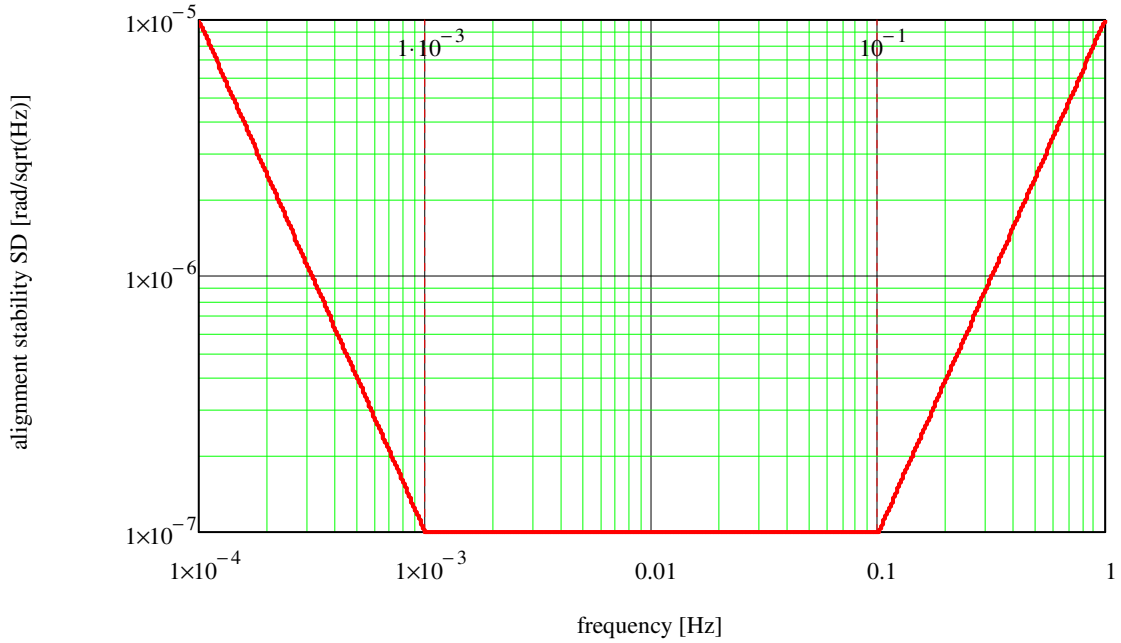

6.7 Temperature Stability Requirements

6.7.1 Optical bench temperature stability

The fundamental design principle of a laser interferometer for precision measurement is that the reference beam and the measurement beam must travel the same optical path up to the beam splitting and recombination points, the only difference being the length to be measured. If this condition is achieved, the only variation of the optical path of the measurement beam which is not experienced also by the reference beam is that of the distance under measurement.
In the optical layout of the metrology system which has been defined this condition is not completely achieved (see Figure 6.7-1). In fact, along the measurement arm between the retro-

reflectors RR_1, RR_2 there are optical elements crossed (twice) by the measurement beam only: the pbs_2, the quarter waveplates (q_1, q_2), the telescope lenses (tl_1, tl_2), and the filter/window.

The variations of the non-common optical path length between the measurement and reference beams (apart from the relative displacement of the two satellites which is the quantity to be measured by the laser interferometer containing the scientific information) are due to:

a) The optical bench temperature variations, inducing changes in the geometric lengths (L_O) and refraction indices (n) of the optical elements:

$$OPL_O = 2\, n \cdot L_O$$

$$\delta OPL_O = 2\left(\frac{dn}{dT}\cdot L_O + n\frac{dL_O}{dT}\right)\cdot \delta T = 2\left(\frac{dn}{dT}\cdot L_O + n\cdot CTE_O \cdot L_O\right)\cdot \delta T = 2\, L_O \cdot \left(\frac{dn}{dT} + n\cdot CTE_O\right)\cdot \delta T$$

where OPL_O is the length of the optical path travelled by the measurement laser beam across the optical elements (pbs_2, q_1, q_2, tl_1, tl_2, filter), δOPL_O is its variation, CTE_O is the coefficient of thermal expansion of the optical elements and dn/dT the temperature derivative of the refraction index, and δT is the temperature variation of the optics.

b) The optical bench structure temperature variations, inducing changes in the distance (L_B) between the pbs_2 and the RR_1:

$$\delta L_B = 2\, L_B \cdot CTE_B \cdot \delta T$$

where CTE_B is the coefficient of thermal expansion of the optical bench structure and δT is its temperature variation (which is the same as for the optics installed on the optical bench, since the optics and the bench structure share the same thermal environment).

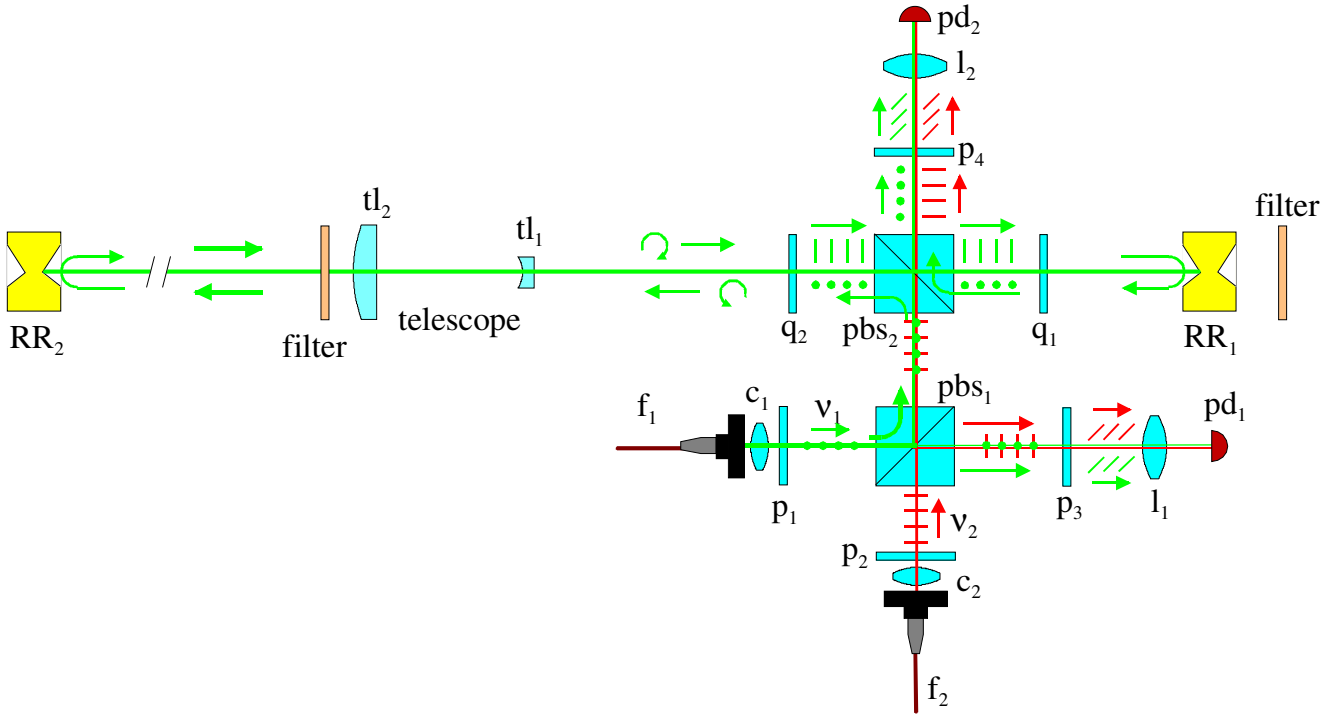

Figure 6.7-1 : Optical layout of the laser interferometer.

The requirement applicable to the optical path variation due to the temperature stability of the optical bench is:

$$\delta\tilde{L}_{OP}(f) \leq \begin{cases} 1.0\cdot 10^{-9} & \text{for } f \geq 0.01 \text{ Hz} \\ 1.0\cdot 10^{-9}\cdot\left(\dfrac{0.01}{f}\right) & \text{for } f < 0.01 \text{ Hz} \end{cases} \quad \text{m/Hz}^{1/2}$$

Standard deviation in MBW = 0.42 nm 1σ

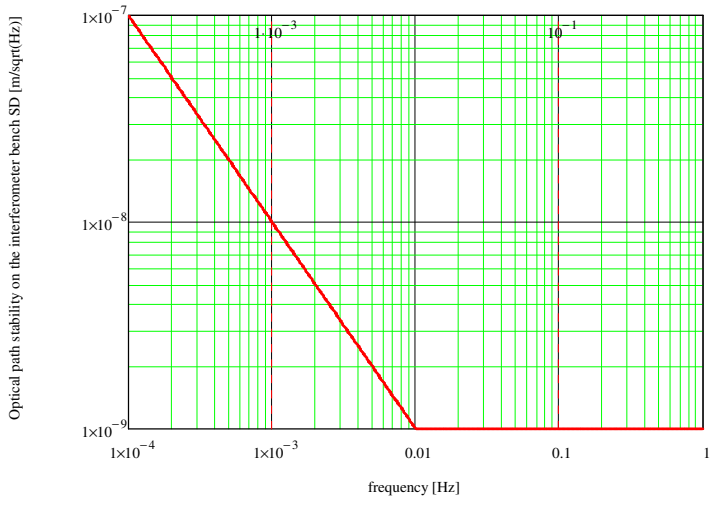

The corresponding requirement on the temperature stability of the optical bench is obtained from the following relationship:

$$\delta \mathrm{OP}\tilde{L}_{\mathrm{O}}(f) + \delta\tilde{L}_{\mathrm{B}}(f) = \delta\tilde{L}_{OP}(f)$$

$$2\,L_{\mathrm{O}} \cdot \left(\frac{dn}{dT} + n \cdot \mathrm{CTE}_{\mathrm{O}} \right) \cdot \delta\tilde{T}(f) + 2\,L_{\mathrm{B}} \cdot \mathrm{CTE}_{\mathrm{B}} \cdot \delta\tilde{T}(f) = \delta\tilde{L}_{OP}(f) \qquad (6.7\text{-}1)$$

$$\delta\tilde{T}(f) = \frac{\delta\tilde{L}_{OP}(f)}{2\,L_{\mathrm{O}} \cdot \left(\frac{dn}{dT} + n \cdot \mathrm{CTE}_{\mathrm{O}} \right) + 2\,L_{\mathrm{B}} \cdot \mathrm{CTE}_{\mathrm{B}}}$$

Taking into account that the optical elements crossed by the measurement laser in the non-common path are made of fused silica (pbs_2, tl_1, tl_2, filter) and crystal quartz (q_1, q_2), the expression (6.7-1) can be further expanded as follows:

$$\delta\tilde{T}(f) = \frac{\delta\tilde{L}_{OP}(f)}{2\,L_{FS} \cdot \left(\left(\frac{dn}{dT} \right)_{FS} + n_{FS} \cdot \mathrm{CTE}_{FS} \right) + 2\,L_{CQ} \cdot \left(\left(\frac{dn}{dT} \right)_{CQ} + n_{CQ} \cdot \mathrm{CTE}_{CQ} \right) + 2\,L_{\mathrm{B}} \cdot \mathrm{CTE}_{\mathrm{B}}} \qquad (6.7\text{-}2)$$

where L_{FS} (L_{CQ}) is the geometric length of the fused silica (crystal quartz) optical elements, n_{FS} (n_{CQ}) is their refraction index, $(dn/dT)_{FS}$ ($(dn/dT)_{CQ}$) is their temperature derivative of the refraction index and CTE_{FS} (CTE_{CQ}) is their coefficient of thermal expansion.

The inputs utilized to compute the temperature stability requirement for the optical bench are:

- L_{FS} = 65.4 mm
- L_{CQ} = 12.7 mm
- n_{FS} = 1.4496
- n_{CQ} = 1.5428
- $(dn/dT)_{FS}$ = $9.6 \cdot 10^{-6}$ 1/K
- $(dn/dT)_{CQ}$ = $5 \cdot 10^{-6}$ 1/K
- CTE_{FS} = $5.2 \cdot 10^{-7}$ 1/K
- CTE_{CQ} = $13.2 \cdot 10^{-7}$ 1/K
- L_{B} = 130 mm
- $\mathrm{CTE}_{\mathrm{B}}$ = $2 \cdot 10^{-7}$ 1/K (Carbon-Carbon composite)

The requirement on the spectral density limit of the temperature variation of the optical bench (i.e. the specification for the optical bench thermal control) is:

$$\delta\tilde{T}(f) \leq \begin{cases} 6.3\cdot 10^{-4} & \text{for } f \geq 0.01 \text{ Hz} \\ 6.3\cdot 10^{-4}\cdot\left(\dfrac{0.01}{f}\right) & \text{for } f < 0.01 \text{ Hz} \end{cases}$$

$K/Hz^{1/2}$

Standard deviation in MBW = 0.27 mK 1σ

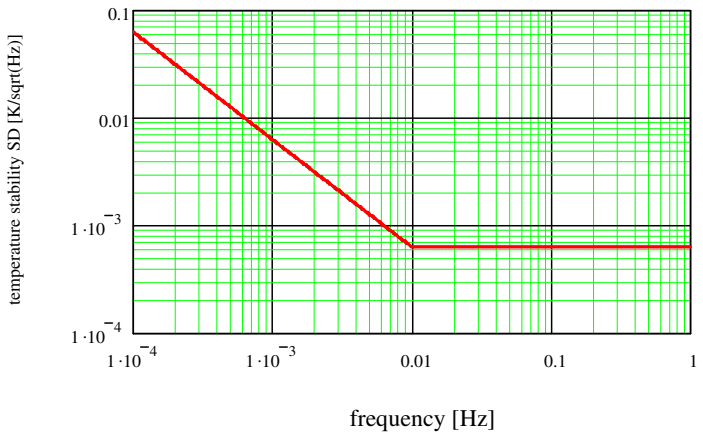

6.7.2 Thermal stability of the reference optical cavity

Among the elements hosted on this bench, the most critical one for the thermal stability is the Fabry-Perot optical cavity for the laser frequency stabilisation. The required temperature stability is defined by the relationship:

$$\delta T < \frac{1}{CTE}\frac{\delta\nu}{\nu}$$

where $\frac{\delta\nu}{\nu}$ is the relative frequency stability to be achieved by locking the laser to the optical cavity and CTE is the coefficient of thermal expansion of the material of the spacer joining the two end mirrors.

By using a spacer made of premium grade ULE™, having a mean CTE = 0 ± 10^{-8} K^{-1} in the temperature range 5 ÷ 35 ºC, and considering for $\frac{\delta\nu}{\nu}$ the requirement defined in section 6.3, we obtain the following requirement for the temperature stability of the Fabry-Perot cavity (the thermal stability requirement of the LISA optical bench is also provided as term of comparison):

$$\delta\tilde{T}(f) \leq \begin{cases} 1.32 \cdot 10^{-5} & \text{for } f \geq f_{L1} \\ 1.32 \cdot 10^{-5} \cdot \left(\dfrac{f_{L1}}{f} \right) & \text{for } f < f_{L1} \end{cases} \quad \text{K/Hz}^{1/2}$$

$(f_{L1} = 0.01 \text{ Hz})$

Temperature fluctuation standard deviation in the MBW = 5.6 µK 1σ

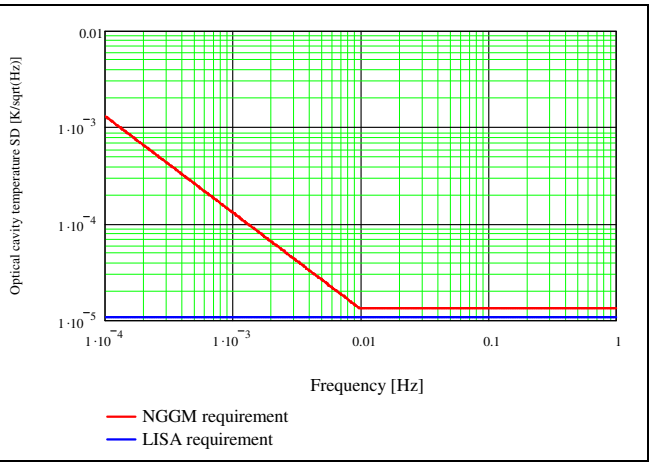

This thermal stability requirement is more stringent than that of the interferometer optical bench (ref. section 6.7.1), but applies only to the Fabry-Perot cavity and not to the whole laser optical bench. Therefore this requirement can be managed by enclosing the optical cavity in a thermally insulated box with a dedicated thermal control.

7. REFERENCE INSTRUMENT CALIBRATION APPROACH

7.1 Calibration of the Satellite-to-Satellite Laser Metrology

No calibration needs identified for the laser interferometer (whose task is to measure distance variations and not absolute distances), after having removed the Beam Steering Mechanism from the baseline configuration. Before, the calibration it was necessary for estimating the optical path variations induced by the BSM operation.

The angle and lateral displacement metrology needs in general to be calibrated, for the measurement of the absolute angular misalignment and lateral offset from the laser beam axis. This calibration can be achieved by comparing the angular and lateral displacement metrology outputs with the same measured quantities obtained from the star trackers and the relative GPS.

7.2 Calibration of the Accelerometers

For the accelerometer primary utilization in the ll-SST mission (measurement of the non-gravitational acceleration of the Satellite COM), the in-flight calibration is necessary only for improving the knowledge precision of the absolute scale factor within $2 \cdot 10^{-4}$ for the US axes aligned along the X-axis of the satellite, and $1 \cdot 10^{-3}$ for the other axes.
A calibration method similar to that utilized on GOCE for the determination of the common scale factor of the accelerometer pairs by using as reference the angular acceleration measured by the star trackers (ref. [RD-26]) can be probably adopted, but it must be suitably adapted to the case in which only two accelerometer pairs are present (in GOCE, the measurements of all six accelerometers are combined in this calibration procedure). The utilization of the trim masses (utilized for adjusting the COM position) could be also utilized this purpose. For instance, by moving them back and forth with the linear translation stage following a given sinusoidal profile, in principle a known acceleration (i.e. with a given amplitude and frequency) is applied to the satellite. The scale factor is derived by comparing this input acceleration with the accelerometer output. The procedure can be repeated for different frequencies and amplitudes of the input acceleration to obtain a full characterization of the scale factor. The feasibility of this approach shall be verified by assessing the disturbances produced by the motion of the test mass and the resulting requirements on the translation stage.

For using the accelerometer set as gradiometer, the differential scale factors and the differential misalignments between the accelerometers shall be calibrated too. For this purpose, a procedure similar to that utilized for GOCE (ref. [RD-26]) can be adopted. Basically, it consists in shaking satellite with the thrusters and in deriving (by least squares fit) of the difference between the scale factors and the alignments that match the measurements of the accelerometer pairs.

7.3 In-flight Measurement of the COM-Accelerometer Relative Position

The COM-O_{AP} offset (vector C_1, ref. Figure 6.6-1) can be measured in flight utilizing a method based on the following relationship between the angular accelerations applied to the satellite and the common-mode acceleration measured be an accelerometer pair:

$$\underline{a}_{c,12} = \frac{1}{2}(\underline{a}_1 + \underline{a}_2) = ([U] - [\Omega^2] - [\dot{\Omega}])\,\underline{C}_1 + 2[\Omega](\underline{\dot{A}}_{c,12} - \underline{\dot{C}}_1) + \underline{\ddot{A}}_{c,12} - \underline{\ddot{C}}_1 + \underline{D}_1 - \underline{MS}_{c,12}$$

$$= \begin{pmatrix} U_{XX} + \omega_Y^2 + \omega_Z^2 & U_{XY} - \omega_X\omega_Y + \dot{\omega}_Z & U_{XZ} - \omega_X\omega_Z - \dot{\omega}_Y \\ U_{XY} - \omega_X\omega_Y - \dot{\omega}_Z & U_{YY} + \omega_X^2 + \omega_Z^2 & U_{YZ} - \omega_Y\omega_Z + \dot{\omega}_X \\ U_{XZ} - \omega_X\omega_Z + \dot{\omega}_Y & U_{YZ} - \omega_Y\omega_Z - \dot{\omega}_X & U_{ZZ} + \omega_X^2 + \omega_Y^2 \end{pmatrix} \begin{pmatrix} C_{1X} \\ C_{1Y} \\ C_{1Z} \end{pmatrix} + 2[\Omega](\underline{\dot{A}}_{c,12} - \underline{\dot{C}}_1) + \underline{\ddot{A}}_{c,12} - \underline{\ddot{C}}_1 + \underline{D}_1 - \underline{MS}_{c,12}$$

The method proceeds through the following steps.

1. Apply a sinusoidal angular acceleration about the Z axis:

The amplitude W_Z of the sinusoidal angular acceleration signal shall be larger than all the other terms at the signal frequency ν_s in the expression of the common-mode acceleration. Thus, retaining the largest terms only:

$$\underline{a}_{c,12} = \begin{pmatrix} a_{c,12,X} \\ a_{c,12,Y} \\ a_{c,12,Z} \end{pmatrix} \cong \begin{pmatrix} 0 & W_Z \sin(2\pi\nu_s\, t) & 0 \\ -W_Z \sin(2\pi\nu_s\, t) & 0 & 0 \\ 0 & 0 & 0 \end{pmatrix} \begin{pmatrix} C_{1X} \\ C_{1Y} \\ C_{1Z} \end{pmatrix} = \begin{pmatrix} W_Z \sin(2\pi\nu_s\, t) \cdot C_{1Y} \\ -W_Z \sin(2\pi\nu_s\, t) \cdot C_{1X} \\ 0 \end{pmatrix}$$

2. Extract from $a_{c,12,X}$, $a_{c,12,Y}$ the amplitude of the component at frequency ν_s:

$$(a_{c,12,X})_s = W_Z\, C_{1Y},\ \ (a_{c,12,Y})_s = -W_Z\, C_{1X} \Rightarrow C_{1X} = -(a_{c,12,Y})_s/W_Z\ ,\ \ C_{1Y} = (a_{c,12,X})_s/W_Z$$

3. Repeat the same procedure by apply a sinusoidal angular acceleration about the Y axis to determine also the Z component of the vector C_1.

Once the offset between the COM and the centre of the accelerometer pair has been obtained, it can be adjusted by means of trim masses within the required limit (0.1 mm).

If the laser retro-reflector vertex (A, ref. Figure 6.6-1) has been positioned at the geometric centre of each accelerometer pairs (O_{AP1}, O_{AP2} assumed nearly coincident) with a precision of 0.1 mm, then the in flight positioning of the COM close $O_{AP1,2}$ with a precision of 0.1 mm through the measurement/correction procedure described above, also ensures that the A-COM relative position is known with the required precision of 0.1 mm.

8. ACRONYMS

AD	Applicable Document
ARF	Accelerometer Reference Frame
BOL	Beginning of Life
BSM	Beam Steering Mechanism
C/C	Carbon-Carbon (composite)
CHAMP	CHAllenging Minisatellite Payload
COM	Centre of Mass
DFAC	Drag-Free and Attitude Control
E2ES	End-to-End Simulator
EOL	End of Life
FF	Formation Flying
GGT	Gravity Gradient Tensor
GNSS	Global Navigation Satellite System
GOCE	Gravity field and steady-state Ocean Circulation Explorer
GPS	Global Positioning System
GRACE	Gravity Recovery And Climate Experiment
INRIM	Istituto Nazionale di Ricerca Metrologica
ITT	Invitation To Tender
KBR	K-Band Ranging
LEO	Low Earth Orbit
ll-SST	low-low Satellite to Satellite Tracking
LORF	Local Orbital Reference Frame
LRR	Laser Retro Reflector
LS	Less Sensitive (axis of the accelerometer)
MBW	Measurement Bandwidth
MST	Mission Simulation Tool
NGGM	Next-Generation Gravity Mission
P/L	Payload
POD	Precise Orbit Determination
PSD	Power Spectral Density
RD	Reference Document
RF	Radio Frequency
RMS	Root Mean Square
RR	Retro-Reflector
S/C	Spacecraft
SLR	Satellite Laser Ranging
SQUID	Superconducting Quantum Interference Device
SRF	Satellite Reference Frame
SSO	Sun Synchronous Orbit
SSRF	Satellite-to-Satellite Reference Frame
SST	Satellite-to-Satellite Tracking
TAS-I	Thales Alenia Space Italia
TBC	To Be Confirmed
TBD	To Be Defined
US	Ultra Sensitive (axis of the accelerometer)

END OF DOCUMENT